Copyright

by

Ki-Tae Lee

2006

The Dissertation Committee for Ki-Tae Lee certifies that this is the approved version of the following dissertation:

DEVELOPMENT OF PEROVSKITE AND INTERGROWTH OXIDE CATHODES FOR INTERMEDIATE TEMPERATURE SOLID OXIDE FUEL CELLS

Committee:

Arumugam Manthiram, Supervisor

Desiderio Kovar

Harovel G. Wheat

Llewellyn K. Rabenberg

Peter F. Green

DEVELOPMENT OF PEROVSKITE AND INTERGROWTH OXIDE CATHODES FOR INTERMEDIATE TEMPERATURE SOLID OXIDE FUEL CELLS

by

Ki-Tae Lee, B.S., M.S.

Dissertation

Presented to the Faculty of the Graduate School of

the University of Texas at Austin

in Partial Fulfillment

of the Requirements

for the Degree of

Doctor of Philosophy

The University of Texas at Austin

May 2006

ACKNOWLEDGEMENTS

First of all, I would like to thank my mentor as well as supervisor, Professor Arumugam Manthiram, for his support, encouragement, and guidance for my research work. I also thank my committee members for their helpful suggestions and review of my work, and all the faculty, staff, and graduate students in the Materials Science and Engineering Program. Especially, I would like to thank my group members and all Korean friends in Austin for creating a comfortable and fertile atmosphere to work. I also appreciate the understanding attitude of my friends and loved ones, who had to take second place to my research work during the last few years. I wish happiness to all of them. The financial support provided by the Welch Foundation is gratefully acknowledged.

Last but most special and sincere gratitude goes to my parents and brother. I really appreciate their continuous support and endless love throughout all my life. I would like to say, “I do love you all.”

DEVELOPMENT OF PEROVSKITE AND INTERGROWTH OXIDE CATHODES FOR INTERMEDIATE TEMPERATURE SOLID OXIDE FUEL CELLS

Publication No. _____

Ki-Tae Lee, Ph.D.

The University of Texas at Austin, 2006

Supervisor: Arumugam Manthiram

Solid oxide fuel cells (SOFC) offer the advantage of using less expensive oxide catalysts and hydrocarbon fuels directly, but chemical reactivity and thermal expansion mismatch at the conventional operating temperature of ~ 1000 ^{o}C pose serious problems. These difficulties have generated considerable interest in intermediate temperature (500-800 ^{o}C) SOFC, but the lower temperature leads to poor oxygen reduction reaction kinetics with the conventional cathode material, $La_{1-x}Sr_xMnO_3$. To address this issue, this dissertation focuses on the synthesis and characterization of alternative cathode materials based on $Ln_{1-x}Sr_xCoO_{3-\delta}$ perovskites and $La_{3-x}Sr_xFe_{2-y}Co_yO_{7-\delta}$ and $LaSr_3Fe_{3-y}Co_yO_{10-\delta}$ intergrowth oxides.

Both the electrical conductivity and the oxide ion vacancy concentration decrease from Ln = La to Gd in $Ln_{1-x}Sr_xCoO_{3-\delta}$, which leads to a decrease in the

electrocatalytic activity for the oxygen reduction reaction. However, the thermal expansion coefficient (TEC) decreases from Ln = La to Gd due to a decreasing ionicity of the Ln-O bond and a suppression of the tendency to lose oxygen from the lattice. Therefore, $Nd_{1-x}Sr_xCoO_{3-\delta}$ with an intermediate size lanthanide ion offers a tradeoff between electrocatalytic activity and TEC, with the x = 0.4 sample exhibiting the highest catalytic activity without any interfacial reaction.

The substitution of Fe or Mn for Co in $Nd_{0.6}Sr_{0.4}CoO_{3-\delta}$ leads to a decrease in the oxygen non-stoichiometry, TEC, electrical conductivity, and electrocatalytic activity, but the decrease in catalytic activity is rapid with the Mn-doped system due to a faster decrease in the oxide ion and electronic conductivities. Interestingly, the incorporation of metallic Ag into porous $Nd_{0.6}Sr_{0.4}Co_{0.5}Fe_{0.5}O_{3-\delta}$ improves the electrochemical performance due to an increased electronic conductivity and enhanced electrocatalytic activity.

The electrical conductivity, oxygen vacancy concentration, TEC, and electrocatalytic activity increase with increasing Co content in the perovskite-related intergrowth oxide systems, $LaSr_3Fe_{3-y}Co_yO_{10-\delta}$ and $Sr_{3-x}La_xFe_{2-y}Co_yO_{7-\delta}$. The increase in catalytic activity is due to an increase in the electronic and oxide ion conductivities. The intergrowth $LaSr_3Fe_{3-y}Co_yO_{10-\delta}$ cathodes offer electrochemical performances comparable to that of the well-known $La_{0.6}Sr_{0.4}CoO_{3-\delta}$ cathode, but with an important advantage of significantly lower TEC.

TABLE OF CONTENTS

LIST OF TABLES

LIST OF FIGURES

CHAPTER 1

INTRODUCTION

1.1 FUEL CELL TECHNOLOGY

The impending energy problems and growing environmental concerns are shifting the paradigm from conventional fossil fuels and internal combustion engines and generating interest on more efficient, environmentally cleaner energy sources or technologies. A fuel cell is an electrochemical energy conversion device which converts chemical energy directly into electrical energy, and therefore it potentially offers much higher efficiency (> 50 %) compared to conventional Carnot-cycle-limited power plants (~ 30 %). Also, fuel cells provide clean energy with no or low emission, and are quiet, modular, and local. Thus, fuel cells can play an important role in future energy technologies.

1.1.1 History of Fuel Cells

The first fuel cell was demonstrated by Sir William Grove, a British amateur physicist, in 1839. Based on reversing the electrolysis of water, he discovered that mixing hydrogen and oxygen within the electrolyte can produce electricity and water.[1] In 1889, Mont and Langer introduced the concept of current density by using porous electrodes, and constructed the basic structure of the modern fuel cell.[2] However, no practical interest occurred until the 1930's, when Bacon developed the

hydrogen-oxygen cell using platinum catalyst and less corrosive alkaline electrolyte.[2] During the 1960's, NASA funded many research projects in fuel cell technology for the space program and then most advanced countries increased their funding for fuel cell R&D in the 1980's.[3] For a long time, however, the cost of fuel cell systems is the main barrier for their commercialization. In recent years, many ongoing research and development are focusing on new materials and innovative solutions that can address the cost and commercial viability issues. Thus, fuel cells are now pursued not only for space missions but also for stationary, transportation, and portable power needs.

1.1.2 Types of Fuel Cells

There are several types of fuel cells and they are most commonly classified according to the electrolyte used.[4,5] The five most common fuel cell types are:

- Phosphoric Acid Fuel Cell (PAFC)
- Alkaline Fuel Cell (AFC)
- Polymer Electrolyte Membrane Fuel Cell (PEMFC)
- Solid Oxide Fuel Cell (SOFC)
- Molten Carbonate Fuel Cell (MCFC)

The typical features and operational characteristics of each type of fuel cell are given in Table 1.1.

Table 1.1 Typical features and characteristics of various fuel cells

	PAFC	AFC	PEMFC	SOFC	MCFC
Electrolyte	H_3PO_4	KOH solution	Sulfonated polymers	Y_2O_3-ZrO_2 (YSZ)	Li_2CO_3-K_2CO_3
Mobile ion	H^+	OH^-	H^+	O^{2-}	CO_3^{2-}
Cathode	Pt	Pt-Au	Pt	$(La,Sr)MnO_3$	Li-NiO
Anode	Pt	Pt-Pd	Pt	Ni/YSZ	Ni
Temperature (^oC)	160-200	60-90	80-110	800-1000	600-800
Fuel	H_2	H_2	H_2	H_2, CO, CH_4	H_2, CO
Oxidant	O_2	O_2	O_2	O_2	$O_2 + CO_2$

1.2 SOLID OXIDE FUEL CELL

Among the various types of fuel cells, SOFC offers important advantages compared to other fuel cells like the PEMFC. The higher operating temperatures (> 500 ^oC) of SOFC allow the use of inexpensive metal oxides or composites of metal oxides and metals as cathode and anode catalysts instead of the expensive and scarcely available platinum catalysts.[6] The higher temperatures also allow in principle the direct use of hydrocarbon fuels without requiring external reforming to produce hydrogen fuel and the cumbersome tasks of safely storing and transporting hydrogen.[7]

1.2.1 Principles of Operation

The basic operating principle of SOFC is shown schematically in Figure 1.1.

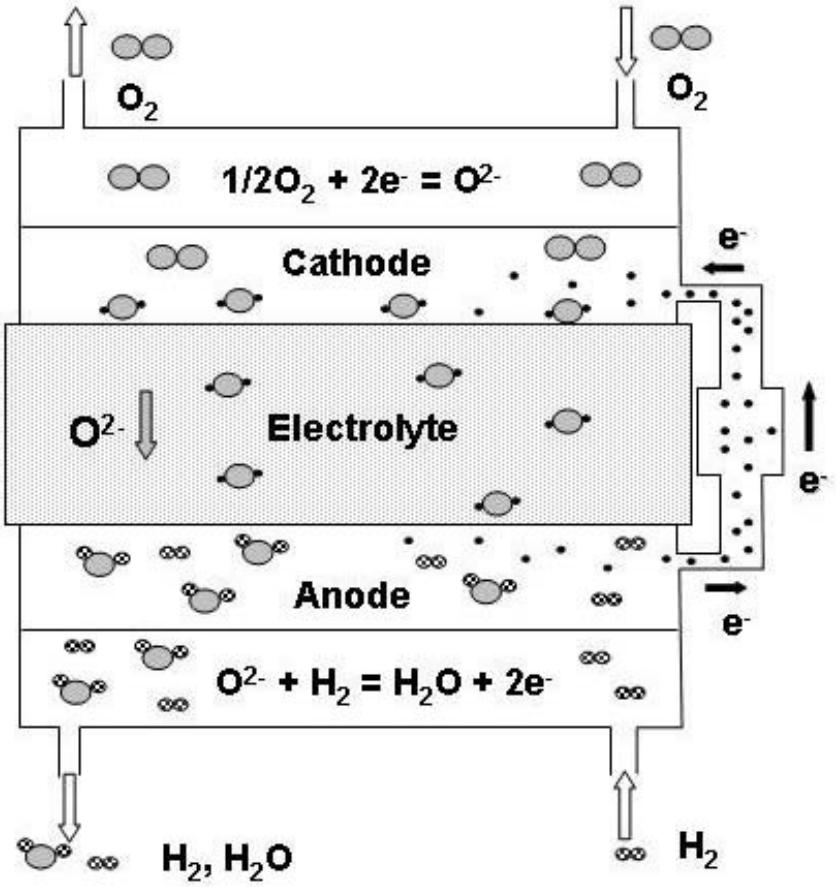

Figure 1.1 Typical operation and configuration of SOFC.

At the porous anode, H_2 gas is oxidized and electrons are released to the external circuit. At the porous cathode, O_2 gas is reduced and electrons are accepted from the external circuit. The oxide ions (O^{2-}) produced pass through the electrolyte from the cathode to anode and the cell electric circuit is completed. The dense electrolyte also

provides a physical barrier to prevent the direct mixing of fuel and oxidant gas. The electrons flow through the external circuit producing direct-current electricity. The overall reaction product is H_2O. In the case of CH_4 fuel, both CO_2 and H_2O are produced at the anode side.

The electromotive force (EMF) or the theoretical reversible potential, E_{th}, of a single cell can be calculated thermodynamically from the free energy change of the electrochemical reaction. If the reactants and products are all in their standard conditions, the reversible standard potential, E^0, of the electrochemical reaction is defined as[8]

$$E^0 = -\frac{\Delta G^0}{nF} \tag{1.1}$$

where ΔG^0 is the Gibbs free energy change for the reaction at the standard state, n is the number of electrons involved in the reaction, and F is the Faraday constant. The Gibbs free energy is dependent on the temperature by the relation

$$\Delta G = \Delta H - T\Delta S \tag{1.2}$$

where ΔH is the enthalpy change for the reaction, T is the absolute temperature, and ΔS is the entropy change for the reaction. Both enthalpy and entropy for the reaction are also dependent on the temperature. For the H_2/O_2 cell, the cell reaction is

$$H_2(g) + \frac{1}{2}O_2(g) = H_2O(g) \tag{1.3}$$

Substituting the standard condition values into Eq. (1.1) and Eq. (1.2) yields

$$E^0 = -\frac{(-237300\ J \cdot mol^{-1})}{(2)\cdot(96485\ C \cdot mol^{-1})} = 1.229\ V \tag{1.4}$$

Beyond the standard condition, the theoretical reversible potential, E_{th}, can be expressed by the Nernst equation[9]

$$E_{th} = E^0 + \frac{RT}{nF} \ln\left(\frac{a_{O_i}^{\nu_i}}{a_{R_i}^{\nu_i}}\right) \tag{1.5}$$

where R is the gas constant, T is the absolute temperature, ν_i is the stoichiometric coefficient of species i, and a_i is the activity of species i. O and R indicate the oxidized and the reduced species, respectively. E^0 is given by Eq. (1.1). Assuming that the gases are ideal and considering Eq. (1.3), Eq. (1.5) becomes

$$E_{th} = E^0 - \frac{RT}{2F} \ln\left(\frac{p_{H_2O}}{p_{H_2} \cdot p_{O_2}^{\frac{1}{2}}}\right) \tag{1.6}$$

where p refers to the partial pressure of each gas.

1.2.2 Polarization

The actual cell potential drops from the theoretical potential value due to the irreversible losses as current is drawn in a practical fuel cell. The loss, which is

termed polarization, or over-potential η is defined as the deviation of the actual cell potential E from the theoretical potential E_{th},

$$\eta = E - E_{th} \tag{1.7}$$

Three types of polarization primarily contribute to the loss (voltage drop): (i) activation polarization (η_{act}), (ii) ohmic polarization (η_{ohm}), and (iii) concentration polarization (η_{conc}).[10-13]

Some electrode reactions are inherently slow and the sluggish reactions, with an associated activation energy, give rise to activation polarization. The activation polarization is generally related to the rate-determining step, which could be charge transfer or the surface exchange reaction (adsorption/desorption of reaction species) in the electrode. The relationship between activation polarization and current density i can be expressed by Butler-Volmer equation:[8,11]

$$i = i_0 \left[\exp\left(\frac{(1-\alpha) nF \eta_{act}}{RT} \right) - \exp\left(\frac{-\alpha nF \eta_{act}}{RT} \right) \right] \tag{1.8}$$

where i_0 is the exchange current density and α is the charge transfer coefficient. The exchange current density represents the reaction rate and it can be determined by extrapolating plots of log i vs. η at $\eta = 0$. When the irreversibility is small, Eq. (1.8) can be simplified as the empirical Tafel equation:[8,11]

$$\eta_{act} = a \pm b \log i \tag{1.9}$$

where a and b are constants. The constant b is called the Tafel slop, which can estimate the catalytic activity. In other words, a smaller Tafel slop means better catalytic activity.

The ohmic polarization, known as iR-drop is related to the resistance for conduction of ions and electrons, and to the contact resistance between the cell components. The ohmic polarization η_{ohm} can be given as[10-13]

$$\eta_{ohm} = i \cdot R \tag{1.10}$$

where i is the current density and R is the total cell resistance including ionic, electronic, and any contact resistances. In order to reduce the ohmic polarization, not only electrolytes with high oxide ion conductivity but also electrodes with high electronic conductivity and good adhesion between cell components are needed.

The concentration polarization η_{conc} is caused by mass transfer or diffusion limitations. The electrode reactions require a constant supply of reactants in order to sustain the current flow. When mass transfer limitation causes a decrease in the availability of reactants, part of the available reaction energy is used to drive mass transfer, resulting in a loss of output voltage. The concentration or diffusion polarization η_{conc} can be expressed as[12,13]

$$\eta_{conc} = \frac{RT}{nF} \ln\left(1 - \frac{i}{i_l}\right) \tag{1.11}$$

where i_l is the limiting current density at which the electrode reaction is completely governed by mass transfer.

A characteristic current-voltage (I-V) curve for SOFC is shown in Figure 1.2. The I-V curve can be divided into three regions, which are governed by different polarization losses. The activation polarization loss is dominant at low current density in the region I. The ohmic polarization loss governs the region II, where the cell voltage decreases linearly with increasing current density. The significant cell voltage drop at high current density in the region III is due to the concentration polarization loss.

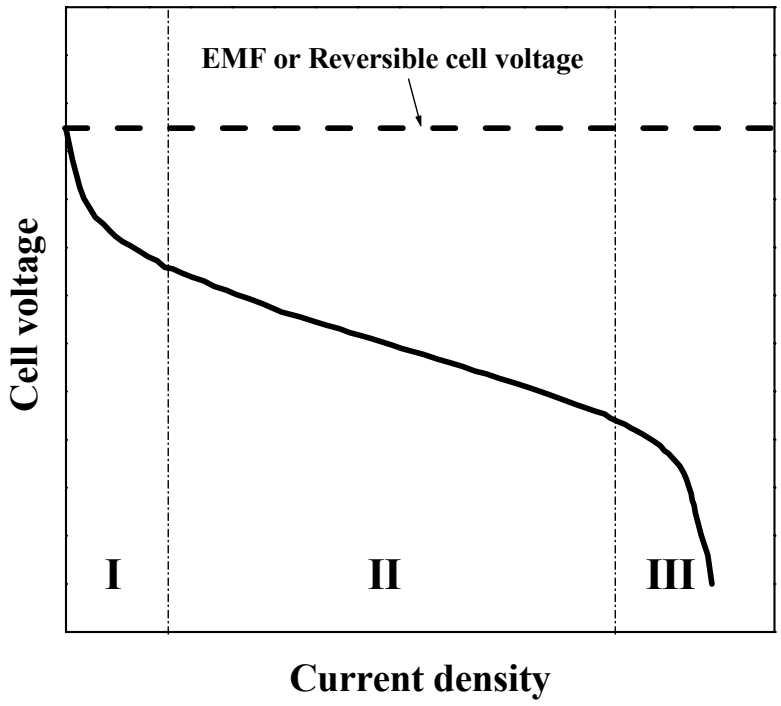

Figure 1.2 Characteristics of a typical current-voltage curve for SOFC.

1.3 CELL COMPONENTS OF SOLID OXIDE FUEL CELL

A SOFC mainly consists of a dense electrolyte, which is an oxide ion conductor, and two porous electrodes (anode and cathode).

1.3.1 Electrolyte

The main role of the electrolyte in SOFC operation is to carry oxide ions and separate the fuel from the oxidant. Thus, the electrolyte must be stable in the duel atmosphere (reducing and oxidizing atmospheres), impermeable to the gases, and have high oxide ion conductivity. Due to the high operating temperature, the electrolyte should also be thermally and chemically stable itself and compatible with other components at high temperature.

Yttria-stabilized zirconia, $Zr_{1-x}Y_xO_{2-0.5x}$ (YSZ), with a fluorite structure has been the most popular electrolyte due to its pure oxide ion conduction over a wide range of oxygen partial pressures.[14-16] The substitution of Y^{3+} for Zr^{4+} in ZrO_2 not only stabilizes the cubic fluorite structure but also creates oxide ion vacancies. Using the Kröger-Vink notation,[17] the formation of oxide ion vacancy can be written as

$$Y_2O_3 \xrightarrow{ZrO_2} 2Y'_{Zr} + 3O_O^{\times} + V_O^{\bullet\bullet} \qquad (1.12)$$

The conductivity of YSZ with 10 mol % yttria is about 0.1 S/cm at 1000 ^oC. At 800 ^oC, however, conductivity decreases to 0.01 S/cm.[16] Therefore, the conductivity of YSZ may not be adequate for intermediate temperature (500-800 ^oC) SOFC. Figure

1.3 shows the temperature dependence of the conductivity of various oxide ion conductors.[1]

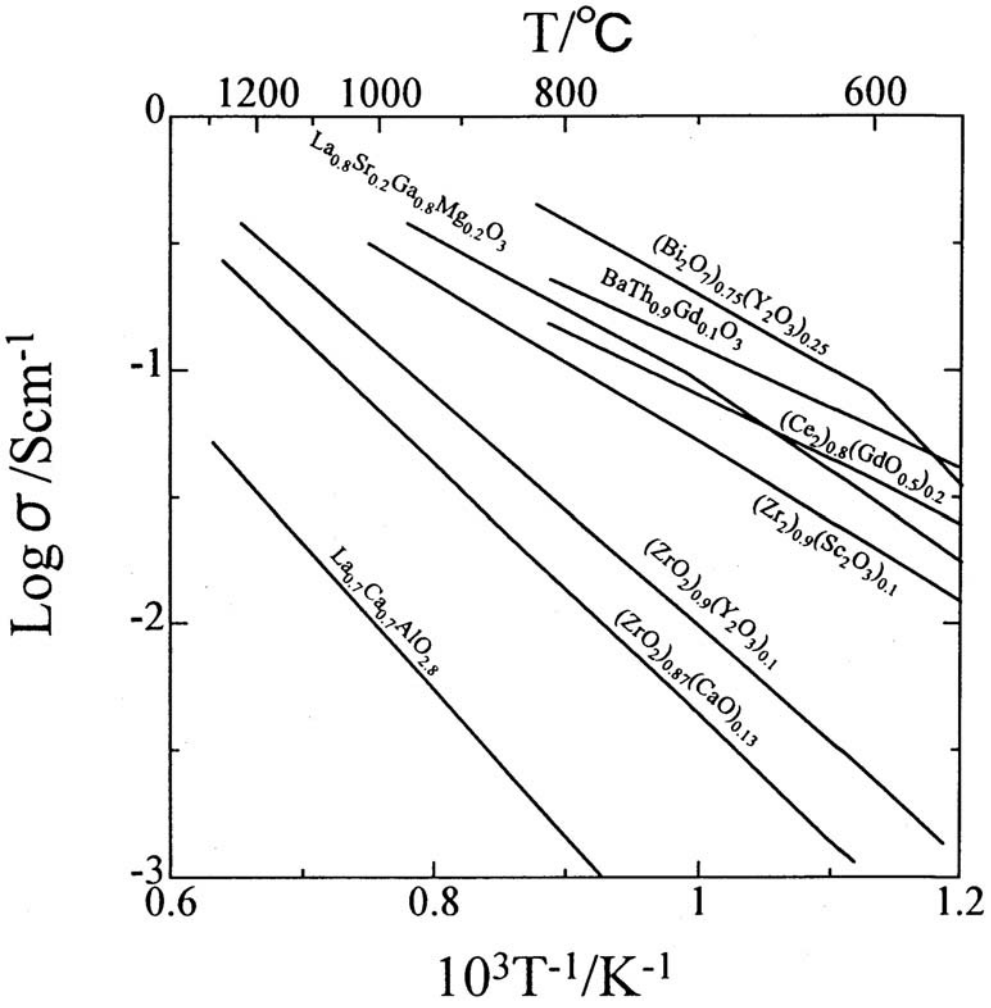

Figure 1.3 The temperature dependence of the conductivity of various oxide ion conductors.[1]

Although bismuth oxide system shows the highest conductivity in the temperature range of 600-800 ^{o}C, stabilized Bi_2O_3 is easily reduced to metallic Bi

leading to electronic conduction, at low oxygen partial pressures (about 10^{-13} atm) at 600 ^{o}C.[18] Therefore, stabilized Bi_2O_3 is not adequate for the practical electrolyte application.

CeO_2 (ceria) doped with a divalent or trivalent oxide has been developed as an alternative electrolyte due to its higher oxide ion conductivity and lower activation energy compared to those of YSZ.[19-21] However, the main drawback of doped ceria is the reduction of Ce^{4+} to Ce^{3+} ion at low oxygen partial pressure with an accompanying electronic conduction.[19] The electronic conductivity at electrolyte generates electronic leakage current and leads to a consequent decrease in the efficiency. There have been two approaches to suppress the reduction problem. One utilizes dopant modification. For example, the stability has been improved by about two orders of magnitude by doping 3 mol % Pr in $Ce_{0.8}Gd_{0.2}O_{2-\delta}$.[22] The other way is to coat the fuel side of the doped ceria with a YSZ thin film which is stable in reducing atmosphere.[23,24]

Recently, Sr- and Mg- doped $LaGaO_3$ (LSGM) with a perovskite structure has been reported as a superior oxide ion conductor.[25-27] While the A-site cation is surrounded by 12 oxygen ions in the ABO_3 perovskite structure, the B-site cation is located in the center of an oxygen octahedron which is connected three dimensionally with corner sharing. The ideal cubic ABO_3 perovskite structure is illustrated in Figure 1.4.

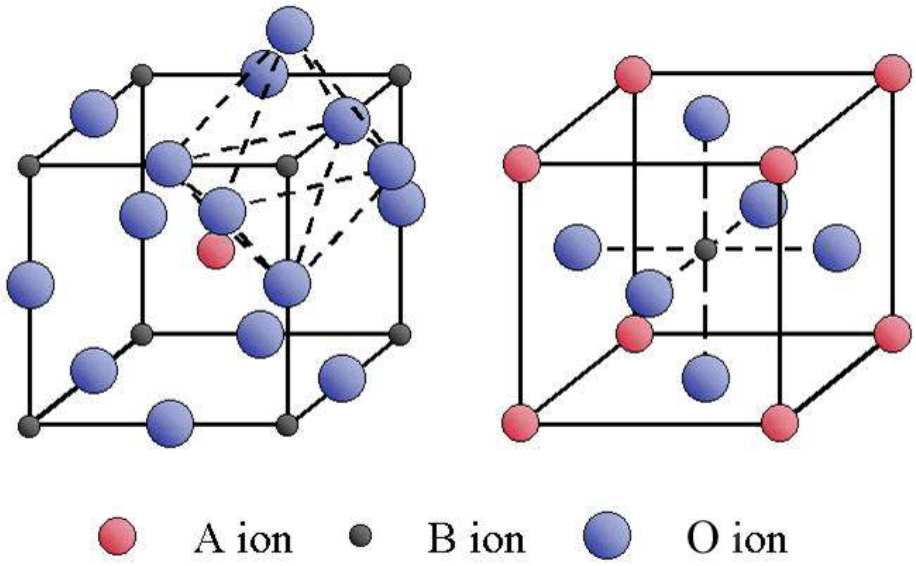

Figure 1.4 The ideal cubic perovskite structure of ABO_3.

LSGM exhibits high oxide ion conductivity of > 0.1 S/cm at 800 ^{o}C, which is similar to that of YSZ at 1000 ^{o}C. It is also very stable without electronic conductivity in a wide range of oxygen partial pressures. Therefore, LSGM is considered as a promising electrolyte for intermediate temperature SOFC. Nevertheless, the high cost of Ga_2O_3 is still a major obstacle for the commercialization prospects of LSGM.

1.3.2 Anode

Among the SOFC components, the porous anode provides electrochemical reaction sites for the oxidation of fuel (*e.g.* H_2 or hydrocarbon). Therefore, anode materials must not only be thermally and chemically stable in a reducing atmosphere but also have good catalytic activity toward oxidation or reforming of fuel gases.

SOFC commonly uses a porous cermet anode consisting of about 40 vol % Ni dispersed in YSZ (Ni-YSZ).[28] While YSZ provides the necessary oxide ion conductivity, the continuously connected Ni provides the electronic conductivity. Although Ni serves as an excellent catalyst for the electrochemical oxidation of the hydrogen fuel, it experiences problems with hydrocarbon fuels. Direct use of hydrocarbon fuels leads to the deposition of carbon and a strong adsorption of H_2S on the Ni particles, which leads to huge activation polarization and severe performance loss.

Both doped and undoped ceria have been found to show high activity towards steam reforming of methane with the onset of methane reforming occurring at temperatures as low as 210 ^oC.[29-31] Furthermore, a three-component anode consisting of YSZ, ceria, and Cu has been found to exhibit good activity towards the electrochemical oxidation of a variety of dry hydrocarbon gases with suppressed carbon deposits.[32] Thus, Cu is a better catalyst than Ni for the oxidation of hydrocarbons.

In an effort to develop alternative new anodes that can withstand sulfur contamination and carbon deposition with hydrocarbon fuels, perovskite oxides based on Cr have also drawn attention recently. For example, $La_{0.8}Sr_{0.2}Cr_{0.97}V_{0.03}O_3$-YSZ has been shown to exhibit electrochemical performance similar to that of Ni-YSZ with excellent resistance to carbon deposition.[33]

1.3.3 Cathode

Due to the high corrosivity of oxygen at high operating temperatures and the slow oxygen reduction reaction, cathodes have more significant material limitations than any other cell component. The key requirements of cathode materials for SOFC are the following:

- The cathode material should be thermodynamically stable in the oxidizing environment and at high operating temperature.
- The cathode material must have sufficient electronic conductivity to sustain electron flow for charge transfer and to reduce the ohmic loss at the operating temperature.
- The cathode material should be chemically stable and compatible with other components such as the electrolyte and interconnect to minimize chemical interaction or elemental diffusion.
- The thermal expansion of the cathode material must match with that of the adjoining components to avoid cracking and delamination during fabrication and operation.
- The cathode must have sufficient porosity to allow gas transport to reaction sites.

- The cathode material must have sufficient catalytic activity in order to reduce the electrode polarization for the oxygen reduction reaction.

Since Sr-doped lanthanum manganite (LSM) has high electrochemical activity for the O_2 reduction reaction and good stability with electrolyte such as YSZ, Sr-doped $LaMnO_3$ has been known as a state-of-the-art cathode material for SOFC.[14,34] Sr doping on $LaMnO_3$ enhances its electronic conductivity by increasing the Mn^{4+} content through a substitution of a lower valence cation Sr^{2+} for La^{3+} cation:

$$LaMnO_3 \xrightarrow{xSrO} La_{1-x}^{3+} Sr_x^{2+} Mn_{1-x}^{3+} Mn_x^{4+} O_3 \qquad (1.13)$$

Thus, LSM exhibits p-type semiconducting behavior.

The chemical stability of LSM for YSZ electrolyte is also acceptable.[35,36] The thermal expansion coefficient of LSM can be modified by Sr content from 11.2 to 12.8 $\times$ 10^{-6} $^{o}C^{-1}$, which makes it compatible with that of YSZ.[37] However, the oxide ion vacancy concentration is low as shown in Figure 1.5, and the oxygen self diffusion coefficient is about 10^{-15} to 10^{-12} cm^2/s in the temperature range of 700 ^{o}C to 900 ^{o}C.[38,39] Thus, LSM exhibits a low oxide ion conductivity value of 5 $\times$ 10^{-7} to 8 $\times$ 10^{-8} S/cm at 900 ^{o}C in air.[40] The rather low oxide ion conductivity of LSM leads to a decrease in catalytic activity toward the oxygen reduction reaction at lower temperatures. Therefore, LSM is not adequate as a cathode material for intermediate temperature SOFC.

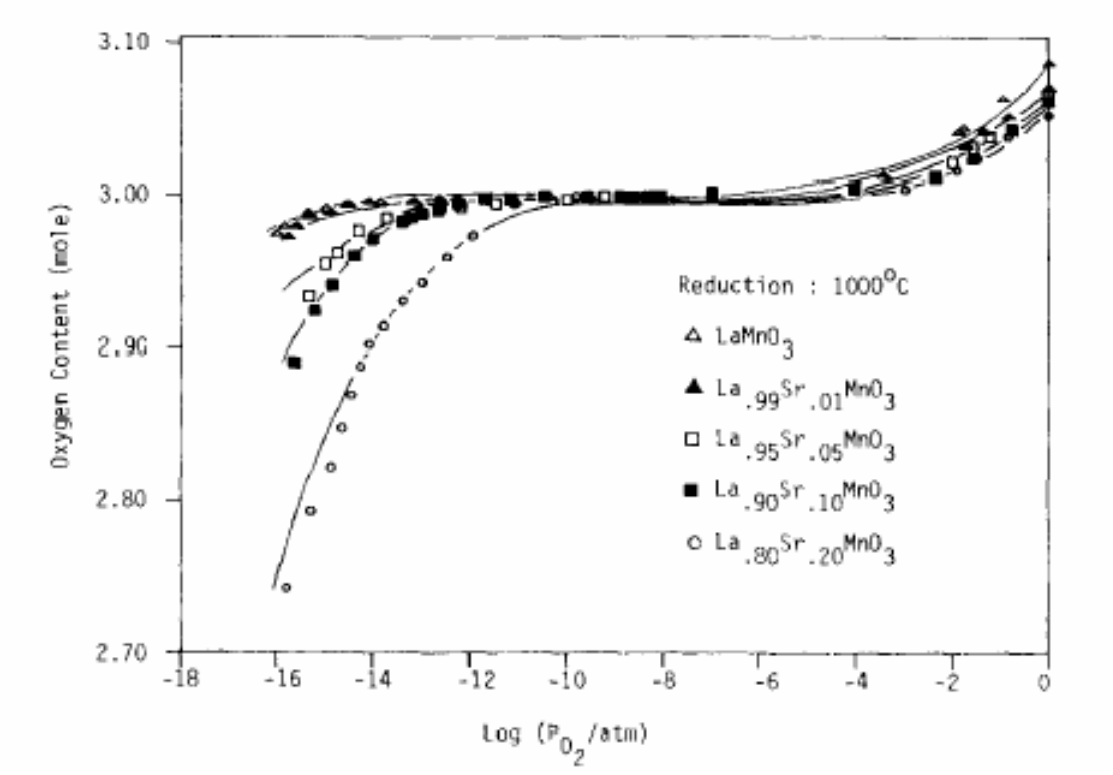

Figure 1.5 Oxygen content of $La_{1-x}Sr_xMnO_3$ as a function of Log p_{O2} at 1000 ^oC.[38]

Recently, Sr-doped lanthanum cobaltite (LSC) has been investigated extensively due to its high electronic and oxide ion conductivity. The electronic conductivity of LSC is about 1200 S/cm at 1000 ^oC.[41,42] Undoped $LaCoO_3$ is a p-type semiconductor, but shows a semiconductor to metal transition at about 800 ^oC in oxygen atmosphere.[43] The transition temperature could be lowered by doping with Sr, and above 30 mol % Sr, LSC exhibits a metallic conductivity from room temperature to 1000 ^oC.[41,44] When doped with Sr, LSC becomes oxygen deficient, and the deficiency increases with increasing temperature, decreasing oxygen partial pressure,

and increasing Sr content as shown in Figure 1.6.[45] LSC exhibits a high oxide ion conductivity value of 1.1×10^{-5} to 1.3×10^{-3} S/cm at 700 ^{o}C.[46,47] Therefore, LSC is more favorable as a cathode material for intermediate temperature SOFC than LSM.

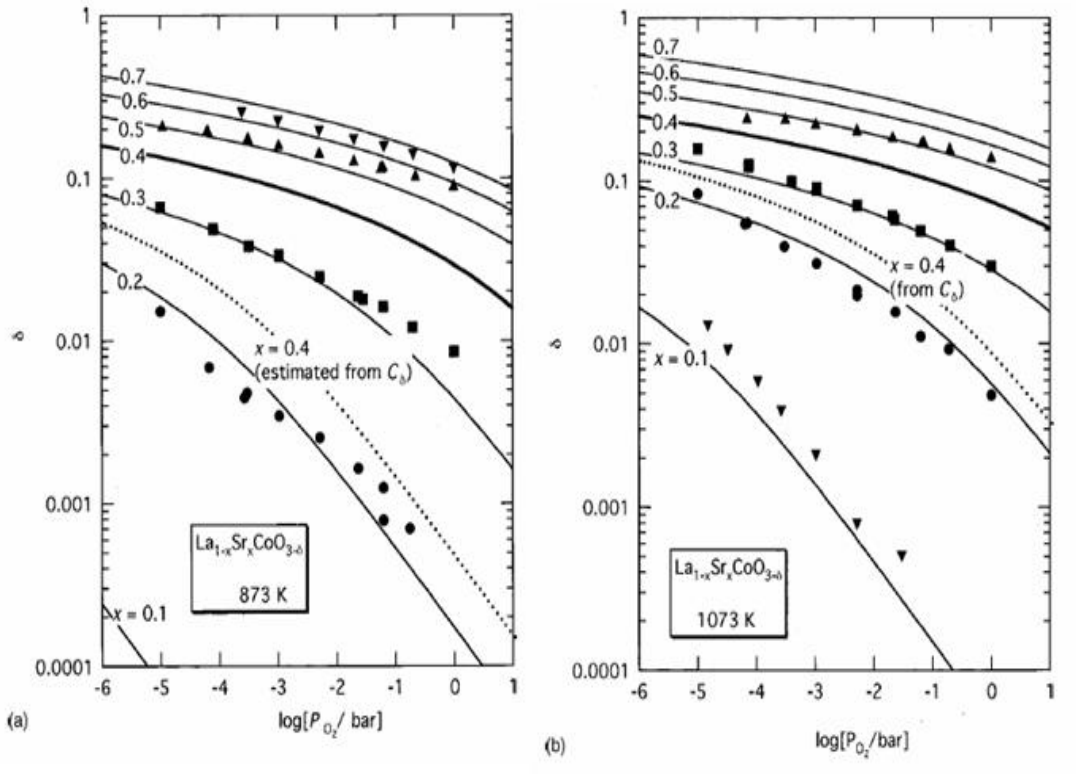

Figure 1.6 Oxygen nonstoichiometry δ in $La_{1-x}Sr_xCoO_{3-\delta}$ at (a) 873 K and (b) 1073 K.[45]

However, LSC readily reacts with YSZ to form a resistive phase such as $La_2Zr_2O_7$ or $SrZrO_3$ at high temperature,[35,48] and the thermal expansion coefficient of LSC (22 to 24×10^{-6} $^{o}C^{-1}$) is significantly higher than that of YSZ.[44,49] Therefore, the main issue

of the LSC cathode is to decrease the thermal expansion coefficient mismatch with the electrolyte.

1.4 MOTIVATION AND OBJECTIVE OF THIS WORK

Despite important advantages, the SOFC technology is confronted with a few challenges. Conventional SOFC technology uses the zirconia-based electrolytes such as the yttria-stabilized zirconia, $Zr_{1-x}Y_xO_{2-0.5x}$ (YSZ), which necessitate a high operating temperature of around 1000 ^oC to realize adequate oxide ion conductivity and power density. Such a high operating temperature of around 1000 ^oC leads to several difficulties: (i) limitation in the choice of cathode, anode, and interconnect materials due to undesirable interfacial reactions among them, (ii) thermal expansion mismatch among the electrolyte and electrodes and consequent degradation in mechanical properties, (iii) problems with sealing, and (iv) long-term stability and durability. These difficulties can be overcome or minimized, while still preserving the important advantage of using hydrocarbon fuels directly, by lowering the operating temperatures to 500-800 ^oC. However, one of the major issues with the intermediate temperature SOFC is the slow oxygen reduction kinetics and the consequent high over-potential at the cathode.

To overcome this difficulty, several perovskite oxides based on Co such as $La_{1-x}Sr_xCoO_{3-\delta}$ have been pursued in recent years, but oxides with high Co content lead to high thermal expansion and high chemical reactivity. So the main objective of

this study is to design and develop efficient cathode materials with relatively low thermal expansion and good catalytic activity.

Specifically, the objective of this study is to

- investigate the $Ln_{1-x}Sr_xCoO_{3-\delta}$ (Ln = La, Pr, Nd, Sm, and Gd) and $Nd_{0.6}Sr_{0.4}Co_{1-y}M_yO_{3-\delta}$ (M = Fe and Mn) perovskite oxide cathodes, incorporate metallic Ag into porous perovksite oxide cathodes, and explore new perovskite-related intergrowth oxides such as $LaSr_3Fe_{3-y}Co_yO_{10-\delta}$ and $Sr_{3-x}La_xFe_{2-y}Co_yO_{7-\delta}$
- characterize them by a variety of physical techniques (diffraction, wet-chemical analysis, microscopy, spectroscopy, electrical and ionic transport, thermal analysis)
- evaluate their performance with single cell SOFCs and
- develop a fundamental understanding of the structure-property-performance relationships.

CHAPTER 2

EXPERIMENTAL TECHNIQUES

2.1 MATERIALS SYNTHESIS

The various cathode materials presented in this dissertation were synthesized by conventional solid-state reaction or coprecipitation methods. The conditions and procedures of synthesis varied depending on each system. While the general procedures are given in this chapter, more details of synthesis will be given in the relevant chapters.

NiO-$Ce_{0.9}Gd_{0.1}O_{1.95}$ (GDC) cermet (Ni:GDC = 70:30 vol %) anode was synthesized by the glycine-nitrate combustion method.[50] The method involved the addition of glycine to a dilute nitric acid solution of required amounts of Gd_2O_3, CeO_2, and $Ni(CH_3COO)_2 \cdot 4H_2O$, followed by an evaporation of water and a self-sustaining combustion of the solid mass on a hot plate. The residual carbon was then removed by calcining at 600 ^oC for 3 h in air.

The $La_{0.8}Sr_{0.2}Ga_{0.8}Mg_{0.2}O_{2.8}$ (LSGM) electrolyte was prepared by firing required amounts of La_2O_3, $SrCO_3$, Ga_2O_3, and MgO at 1100 ^oC for 5 h, followed by pelletizing and sintering at 1500 ^oC for 10 h.

2.2 MATERIALS CHARACTERIZATION

The materials synthesized were characterized by a variety of techniques. A more general description of the techniques is provided in this chapter, and any specific details will be presented in the respective chapters.

2.2.1 X-ray Powder Diffraction (XRD)

X-ray powder diffraction was carried out using a Philips Model APD 3520 X-ray diffractometer with Cu Kα radiation. Diffraction patterns were recorded with variable slit values in the 2θ range of 20° to 80° with a stepwise scan method (scan rate of 0.05^{o} per 2 seconds) and then converted to fixed variable values. Crystal chemistry of the samples was analyzed by the Rietveld refinement method with the DBWS-9411 program.[51] The average crystallite size was estimated from the line broadening in the X-ray diffraction patterns using the Scherrer equation,[52]

$$Crystallite\ size = \frac{0.9\lambda}{FW \cdot \cos\theta} \tag{2.1}$$

where λ is the wavelength of the incident radiation and FW is the full width in radians at half maximum.

2.2.2 Iodometric Titration

The oxygen content and average oxidation state of the transition metal ions at room temperature were determined by iodometric titration.[53] The fine sample powders were dissolved in 15 mL of 10 % KI solution. After adding 10 mL of 3.5 N HCl, the solution was stirred until the sample dissolved completely. The clear solution was then titrated against 0.03 N sodium thiosulfate ($Na_2S_2O_3$) solution using starch as an indicator.

2.2.3 Surface Area and Density Measurement

The surface area of the powder was measured with a Quantachrome Autosorb-1 surface area and pore size analyzer using the Brunauer-Emmett-Teller (BET) method. After removing the pre-adsorbed gases in vacuum at 200 ^{o}C, the measurement was carried out using nitrogen gas as an adsorbate. The bulk densities of sintered samples were measured by the Archimedes method.

2.2.4 Thermal Analysis

Weight changes and thermal expansion behavior of the samples during heating and cooling were monitored, respectively, with a Perkin-Elmer Series 7 thermogravimetric analyzer (TGA) and a thermomechanical analyzer (TMA). TGA was carried out from room temperature to 1000 ^{o}C with a heating rate of 2 ^{o}C/min and

a cooling rate of 10 ^{o}C/min in air. Thermal expansion data were generally obtained from room temperature to 700 ^{o}C with a heating/cooling rate of 10 ^{o}C/min in air.

2.2.5 Electrical Conductivity Measurement

The electrical conductivity was measured from 200 to 900 ^{o}C at 20 ^{o}C increment with a four-probe dc method using the Van der Pauw configuration[54,55] The schematic Van der Pauw configuration is shown in Figure 2.1. The specific resistivity ρ of a flat sample can be calculated by

$$\rho = \frac{\pi d}{\ln 2} \frac{(R_{AB,CD} + R_{BC,DA})}{2} f\left(\frac{R_{AB,CD}}{R_{BC,DA}}\right) \tag{2.2}$$

where R is the resistance, and d is the thickness of the sample, and f is a function of the ratio $R_{AB,CD}/R_{BC,DA}$ (see Figure 2.1)

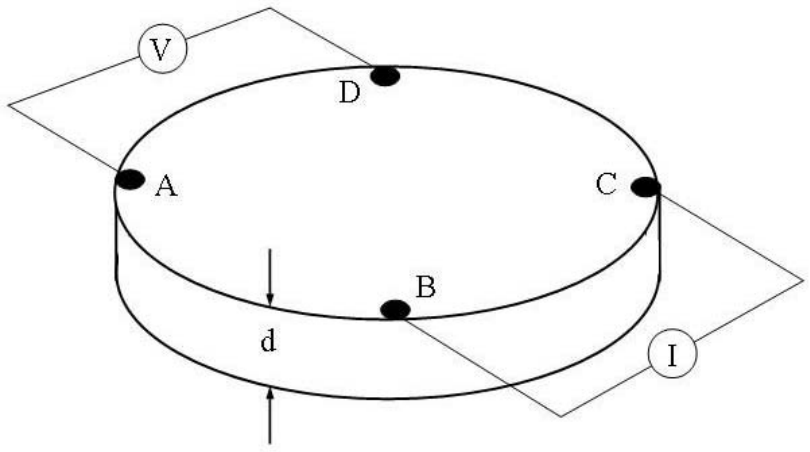

Figure 2.1 Schematics of the Van der Pauw configuration.

Assuming the four probes are equally located in a square on a disc type sample, $f\left(\frac{R_{AB,CD}}{R_{BC,DA}}\right)$ equals to 1, and then the conductivity σ can be calculated as

$$\sigma = \frac{1}{\rho} = 0.2207 \frac{I}{V \cdot d} \tag{2.3}$$

where I is the applied current, V is the measured voltage, and d is the sample thickness.

2.2.6 Scanning Electron Microscopy (SEM)

Microstructural characterization of the cathodes and the interfacial reaction analysis were carried out with a JEOL LSM-5610 scanning electron microscope (SEM) equipped with an OXFORD Instruments INCA Energy 200 X-ray detector for elemental analysis by energy dispersive spectroscopy (EDS).

2.3 ELECTROCHEMICAL CHARACTERIZATION

Electrochemical performances were evaluated with single cells at 800 ^{o}C and AC impedance analysis at various temperatures.

2.3.1 Fabrication of Single Cells

The sintered LSGM electrolyte pellets with densities of > 95% of the theoretical value were ground and polished to 0.7-1.0 mm thickness. The electrode powders synthesized were ball milled for 24 h in ethanol using a zirconia milling media. The various cathodes and NiO-GDC cermet anode were then prepared by screen printing the slurries consisting of 60 wt. % ball milled cathode or anode powder and 40 wt. % organic binder (Heraeus V006) onto the LSGM electrolyte pellet, followed by firing for 3 h at 920-1100 ^{o}C for the cathodes and 1200 ^{o}C for the anode. The specific firing temperature of various cathode compositions will be described in the respective chapters. The geometrical area of the electrode was 0.25 cm^2.

2.3.2 Single Cell Performance Test

Current-voltage (I-V) measurements were carried out with a three electrode configuration consisting of Pt paste as the reference electrode, which allowed a separation and monitoring of the cathode over-potentials during the cell operation. The schematic configuration of the test cell is shown in Figure 2.2.

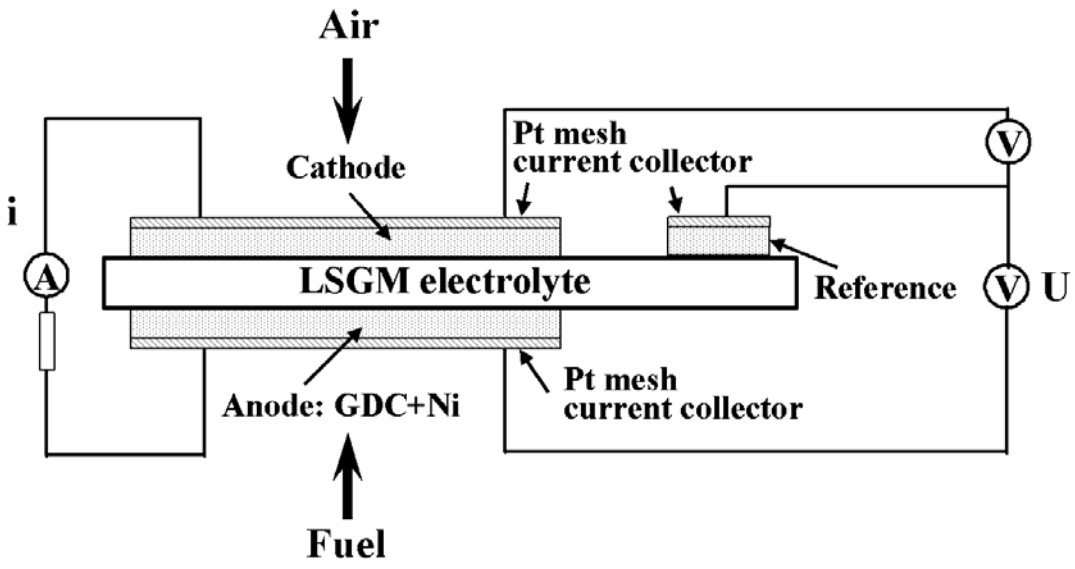

Figure 2.2 Schematic configuration of the test single cell.

Pt mesh was attached to the top of the electrodes as a current collector and Pt wire was used as terminals. In order to keep the current collector and electrode in good contact, a spring was used to press the Pt mesh onto the electrode via a porous alumina disk. Sealing between the single cell and the alumina tube was achieved with a pyrex glass ring. The schematic configuration of the test stand is shown in Figure 2.3.

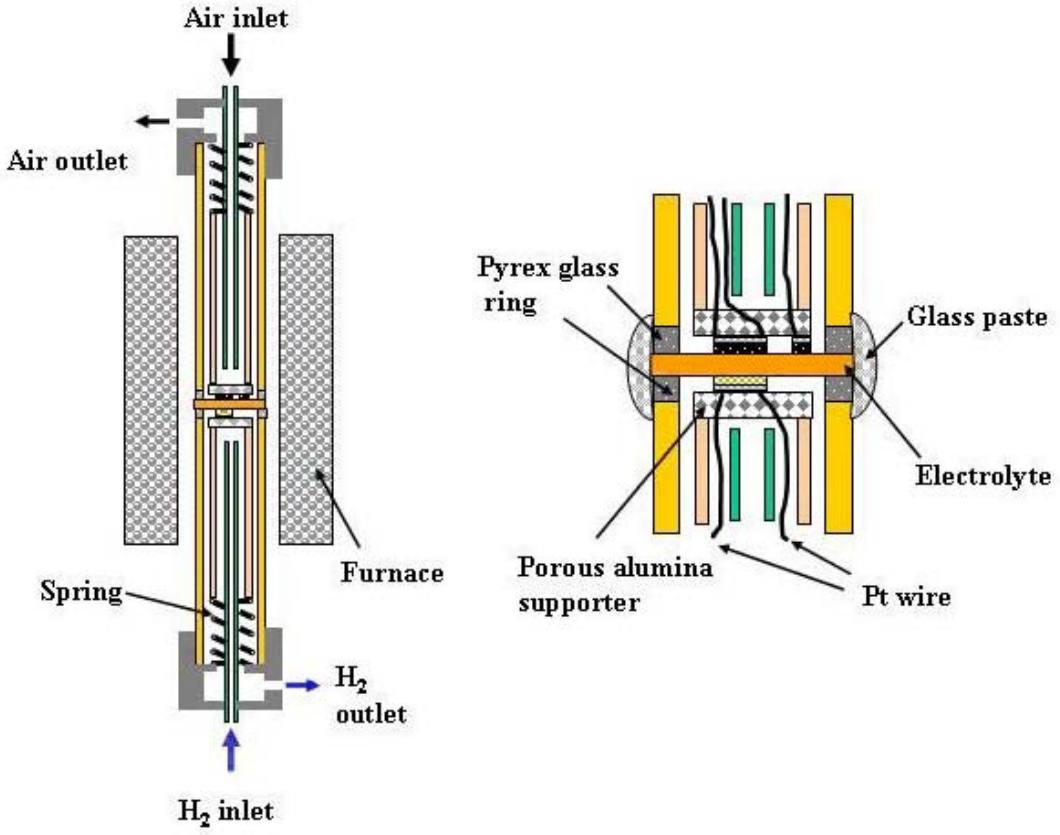

Figure 2.3 Schematic configuration of the test stand.

Humidified H_2 (~3% H_2O at 30 ^oC) and air were supplied as fuel and oxidant, respectively, at a rate of 100 cm^3/min. NiO in the anode was reduced to Ni in humidified H_2 before the single cell test. I-V and cathode over-potentials were measured *in situ* during cell operation with an Arbin BT2000/fuel cell test station.

2.3.3 AC Impedance Measurement

AC impedance was measured in air by a potentiostat having a frequency response analyzer with a three electrode configuration, and the test cell geometry and configuration were same as that used for the single cell performance test. Pt paste was used as both the counter and the reference electrodes, and the applied frequency was in the range of 0.5 mHz to 1 MHz with an voltage amplitude of 10 mV.

PART I

PEROVSKITE OXIDE CATHODE MATERIALS FOR INTERMEDIATE TEMPERATURE SOFC

CHAPTER 3

COMPARISON OF $Ln_{0.6}Sr_{0.4}CoO_{3-\delta}$ (Ln = La, Pr, Nd, Sm, AND Gd) PEROVSKITE OXIDE CATHODE MATERIALS

3.1 INTRODUCTION

Solid oxide fuel cells (SOFC) have attracted much attention because of their high energy conversion efficiency, environmental compatibility, and ability to use hydrocarbon fuels directly without external reforming. However, the chemical reactivity and thermal expansion mismatch among the components as well as the limited choice of interconnect and cathode materials at the conventional operating temperatures (~ 1000 ^{o}C) of SOFC are major obstacles. These difficulties have created enormous interest recently in intermediate temperature (500-800 ^{o}C) SOFC.[14] However, the performance of the intermediate temperature SOFC is strongly dependent on the electrochemical properties of the cathode materials since the cathode over-potential for the oxygen reduction reaction (ORR) increases significantly at lower temperatures.[56] Therefore, there is a need to develop alternate mixed ionic-electronic conductors that can replace the conventional $La_{1-x}Sr_xMnO_3$ cathodes.

A desirable cathode material for the intermediate temperature SOFC should have high electronic and oxide ion conductivities, chemical and thermal expansion compatibility with the electrolyte, and high catalytic activity for the oxygen reduction

reaction. In this regard, the Sr-doped lanthanum cobaltites ($La_{1-x}Sr_xCoO_{3-\delta}$) have been investigated intensively due to their high electronic and oxide ion conductivities.[45,57] However, the $La_{1-x}Sr_xCoO_{3-\delta}$ cathodes exhibit a large thermal expansion coefficient (TEC) and react readily with the YSZ electrolyte.[48,58] Accordingly, other Sr-doped lanthanide cobaltites $Ln_{1-x}Sr_xCoO_{3-\delta}$ (Ln = Lanthanide) have also been investigated as cathode materials for intermediate temperature SOFC.[59-64] Despite a scattered investigation of the $Ln_{1-x}Sr_xCoO_{3-\delta}$ cathodes, a systematic investigation of the factors that control their electrocatalytic activity towards the oxygen reduction reaction is scarcely available in the literature. With this perspective, a comparison of the crystal chemistry, thermal expansion, electrical conductivity, chemical compatibility, and electrochemical performance of the $Ln_{0.6}Sr_{0.4}CoO_{3-\delta}$ (Ln = La, Pr, Nd, Sm, and Gd) cathodes and a correlation of the electrochemical performance to the lanthanide host cations are presented in this chapter. Additionally, the differences in the influence of the Ln^{3+} ions on the properties of the $Ln_{1-x}Sr_xCoO_{3-\delta}$ and $Ln_{1-x}Sr_xMnO_3$ systems are discussed.

3.2 EXPERIMENTAL

3.2.1 Materials Synthesis

The $Ln_{0.6}Sr_{0.4}CoO_{3-\delta}$ (Ln = La, Pr, Nd, Sm, and Gd) cathode samples were synthesized by a conventional solid-state reaction method. Required amounts of the

lanthanide oxides (La_2O_3, Pr_6O_{11}, Nd_2O_3, Sm_2O_3, or Gd_2O_3), $SrCO_3$, and Co_3O_4 were thoroughly mixed with ethanol using an agate mortar and pestle, and calcined in air first at 900 ^oC for 12 h. The calcined powders were then ground, pressed into pellets, and finally sintered at 1200 ^oC for 24 h. The sintering at 1200 ^oC was repeated again for 24 h after regrinding and repelletizing to improve the product homogeneity. The $La_{0.8}Sr_{0.2}Ga_{0.8}Mg_{0.2}O_{2.8}$ (LSGM) electrolyte and the NiO-$Ce_{0.9}Gd_{0.1}O_{1.95}$ (GDC) cermet (Ni:GDC = 70:30 vol %) anode powder were prepared by solid-state reaction and glycine-nitrate combustion method, respectively, as described in Chapter 2.

3.2.2 Fabrication of Single Cells

The $Ln_{0.6}Sr_{0.4}CoO_{3-\delta}$ cathodes and NiO-GDC cermet anode were prepared by screen printing onto 1.0 mm thick LSGM electrolyte pellet, as described in Chapter 2, followed by firing for 3 h at 1000 ^oC for the cathode and 1200 ^oC for the anode.

3.2.3 Characterization

The products obtained were characterized by XRD, BET surface area, SEM, iodometric titration to determine the oxidation state and oxygen content, TGA, TMA, electrical conductivity, and electrochemical single cell measurements as described in Chapter 2. For iodometric titration, the powders were ball milled and sieved a few times to obtain fine powders so that they could be dissolved in a mixture of 10 % KI and 3.5 N HCl. The specimens for the reactivity tests were obtained by mixing the

cathode powders with the LSGM electrolyte in a 1:1 weight ratio. The reactivity tests were then carried out at 1000 ^{o}C for 3 h in air.

3.3 RESULTS AND DISCUSSION

3.3.1 Crystal Chemistry and Oxygen Content

X-ray diffraction patterns of the $Ln_{0.6}Sr_{0.4}CoO_{3-\delta}$ (Ln = La, Pr, Nd, Sm, and Gd) samples are shown in Figure 3.1. All the samples are single phase perovskite solid solutions without any detectable impurity phases, which is consistent with the report of Ohbayashi *et al.*[64] While the Ln = La sample was found to be rhombohedral, all others with Ln = Pr, Nd, Sm, and Gd were found to be orthorhombic. The lattice parameters, lattice volume, pseudo-cubic lattice parameter, and tolerance factor *t* for all the $Ln_{0.6}Sr_{0.4}CoO_{3-\delta}$ samples are summarized in Table 3.1. The pseudo-cubic lattice parameter decreases from Ln = La to Gd due to a decrease in the ionic radius of the Ln^{3+} ion. The Goldschmidt tolerance factor *t* can be used as a measure of the deviation of the ABO_3 perovskite structure from the ideal cubic symmetry:

$$t = \frac{r_A + r_O}{\sqrt{2}(r_B + r_O)} \tag{3.1}$$

where r_A, r_B, and r_O are, respectively, the radii of A^{3+}, B^{3+}, and O^{2-} ions.

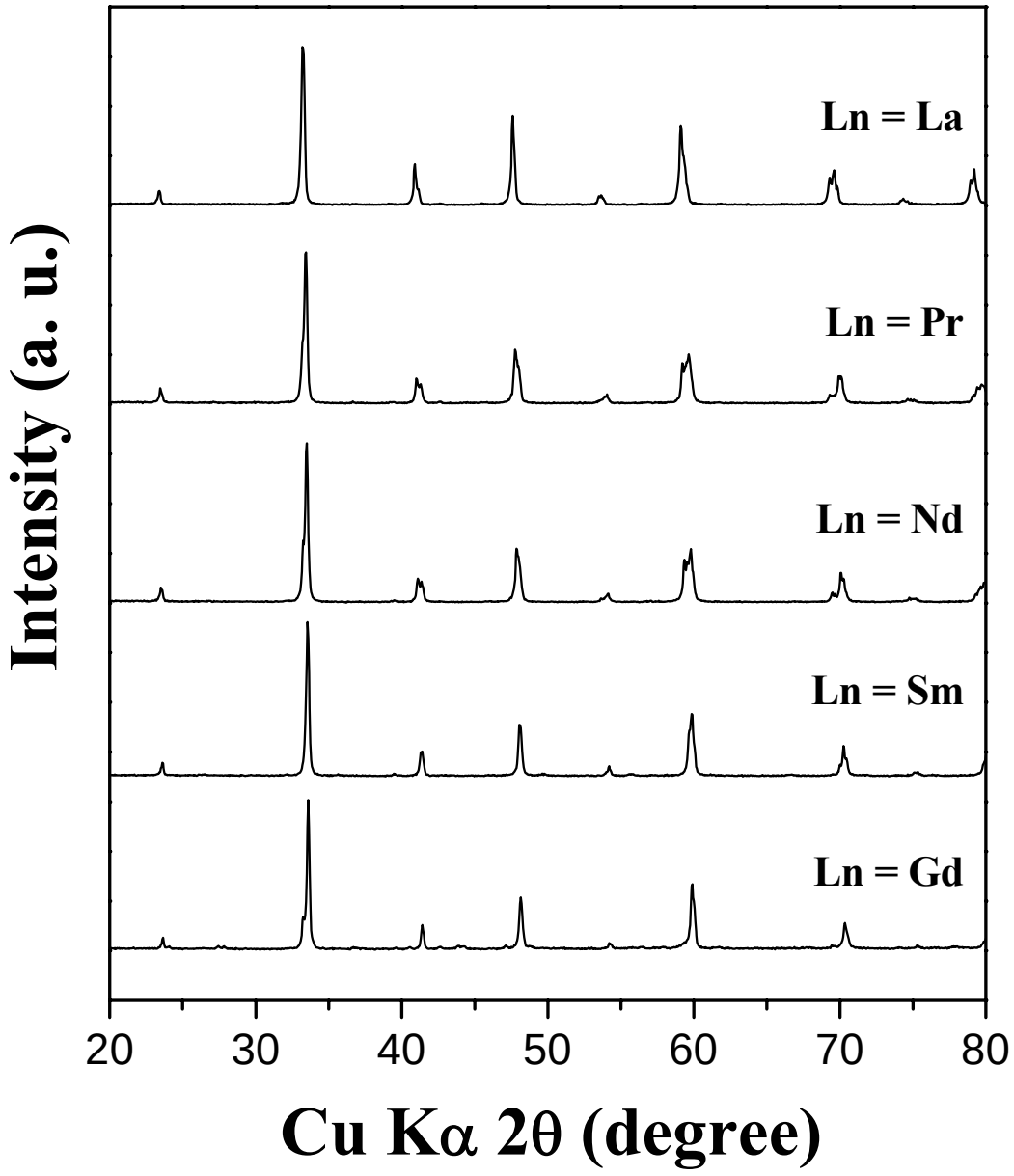

Figure 3.1 X-ray diffraction patterns of $Ln_{0.6}Sr_{0.4}CoO_{3-\delta}$ (Ln = La, Pr, Nd, Sm, and Gd) sintered at 1200 ^{o}C for 24 h.

For an ideal matching, *t* should be equal to unity and *t* generally increases with temperature due to a larger thermal expansion of the more ionic A-O bonds compared to the B-O bonds. In the $Ln_{0.6}Sr_{0.4}CoO_{3-\delta}$ (Ln = La, Pr, Nd, Sm, and Gd) system, a decreasing *t* due to a decreasing ionic radius from La^{3+} to Gd^{3+} causes a lowering of the crystal symmetry and an increasing bending of the O-Co-O bond angle from the ideal value of 180^{o}.

The average oxidation state of Co and the oxygen content values determined at room temperature by the iodometric titration are given in Table 3.1 for the $Ln_{0.6}Sr_{0.4}CoO_{3-\delta}$ oxides. The oxygen contents remain at 3.0 irrespective of the lanthanide ion. The TGA plots comparing the variations of the oxygen contents in $Ln_{0.6}Sr_{0.4}CoO_{3-\delta}$ with temperature are shown in Figure 3.2. The degree of oxygen loss decreases from Ln = La to Gd, suggesting a stronger binding of the oxide ions to the lattice. This is consistent with a report that the enthalpies of formation of solid oxides (Ln_2O_3) and their lattice energies increase from Ln = La to Gd.[65] The TGA data implies that the tendency for oxygen nonstoichiometry (vacancy concentration) in $Ln_{0.6}Sr_{0.4}CoO_{3-\delta}$ (Ln = La, Pr, Nd, Sm, and Gd) decreases in the order La > Pr > Nd > Sm > Gd.

Table 3.1 Lattice parameters, lattice volume, pseudo-cubic lattice parameter (*a'*), tolerance factor (*t*), and chemical analysis data of $Ln_{0.6}Sr_{0.4}CoO_{3-\delta}$.

Ln	*a* (Å)	*b* (Å)	*c* (Å)	Lattice volume ($Å^3$)	*a'* (Å)	*t*	Oxidation state of Co	Oxygen content (3-δ)
La[a]	5.4079(4)	-	-	112.5	4.8274	0.965	3.38	2.99
Pr	5.3733(5)	5.4240(5)	7.5962(8)	221.4	3.8110	0.957	3.39	3.00
Nd	5.3656(5)	5.4148(4)	7.5917(7)	220.6	3.8064	0.953	3.38	2.99
Sm	5.3564(6)	5.3814(5)	7.5792(8)	218.5	3.7943	0.946	3.39	3.00
Gd	5.3578(9)	5.3654(4)	7.5718(8)	217.7	3.7897	0.941	3.40	3.00

[a] Rhombohedral cell angle, $\alpha = 60.28^o$

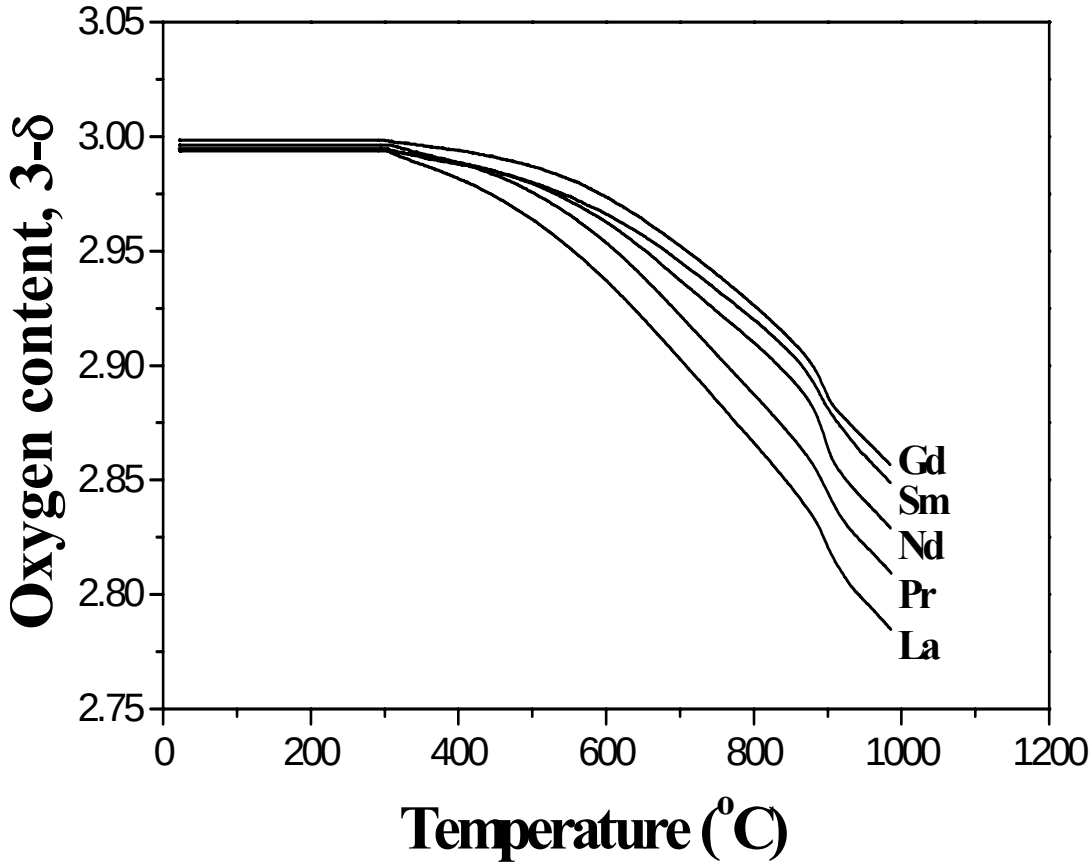

Figure 3.2 Comparison of the TGA plots of $Ln_{0.6}Sr_{0.4}CoO_{3-\delta}$ (Ln = La, Pr, Nd, Sm, and Gd) recorded in air with a heating rate of 2 ^{o}C/min.

3.3.2 Electrical Conductivity

The temperature dependence of the electrical conductivity of $Ln_{0.6}Sr_{0.4}CoO_{3-\delta}$ (Ln = La, Pr, Nd, Sm, and Gd) is shown in Figure 3.3. All the samples exhibit a metallic-conducting behavior and have conductivity values of > 800 S/cm at 800 ^{o}C. The faster decrease in conductivity at higher temperatures could be due to the formation of significant amount of oxide ion vacancies as indicated by the TGA data (Figure 3.2). The formation of oxide ion vacancies is accompanied by a reduction of Co^{4+} to Co^{3+}, resulting in a decrease in the charge carrier concentration and Co-O covalency. Also, the oxide ion vacancies will perturb the O-Co-O periodic potential and covalent interaction.[66] These factors lead to a decrease in electrical conductivity at elevated temperatures.

At a given temperature, the electrical conductivity of the $Ln_{0.6}Sr_{0.4}CoO_{3-\delta}$ (Ln = La, Pr, Nd, Sm, and Gd) samples decreases from Ln = La to Gd. This can be understood by considering the changes in the structural parameters. As seen in Table 3.1, the decreasing tolerance factor *t* with decreasing ionic radius from La^{3+} to Gd^{3+} increases the bending of the O-Co-O bonds (lowers the O-Co-O bond angle from 180^{o}), which results in a decrease in the overlap between the $Co^{3+/4+}$:3d and O^{2-}:2p orbitals and bandwidth. Thus the decreasing covalency of the Co-O bonds and the increasing electron localization from Ln = La to Gd causes a decrease in electrical conductivity.

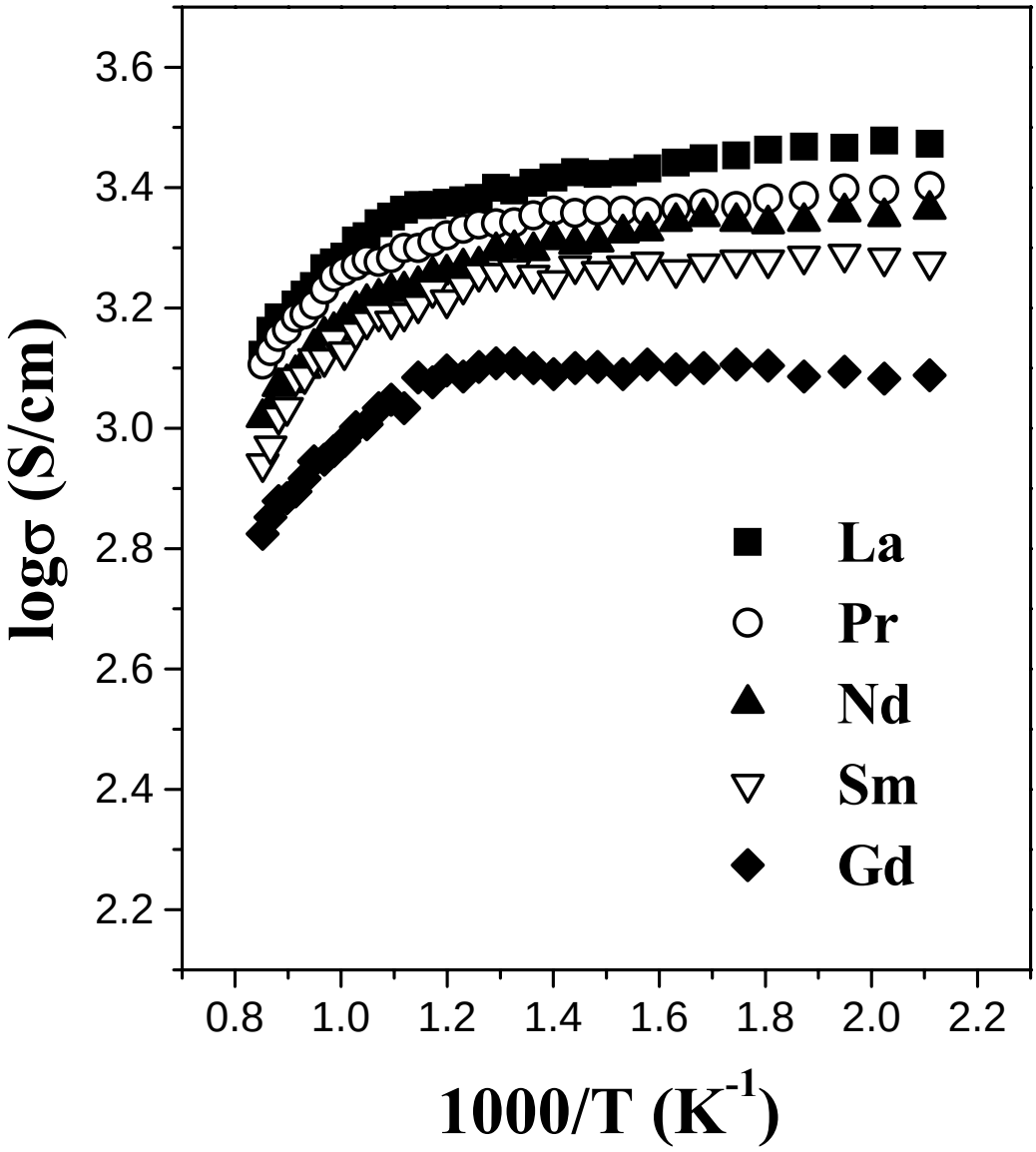

Figure 3.3 Comparison of the temperature dependence of the electrical conductivity of $Ln_{0.6}Sr_{0.4}CoO_{3-\delta}$ (Ln = La, Pr, Nd, Sm, and Gd) in air.

3.3.3 Thermal Expansion Behavior

The average thermal expansion coefficients (TECs) of the $Ln_{0.6}Sr_{0.4}CoO_{3-\delta}$ samples measured in the range of 50-800 ^{o}C in air are given in Table 3.2. The TEC value decreases from Ln = La to Gd. A similar trend has been observed in the analogous $Ln_{1-x}Sr_xMnO_3$[67] and $Ln_{0.8}Sr_{0.2}Fe_{0.8}Co_{0.2}O_3$[68] systems also.

Table 3.2 BET surface area, average crystallite size, and average thermal expansion coefficient (TEC) of $Ln_{0.6}Sr_{0.4}CoO_{3-\delta}$.

Ln	BET surface area (m^2/g)	Average crystallite size [a] (Å)	TEC × 10^{-6} ($^{o}C^{-1}$)
La	4.6	510	21.3
Pr	5.2	480	19.5
Nd	4.0	550	18.7
Sm	3.7	580	18.0
Gd	4.8	500	17.1

[a] Average crystallite size was estimated with the line broadening of XRD peaks, and the error bar is ± 10 Å.

In general, ionic bonds have a larger thermal expansion than the covalent bonds. Therefore, the variations in TEC can be understood by considering the ionic character of the Ln-O bonds. Mori *et al.*[69] have also discussed the variations of TEC in the analogous lanthanum manganites $La_{1-x}A_xMnO_3$ (A = alkaline-earth) in terms of the ionic character of the A-O bond. The percent ionic character of a bond is related to the electronegativity difference between the bonded atoms A and B in the A-B bond by the following empirical relationship:[70]

$$\%\ ionic\ charater = \{1 - \exp[-0.25(x_A - x_B)^2]\} \times 100 \quad (3.2)$$

where x_A and x_B are the electronegativities of the *A* and *B* atoms respectively. Based on the Pauling electronegativity values,[71] one can, therefore, understand that the decreasing TEC from Ln = La to Gd is due to the increasing electronegativity of Ln and the decreasing ionic character of the Ln-O bond from Ln = La to Gd.

Additionally, the variations in TEC could also be related to the tendency to form oxide ion vacancies as the sample is heated. The formation of oxide ion vacancies can cause an increase in TEC due to the reduction of the smaller Co^{4+} ions to the larger Co^{3+} ions.[57,72] Furthermore, TEC is inversely proportional to the binding energy between the ions in the lattice.[73] Hayashi *et al.*[74] have reported that the TEC of GDC increases with the amount of oxide ion vacancies due to a reduction in the binding energy of the metal-oxygen bonds. Therefore, the increasing Ln-O bond strength[65] and the decreasing degree of oxygen loss, as indicated by the TGA data in Figure 3.2, from Ln = La to Gd can be considered to cause a decrease in TEC. In addition, the larger TEC of the cobaltites is partly related to the transition of the Co^{3+} ions from a low spin ($t_{2g}^6 e_g^0$, r = 0.545 Å) to high spin ($t_{2g}^4 e_g^2$, r = 0.61 Å) state.[75] A suppression of such spin state transitions by the decreasing amount of Co^{3+} ions (or decreasing amount of oxide ion vacancies) at elevated temperatures on going from Ln = La to Gd could also contribute to the decreasing TEC.

The influence of the formation of oxide ion vacancies on TEC is also supported by the fact that the decrease in the TEC value on going from Ln = La to Gd in $Ln_{0.6}Sr_{0.4}CoO_{3-\delta}$ (21.3×10^{-6} to 17.1×10^{-6} $^{o}C^{-1}$, measured at 50-800 ^{o}C) is larger than that found with the analogous $Ln_{1-x}Sr_xMnO_3$ system (12.0×10^{-6} to 10.3×10^{-6} $^{o}C^{-1}$, measured at 25-1000 ^{o}C).[67] The increasing tendency to form oxide ion vacancies on going from $Gd_{0.6}Sr_{0.4}CoO_{3-\delta}$ to $La_{0.6}Sr_{0.4}CoO_{3-\delta}$ causes a faster increase (20 %) in TEC in the cobaltite system, while the absence of formation of significant amount of oxygen vacancies in the manganite system for Ln = La – Gd results in a slower increase (14 %) in TEC. Thus, the change in TEC on going from Ln = La to Gd in the manganite system is mainly due to the decreasing ionicity of the Ln-O bond while that in the cobaltite system is due to both the decreasing ionicity of the Ln-O bond and the differences in the formation of oxide ion vacancies. Furthermore, the larger TEC of the cobaltites (~ 20×10^{-6} $^{o}C^{-1}$) compared to that of the manganites (~ 11×10^{-6} $^{o}C^{-1}$) is due to the formation of oxide vacancies, spin state transitions associated with Co^{3+}, and the relatively weaker Co-O bond compared to the Mn-O bond.

3.3.4 Electrochemical Performance

The BET surface area and the average crystallite size of the $Ln_{0.6}Sr_{0.4}CoO_{3-\delta}$ cathode powders do not vary significantly with the Ln^{3+} ions as seen in Table 3.2. Therefore, the influence of the geometrical morphology of the prepared powders on the electrochemical performance could be neglected in this study. Figure 3.4 shows

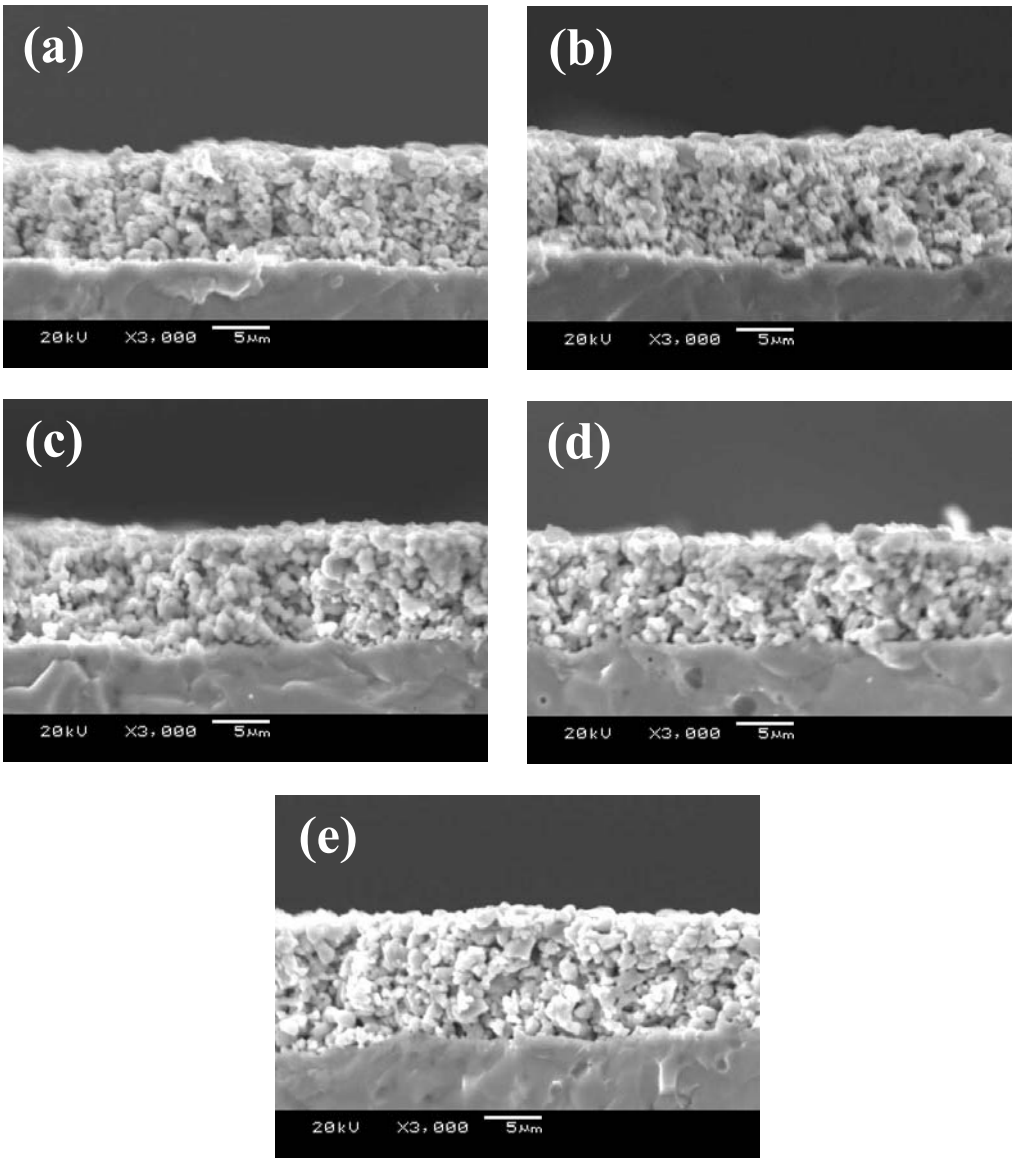

Figure 3.4 SEM micrographs of the $Ln_{0.6}Sr_{0.4}CoO_{3-\delta}$ cathode – LSGM electrolyte assemblies after firing at 1000 ^{o}C for 3 h: (a) Ln = La, (b) Ln = Pr, (c) Ln = Nd, (d) Ln = Sm, and (e) Ln = Gd.

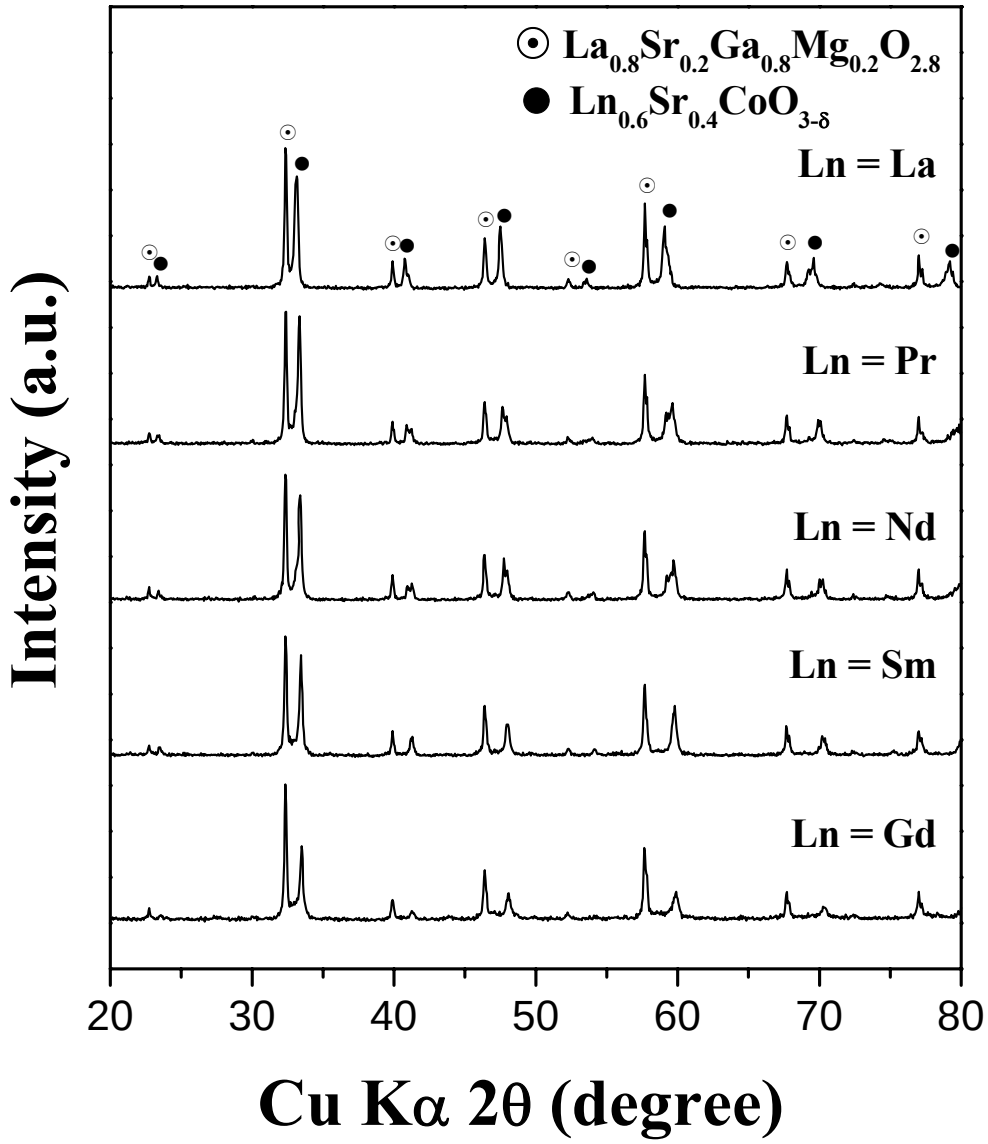

Figure 3.5 X-ray powder diffraction patterns recorded after heating the $Ln_{0.6}Sr_{0.4}CoO_{3-\delta}$ cathode and the LSGM electrolyte powders at 1000 ^{o}C for 3 h.

the SEM micrographs of the $Ln_{0.6}Sr_{0.4}CoO_{3-\delta}$ cathodes after screen printing them onto the LSGM electrolyte followed by firing at 1000 ^{o}C for 3 h. Porous cathode layers of about 10 μm thick with homogeneous microstructure that are well adhered to the dense LSGM electrolyte are seen. In addition, X-ray powder diffraction patterns of the $Ln_{0.6}Sr_{0.4}CoO_{3-\delta}$ and LSGM mixtures after heating at 1000 ^{o}C for 3 h show that there is no interfacial reaction between the cathode compositions and the LSGM electrolyte (Figure 3.5).

The variations of the cell voltage, power density, and over-potential with current density at 800 ^{o}C are compared in Figure 3.6 for the various $Ln_{0.6}Sr_{0.4}CoO_{3-\delta}$ cathodes. The power density decreases and the over-potential increases from Ln = La to Gd. The cathode over-potential for oxygen reduction reaction is closely related to both the electronic and oxide ion conductivities of the cathode materials since the electrocatalytic reaction at a porous cathode is limited by the kinetics of oxygen exchange and diffusion as well as the charge transfer. Both the electrical conductivity (Figure 3.3) and the concentration of oxide ion vacancies (Figure 3.2) decrease from Ln = La to Gd in $Ln_{0.6}Sr_{0.4}CoO_{3-\delta}$; oxide ion conductivity is proportional to the amount of oxide ion vacancies. Additionally, Kharton *et al.*[76] have reported that a decrease in the radius of the Ln^{3+} ions in $Ln_{0.6}Sr_{0.4}CoO_{3-\delta}$ causes a decrease in the size of the anion transfer channel and an increase in the (Ln,Sr)-O bond energy, as evident from the decreasing cell volume in Table 3.1.

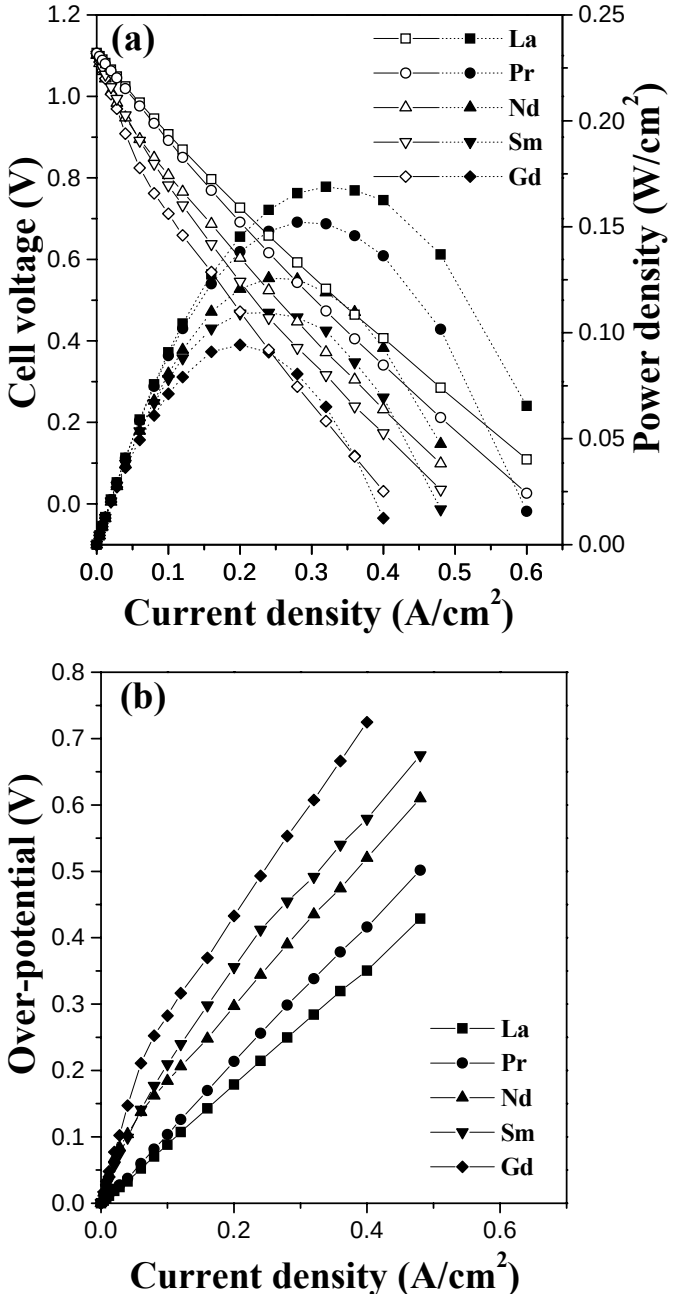

Figure 3.6 Electrochemical performance data of the $Ln_{0.6}Sr_{0.4}CoO_{3-\delta}$/LSGM/Ni-GDC single cells at 800 ^{o}C: variations of the (a) I-V curves (open symbols) and power densities (closed symbols) and (b) cathode over-potential.

This suggests that the oxide ion conductivity of $Ln_{0.6}Sr_{0.4}CoO_{3-\delta}$ would decrease in the order La > Pr > Nd > Sm > Gd, which is consistent with that found by Kharton *et al.*[76] for Ln = La, Pr, and Nd from oxide ion conductivity measurements. Gao *et al.*[77] have also reported that high oxide ion vacancy concentration in the surface of cathode could improve the dissociation of oxygen molecule O_2 (ad) into atomic oxygen O_{ad}. Thus, the decreasing electronic and oxide ion conductivities from Ln = La to Gd in $Ln_{0.6}Sr_{0.4}CoO_{3-\delta}$ leads to a decrease in the oxygen exchange, transport speed of oxide ions, and charge transfer kinetics, which in turn results in a decrease in the electrochemical performance.

However, considering the long-term performance, $La_{0.6}Sr_{0.4}CoO_{3-\delta}$ may encounter a faster degradation in electrochemical performance compared to $Gd_{0.6}Sr_{0.4}CoO_{3-\delta}$ due to the larger difference in TEC (Table 3.2) between the $La_{0.6}Sr_{0.4}CoO_{3-\delta}$ cathode ($21.3 \times 10^{-6}\ ^{o}C^{-1}$) and the LSGM electrolyte ($12.2 \times 10^{-6}\ ^{o}C^{-1}$),[78] which could cause micro-cracks or delamination. Additionally, Qiu *et al.*[79] have reported that $Ln_{0.7}Sr_{0.3}Co_{0.2}Fe_{0.8}O_{3-\delta}$ with smaller lanthanide ions is less reactive with the YSZ electrolyte than $La_{0.7}Sr_{0.3}Co_{0.2}Fe_{0.8}O_{3-\delta}$. Therefore, the $Ln_{0.6}Sr_{0.4}CoO_{3-\delta}$ cathodes with an intermediate lanthanide ion such as Ln = Nd may be preferred, considering the trade-off between electrochemical performance and other parameters like TEC and reactivity.

Unlike in the $Ln_{0.6}Sr_{0.4}CoO_{3-\delta}$ system, the cathode over-potential in the $Ln_{1-x}Sr_xMnO_3$ system, however, does not seem to depend strongly on the lanthanide host cation.[67] This could be related to the differences in the formation of oxide ion vacancies and oxide ion conductivity. Wen *et al.*[80] have reported that the Mn^{4+} concentration increases proportionately with the Sr^{2+} concentration in the $Ln_{1-x}Sr_xMnO_3$ system and oxide ion vacancies do not exist even at high temperatures. Since the $Ln_{1-x}Sr_xMnO_3$ system[67] does not contain oxide ion vacancies, the change in lanthanide host cations may not significantly affect the oxygen exchange kinetics, and the oxygen reduction reaction could be rather limited by the three-phase boundary or surface diffusion, resulting in no strong correlation between the lanthanide host cations and the electrochemical performance.

3.4 CONCLUSIONS

The electrocatalytic activity of $Ln_{0.6}Sr_{0.4}CoO_{3-\delta}$ (Ln = La, Pr, Nd, Sm, and Gd) for oxygen reduction reaction in SOFC decreases from Ln = La to Gd. This trend could be understood to be due to the decreasing electrical and oxide ion conductivities caused, respectively, by an increasing bending of the O-Co-O bonds and a decreasing oxide ion vacancy concentration. However, going from Ln = La to Gd provides an important advantage of a decrease in TEC, which could be understood to be due to the decreasing ionicity of the Ln-O bonds, the suppression of the reduction of the Co^{4+} ions to Co^{3+} ions, and the decreasing amount of oxide ion

vacancies at elevated temperatures. These two opposing factors with decreasing Ln^{3+} size may make the $Ln_{0.6}Sr_{0.4}CoO_{3-\delta}$ cathodes with an intermediate lanthanide ion more attractive for practical cells. Additionally, the lack of a strong dependence of the catalytic activity of the analogous $Ln_{1-x}Sr_xMnO_3$ system on the Ln^{3+} ions unlike in the cobaltite system could be understood by considering the absence of oxide ion vacancies for Ln = La – Gd.

CHAPTER 4

CHARACTERIZATION OF $Nd_{1-x}Sr_xCoO_{3-\delta}$ ($0 \leq x \leq 0.5$) PEROVSKITE OXIDE CATHODE MATERIALS

4.1 INTRODUCTION

Although the $La_{1-x}Sr_xMnO_3$ perovskite oxide exhibits acceptable electrochemical activity for oxygen reduction at high temperatures with the zirconia electrolyte, its poor oxide ion conductivity prevents its application for intermediate temperature SOFC.[40, 81,82] These difficulties have created interest in the development of alternate cathode materials. $La_{1-x}Sr_xCoO_{3-\delta}$ perovskite oxides are appealing in this regard as they sustain a significant amount of oxygen vacancies δ due to the lower stability of the Co^{4+} oxidation state and exhibit high oxide ion conductivity. Accordingly, $La_{1-x}Sr_xCoO_{3-\delta}$[45,57,83] and other Sr-doped lanthanide cobaltites $Ln_{1-x}Sr_xCoO_{3-\delta}$ (Ln = Pr, Nd, Sm, and Gd)[59,62,63,84-86] have been investigated as cathode materials for intermediate temperature SOFC.

Chapter 3 presented a systematic investigation of the correlation of material properties and electrochemical performance to the lanthanide host cations in the $Ln_{0.6}Sr_{0.4}CoO_{3-\delta}$ (Ln = La, Pr, Nd, Sm, and Gd) cathode system. While $La_{0.6}Sr_{0.4}CoO_{3-\delta}$ exhibits high thermal expansion, replacement of La by other lanthanides Ln = Sm and Gd lowers the thermal expansion due to the decrease in the ionicity of the Ln-O bond. However, the replacement of the larger La by smaller Ln =

Sm and Gd lowers the electronic conductivity due to a bending of the Co-O-Co bonds from 180^{o} and a consequent decrease in the bandwidth and the covalency of the Co-O bonds. Considering a trade off between thermal expansion and electronic conductivity, the $Ln_{1-x}Sr_xCoO_{3-\delta}$ cathodes with an intermediate lanthanide ion are more attractive for practical use. The ionic size of Nd^{3+} is intermediate between those of La^{3+} and Sm^{3+} or Gd^{3+} and the ionicity of the Nd-O bond is intermediate between those of La-O and Sm-O or Gd-O bonds. With this respective, this chapter focuses on the crystal chemistry, thermal expansion, electrical conductivity, chemical compatibility, and electrochemical performance of $Nd_{1-x}Sr_xCoO_{3-\delta}$ ($0 \leq x \leq 0.5$), and a correlation of the electrochemical performance to the materials characteristics.

4.2 EXPERIMENTAL

4.2.1 Materials Synthesis

The $Nd_{1-x}Sr_xCoO_{3-\delta}$ compositions were synthesized by both conventional solid-state reactions and a coprecipitation method. With the solid-state reaction method, required amounts of Nd_2O_3, $SrCO_3$, and Co_3O_4 were fired in air first at 900 ^{o}C for 12 h, reground, pressed into pellets, and sintered at 1200 ^{o}C for 24 h. The sintering at 1200 ^{o}C was repeated for another 24 h after regrinding and repelletizing. With the coprecipitation method,[87] required amounts of Nd_2O_3, $SrCO_3$, and $Co(CH_3COO)_2{\cdot}4H_2O$ were first dissolved in dilute nitric acid and the metal ions were

then coprecipitated as carbonates and hydroxides at pH = 13 by adding a mixture of KOH and K_2CO_3. The coprecipiate was washed with deionized water, dried, fired at 500 ^oC for 5 h, ground, pressed into pellets, and sintered at 1200 ^oC for 24 h. The LSGM electrolyte disks and the NiO-$Ce_{0.9}Gd_{0.1}O_{1.95}$ (GDC) cermet (Ni:GDC = 70:30 vol %) anode powder were prepared by solid-state reaction and glycine-nitrate combustion method, respectively, as described in Chapter 2.

4.2.2 Fabrication of Single Cells

The $Nd_{1-x}Sr_xCoO_{3-\delta}$ ($0 \leq x \leq 0.5$) cathodes and NiO-GDC cermet anode were prepared by screen printing onto 1.0 mm thick LSGM electrolyte pellet, as described in Chapter 2, followed by firing for 3 h at 1000 ^oC for the cathode and 1200 ^oC for the anode.

4.2.3 Characterization

The samples were characterized by XRD, SEM, EDS, BET surface area, TGA, TMA, electrical conductivity, and electrochemical single cell measurements as described in Chapter 2. The reactivity tests between cathodes and the LSGM electrolyte were carried out at 1000 ^oC for 3h in air.

4.3 RESULTS AND DISCUSSION

4.3.1 Crystal Chemistry

The X-ray diffraction patterns of the $Nd_{1-x}Sr_xCoO_{3-\delta}$ ($0 \leq x \leq 0.5$) samples are shown in Figure 4.1. All the samples are single-phase materials and the patterns could be indexed on the basis of the orthorhombic perovskite ($GdFeO_3$ type) structure. The lattice parameters, BET surface area, and the average crystallite size of the samples are summarized in Table 4.1. The data indicate that the lattice volume increases with increasing Sr content, x. Although the substitution of Nd^{3+} by Sr^{2+} causes an oxidation of Co^{3+} to a smaller Co^{4+} and/or the formation of oxide ion vacancies, a significantly larger size of Sr^{2+} compared to that of Nd^{3+} (Table 4.2)[88] results in an overall increase in the cell volume with doping.

4.3.2 Defect Structure

The charge imbalance caused by a replacement of Nd^{3+} by Sr^{2+} could be accommodated either by an oxidation of Co^{3+} to Co^{4+} (electronic compensation) in $Nd^{3+}_{1-x}Sr^{2+}_{x}Co^{3+}_{1-x}Co^{4+}_{x}O_3$ or by the formation of oxide ion vacancies (ionic compensation) in $Nd^{3+}_{1-x}Sr^{2+}_{x}Co^{3+}O_{3-0.5x}$. The charge compensation mechanism and the consequent defect concentration depend on the doping level x, temperature, and oxygen partial pressure.

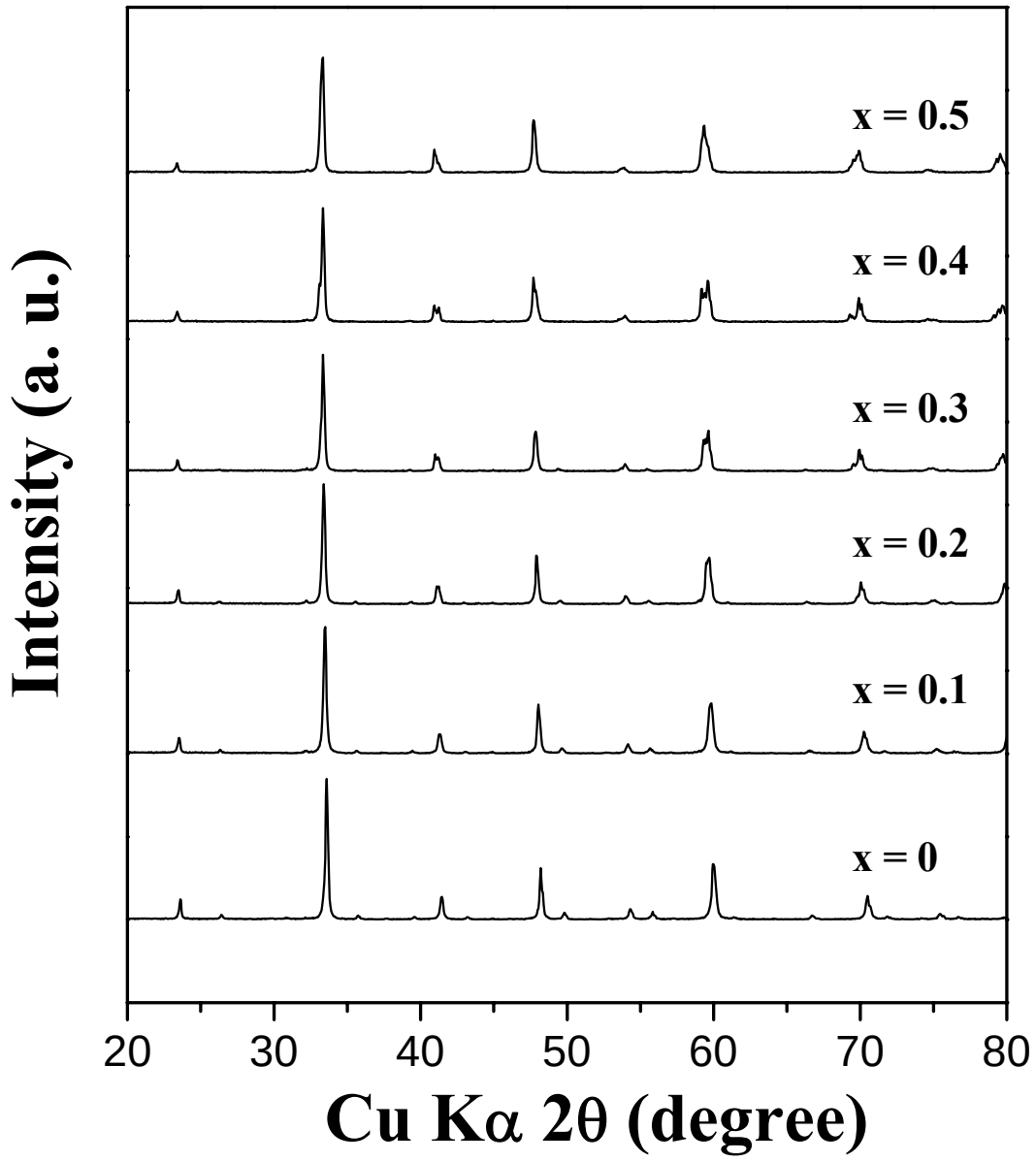

Figure 4.1 X-ray powder diffraction patterns of $Nd_{1-x}Sr_xCoO_{3-\delta}$ ($0 \leq x \leq 0.5$) sintered at 1200 ^{o}C for 24 h.

Table 4.1 Crystal chemistry data, BET surface area, and average crystallite size of $Nd_{1-x}Sr_xCoO_{3-\delta}$.

x	*a* (Å)	*b* (Å)	*c* (Å)	Lattice volume (Å^3)	BET surface area (m^2/g)	Average crystallite size [a] (Å)
0	5.3359(1)	5.3508(1)	7.5545(2)	215.7	4.1	570
0.1	5.3489(1)	5.3694(1)	7.5629(1)	217.2	5.0	590
0.2	5.3587(1)	5.3877(1)	7.5902(3)	219.1	5.5	570
0.3	5.3650(4)	5.4071(2)	7.5992(2)	220.4	4.7	530
0.4	5.3666(1)	5.4209(1)	7.5943(1)	220.9	4.5	440
0.5	5.3759(2)	5.4137(2)	7.6182(1)	221.7	5.3	580

[a] Average crystallite size was estimated with the line broadening of XRD peaks, and the error bar is ± 10 Å.

Table 4.2 Comparison of the ionic radii of the lanthanide and cobalt ions.[88]

Ion	Coordination number	Ionic radius (Å)
Nd^{3+}	12	1.27
Sr^{2+}	12	1.44
Co^{3+} (HS)[a]	6	0.61
Co^{3+} (LS)[a]	6	0.545
Co^{4+}	6	0.53
O^{2-}	6	1.40

[a] HS and LS refer, respectively, to high spin and low spin configurations.

Generally, the electronic compensation mechanism dominates at high oxygen partial pressures and low temperatures while the ionic compensation mechanism dominates at low oxygen partial pressures and high temperatures. Petrov *et al.*[57] have reported that the concentration of Co^{4+} in the $La_{1-x}Sr_xCoO_{3-\delta}$ system increases with x, reaches a maximum at $x \approx 0.4$, and then decreases. This suggests that the charge imbalance is accommodated primarily by the ionic mechanism at higher doping levels ($x > 0.4$) in $La_{1-x}Sr_xCoO_{3-\delta}$. The two mechanisms could be readily distinguished by determining the oxidation state of cobalt and the oxygen content by wet-chemical redox titrations. Unfortunately, the wet-chemical method could not be used with the $Nd_{1-x}Sr_xCoO_{3-\delta}$ ($x \leq 0.3$) system as the samples could not be dissolved in weakly acidic solutions.

Alternatively, thermogravimeric analysis (TGA) in air for the $Nd_{1-x}Sr_xCoO_{3-\delta}$ system was carried out and the data are shown in Figure 4.2. While the samples with $x \leq 0.3$ do not exhibit any detectable weight loss below 850 ^oC, the $x = 0.4$ and 0.5 samples exhibit some weight loss at lower temperatures ($T > 300$ ^oC), which corresponds to the loss of oxygen from the lattice. This observation suggests that the ionic compensation mechanism may be dominant for the samples with $x \geq 0.4$, while the electronic compensation mechanism may be dominant for $x \leq 0.3$ as in the case of $La_{1-x}Sr_xCoO_{3-\delta}$. This point will be used to rationalize the electrochemical performance data later.

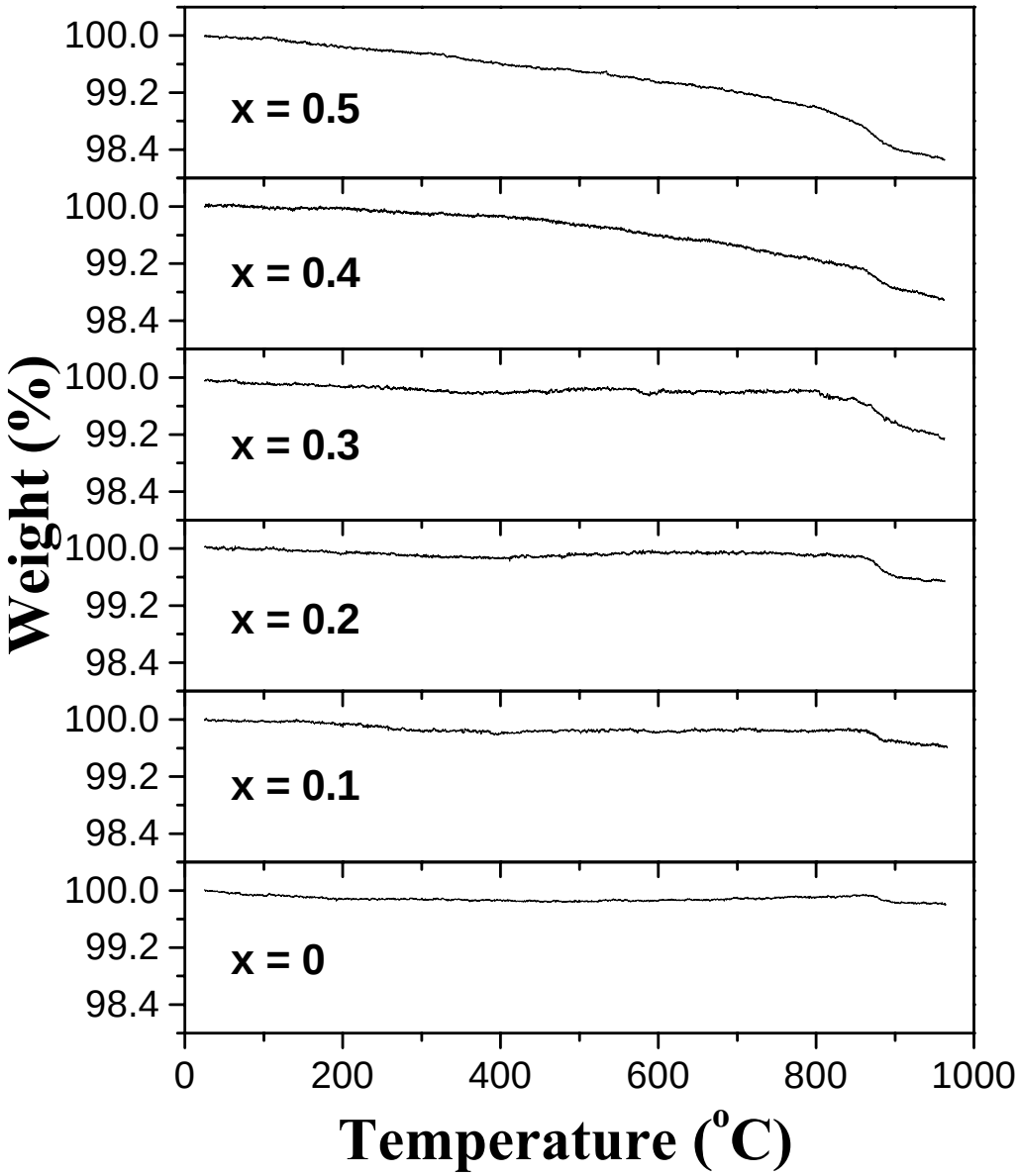

Figure 4.2 TGA plots of $Nd_{1-x}Sr_xCoO_{3-\delta}$ ($0 \leq x \leq 0.5$) recorded in air with a heating rate of 2 °C/min.

4.3.3 Thermal Expansion Behavior

The thermal expansion behaviors of $Nd_{1-x}Sr_xCoO_{3-\delta}$ at 50-700 ^oC in air are shown in Figure 4.3a. The thermal expansion behavior is related to temperature by a polynomial equation and it can be fitted as a fourth polynomial regression.[89] The average TEC values obtained by the fitting are plotted as a function of Sr content x in Figure 4.3b. The TEC decreases with increasing x, reaches a minimum value of 17.8 $\times 10^{-16}$ $^oC^{-1}$ at x = 0.3, and then increases. Similar trend has also been observed for the $Pr_{1-x}Sr_xCoO_{3-\delta}$ and $Sm_{1-x}Sr_xCoO_{3-\delta}$ systems,[59,63] and Kostogloudis *et al.*[59] attempted to explain this behavior with Grüneisen's law,[90]

$$\alpha_V = \frac{\gamma C_V}{VB} \tag{4.1}$$

where α_V is the bulk TEC, γ is the Grüneisen's constant, C_v is the heat capacity at constant volume, V is cell volume, and B is the bulk modulus. Since the cell volume increases with Sr substitution, it causes a decrease in TEC with x.

As discussed in Chapter 3, consideration of the changes in the spin states of the cobalt ions and the consequent changes in the ionic size with temperature will be a useful way to explain the TECs. It has been reported[91-93] that Co^{3+} ions in $LnCoO_3$ (Ln: La, Nd, and Gd) exist in the diamagnetic low spin Co^{III} state ($t_{2g}^6 e_g^0$) at very low temperatures and transform to paramagnetic high spin Co^{3+} state ($t_{2g}^4 e_g^2$) or an intermediate spin Co^{iii} state ($t_{2g}^5 e_g^1$) at higher temperatures.

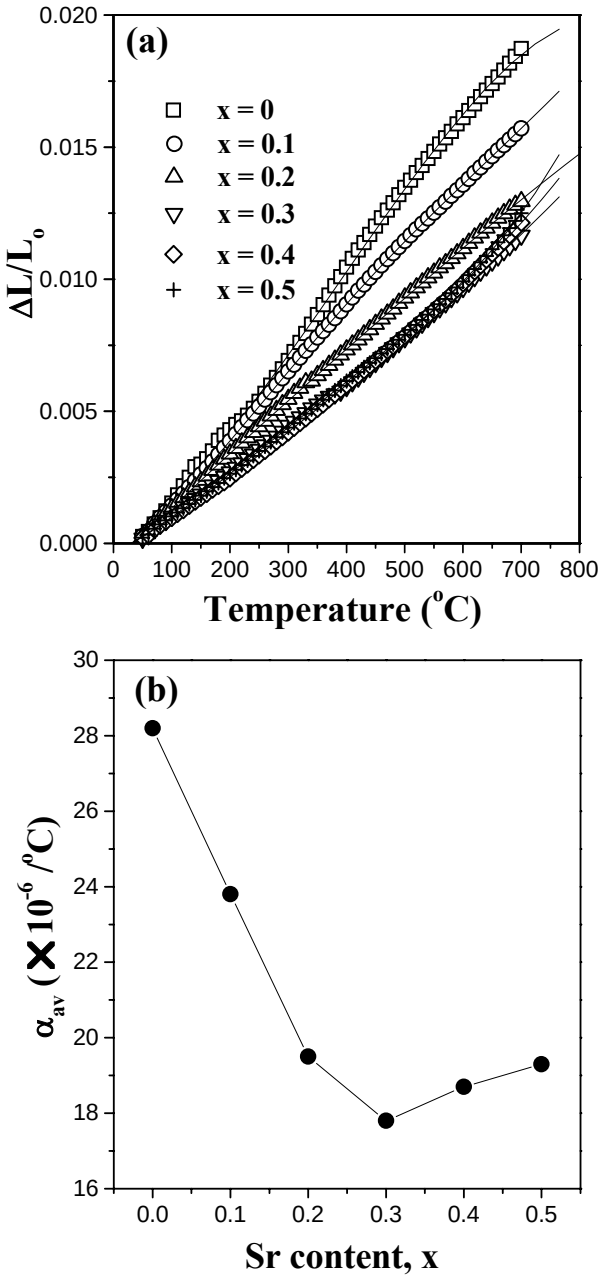

Figure 4.3 Thermal expansion behaviors of $Nd_{1-x}Sr_xCoO_{3-\delta}$ ($0 \le x \le 0.5$) in air: (a) thermal expansion ($\Delta L/L_o$) curves as a function of temperature and (b) variation of average linear thermal expansion coefficients (α_{av}) with Sr content x in the temperature range 50-700 ^oC.

Considering the ionic radii values in Table 4.2, the large TEC value for the undoped $NdCoO_3$ could be understood to be due to the transition of the smaller low spin Co^{III} ions to the larger high spin Co^{3+} or intermediate spin Co^{iii} ions with increasing temperature. A substitution of Sr^{2+} for Nd^{3+} oxidizes Co^{3+} to Co^{4+}, which exists in the low spin Co^{IV} state ($t_{2g}^5 e_g^0$).[93] A decrease in the Co^{3+} content and the consequent decrease in the amount of low spin to high spin transition causes a decrease in the TEC value with increasing x for $0 \leq x \leq 0.3$. However, at higher doping levels with $x \geq 0.4$, charge compensation by ionic mechanism may dominate as discussed earlier, resulting in the formation of oxide ion vacancies and a suppression of the oxidation of Co^{3+} to low spin Co^{4+} with Sr substitution. Furthermore, the samples with $x \geq 0.4$ tend to lose oxygen from the lattice for $T > 300$ ^oC as indicated by the TGA data (Figure 4.2), resulting in a reduction of the smaller Co^{4+} to larger Co^{3+} with temperature and a consequent increase in TEC. The presence of oxide ion vacancies could also decrease the electrostatic attractive forces[94,95] and increase the TEC.

4.3.4 Electrical Conductivity

The temperature dependence of the electrical conductivity of $Nd_{1-x}Sr_xCoO_{3-\delta}$ is shown in Figure 4.4a. The variations of conductivity with Sr content x at various temperatures are shown in Figure 4.4b. The data in Figure 4.4 are in general agreement with the previous reports,[85,86] but no systematic explanation was available before. At a given temperature, the conductivity value increases with increasing x due

to an increasing Co^{4+} content and the charge carrier concentration. The conductivity increases with increasing temperature for $x < 0.3$, implying a small polaron semi-conducting behavior, but decreases with increasing temperature for $x \geq 0.3$, implying a metallic-conducting behavior. The $Nd_{1-x}Sr_xCoO_{3-\delta}$ system thus exhibits a semiconductor to metal transition around $x = 0.3$. The faster decrease in conductivity at higher temperatures for samples with $x \geq 0.3$ in Figure 4.4a could be due to the loss of oxygen from the lattice at higher temperatures as indicated by the TGA data (Figure 4.2) and the consequent decrease in the Co^{4+} content and carrier concentration.

For the compositions with semiconducting behavior, the temperature dependence of the conductivity can be described by the small polaron hopping mechanism as

$$\sigma = \frac{A}{T}\exp\left(-\frac{E_a}{kT}\right) \tag{4.2}$$

where A is the pre-exponential factor, T is the temperature, k is the Boltzmann constant, and E_a is the activation energy for the hopping of the small polarons. The activation energies obtained from the Arrhenius plots of $\ln(\sigma T)$ vs. $1/T$ are given in Table 4.3.

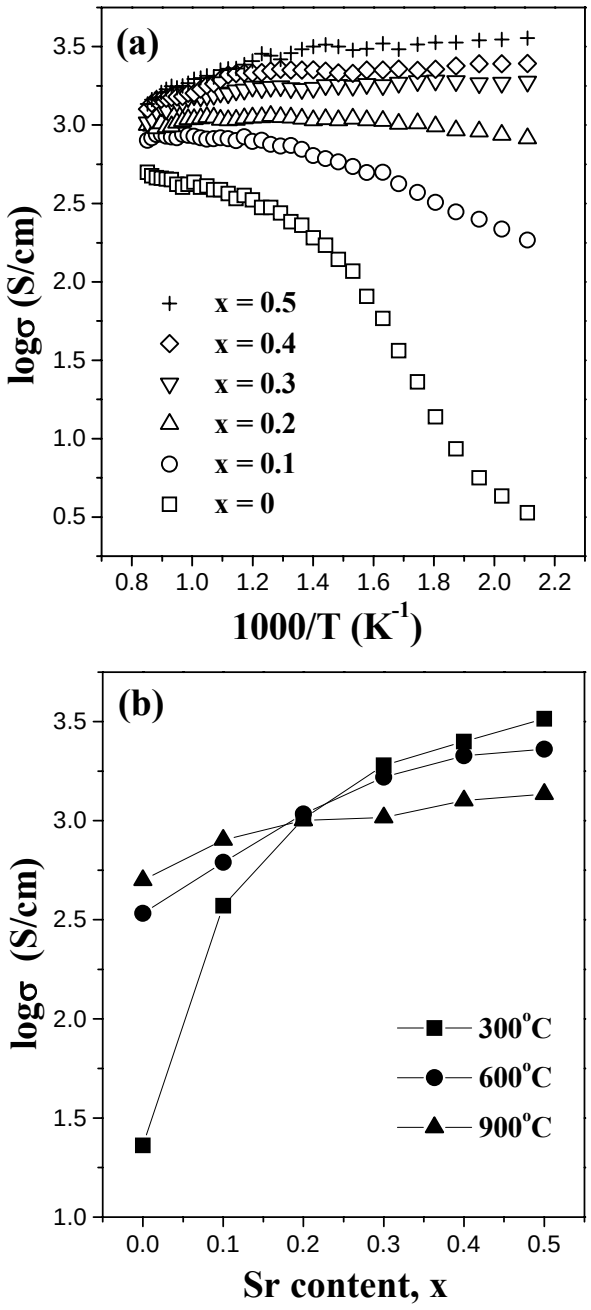

Figure 4.4 Variations of electrical conductivity measured in air of $Nd_{1-x}Sr_xCoO_{3-\delta}$ ($0 \leq x \leq 0.5$) (a) with temperature for various values of x and (b) with Sr content x at various temperatures.

Table 4.3 Activation energy values for the electrical conduction of $Nd_{1-x}Sr_xCoO_{3-\delta}$.

x	Temperature range (^oC)	E_a (eV)
0	200-250	0.32
	250-400	0.69
	400-800	0.22
0.1	200-800	0.17
0.2	200-800	0.07

The activation energy E_a decreases with increasing x. The changes in E_a with temperature for $NdCoO_3$ is attributed to the spin state transitions, and the data are in agreement with that reported by Rajoria *et al.*[92] The changes in the E_a values of $NdCoO_3$ with temperature is also in accordance with the slope change observed in the thermal expansion curve.

The activation energy for the hopping of small polaron (*e.g.* hole) is given as[96]

$$E_a = \frac{E_p}{2} - W \tag{4.3}$$

where E_p is the polaron binding energy and W is bandwidth. The decrease in the activation energy with x in $Nd_{1-x}Sr_xCoO_{3-\delta}$ implies a reduction in the polaron binding energy or an increase in the bandwidth, which could be understood by considering the changes in the structural parameters with doping. As discussed in Chapter 3, the crystal symmetry of the ABO_3 perovskite structure can be described by the

geometrical Goldschmidt tolerance factor, *t*. The undoped $NdCoO_3$ has a $t = 0.940$ at room temperature, which implies that the Nd-O bonds are under tension and the Co-O bonds are under compression. The compressive stress results in a bending of the O-Co-O bonds and a bond angle of $< 180^o$. Both the bandwidth and the magnetic exchange interaction are closely related to $\cos\theta$,[97] where θ is the deviation of the bond angle from the ideal value of 180^o. The substitution of a larger Sr^{2+} for Nd^{3+} not only relieves the tensile stress in the (Nd,Sr)-O bond but also relieves the compressive stress in the Co-O bond due to an oxidation of the larger Co^{3+} to smaller Co^{4+} ions. This leads to an increase in *t* and the O-Co-O bond angle toward 180^o, resulting in an increase in the overlap between the $Co^{3+/4+}$:3d and O^{2-}:2p orbitals and the bandwidth.[98] Moreover, the straightening of the O-Co-O bonds relieves the deep localization of charge carriers and thereby decreases E_p. Thus the increase in bandwidth and the decrease in polaron binding energy lead to a decrease in the activation energy with increasing doping x.

The semiconductor to metal transition in $Nd_{1-x}Sr_xCoO_{3-\delta}$ with doping could also be understood by considering the changes in the structural parameters. The $LnNiO_3$ (Ln = Pr, Nd, Sm, and Eu) perovskites exhibit a semiconductor to metal transition at a transition temperature T_t, and the value of T_t increases with decreasing size of Ln^{3+}.[99] Torrance *et al.*[99] reported that the increase in T_t with the decreasing size of Ln^{3+} is due to a decrease in the tolerance factor *t* and the consequent increase in the bending of the O-Ni-O bonds. As the temperature increases, *t* increases due to a

larger thermal expansion of the Ln-O bonds compared to the Ni-O bonds and the O-Ni-O bond angle increases toward 180^{o}, resulting in an increasing bandwidth. At a critical bandwidth, the charge transfer gap between the $Ni^{3+/4+}$:3d and the O^{2-}:2p bands vanishes, leading to metallic behavior. Similar arguments of an increase in the tolerance factor with increasing x in $Nd_{1-x}Sr_xCoO_{3-\delta}$ together with the increasing covalency of the Co-O bonds with an oxidation of Co^{3+} to Co^{4+} and the consequent increase in the bandwidth and a vanishing of the charge transfer gap could be envisioned to cause a semiconductor to metal transition with increasing x in $Nd_{1-x}Sr_xCoO_{3-\delta}$.

4.3.5 Electrochemical Performance

The BET surface area and the average crystallite size do not vary significantly with x in $Nd_{1-x}Sr_xCoO_{3-\delta}$ (Table 4.1), and therefore influence of the geometrical morphology on electrochemical performance could be considered negligible. Figure 4.5 compares the variations of the I-V curves, power density, and the over-potential with current density at 800 ^{o}C for the various $Nd_{1-x}Sr_xCoO_{3-\delta}$ cathode compositions. The open-circuit voltage at 800 ^{o}C was typically 1.07 to 1.09 V, which is close to the theoretical value. The power density increases with increasing Sr content x for $0 \leq x \leq 0.4$, reaches a maximum at x = 0.4, and then decreases for x = 0.5. The over-potential decreases with x initially, reaches a minimum at x = 0.4, and then increases similar to the trend in the power density.

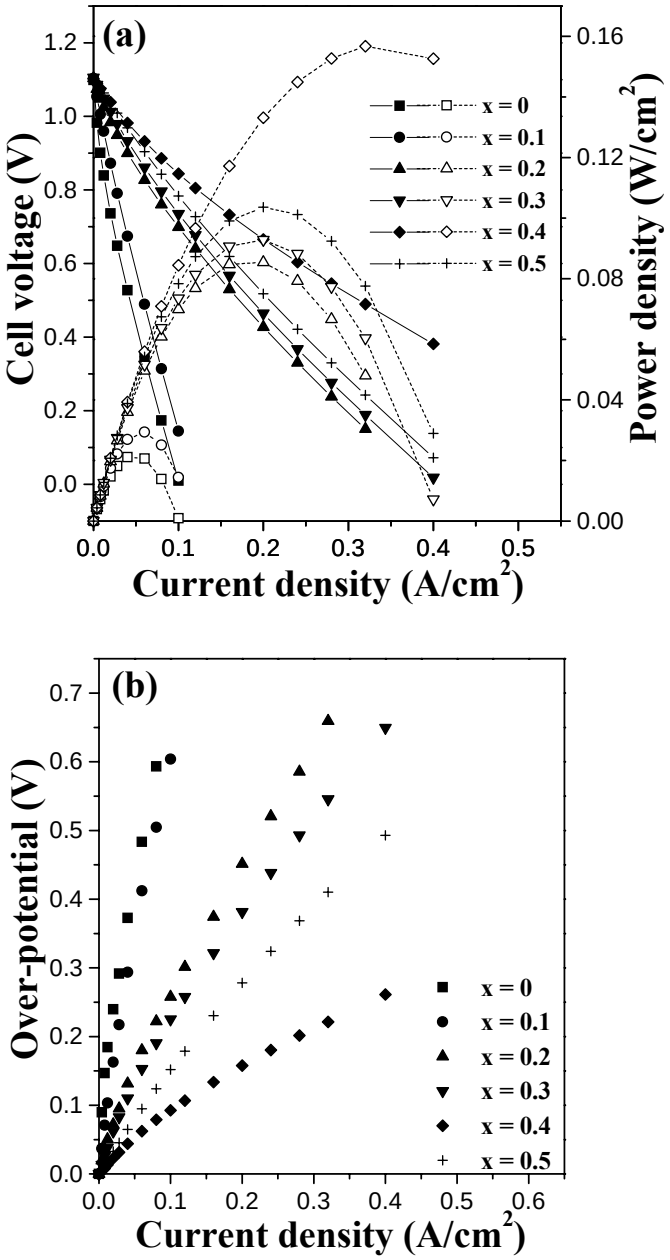

Figure 4.5 Electrochemical performance data of $Nd_{1-x}Sr_xCoO_{3-\delta}$/LSGM/Ni-GDC single cells at 800 ^oC: Variations of (a) the I-V curve (closed symbols) and power density (open symbols) and (b) cathode over-potential.

The lower power density and higher over-potential for the x = 0 and 0.1 samples could be attributed to the lower electrical conductivity as well as surface cracks, which increase the resistance. Figure 4.6 compares the surface structure of the $Nd_{1-x}Sr_xCoO_{3-\delta}$ cathodes after the single cell test. While the x = 0 and 0.1 samples develop cracks due to the larger thermal expansion coefficient, the samples with $x \geq 0.2$ do not experience any crack problems.

The main reaction at the cathode is the oxygen reduction reaction given below:

$$\frac{1}{2}O_2\,(gas) + 2e^-\,(cathode) \rightarrow O^{2-}\,(electrolyte) \qquad (4.4)$$

It is usually assumed that there are two possible paths for the cathode reaction. One is the surface path and the other is the bulk path. In the surface path, oxygen is adsorbed and partly reduced on the surface of the cathode, which then diffuses along the cathode surface to the three phase boundary (TPB) constituted by cathode/electrolyte/gas where it becomes fully reduced and completes the ionic transfer into the electrolyte. The surface path for the incorporation of oxygen into the electrolyte is usually considered as a favorable mechanism. Under electrical load, the oxide ion would then diffuse through the cathode and get incorporated into the electrolyte at the cathode/electrolyte interface (bulk path). Considering the predominantly electronic charge compensation mechanism at the low doping level as

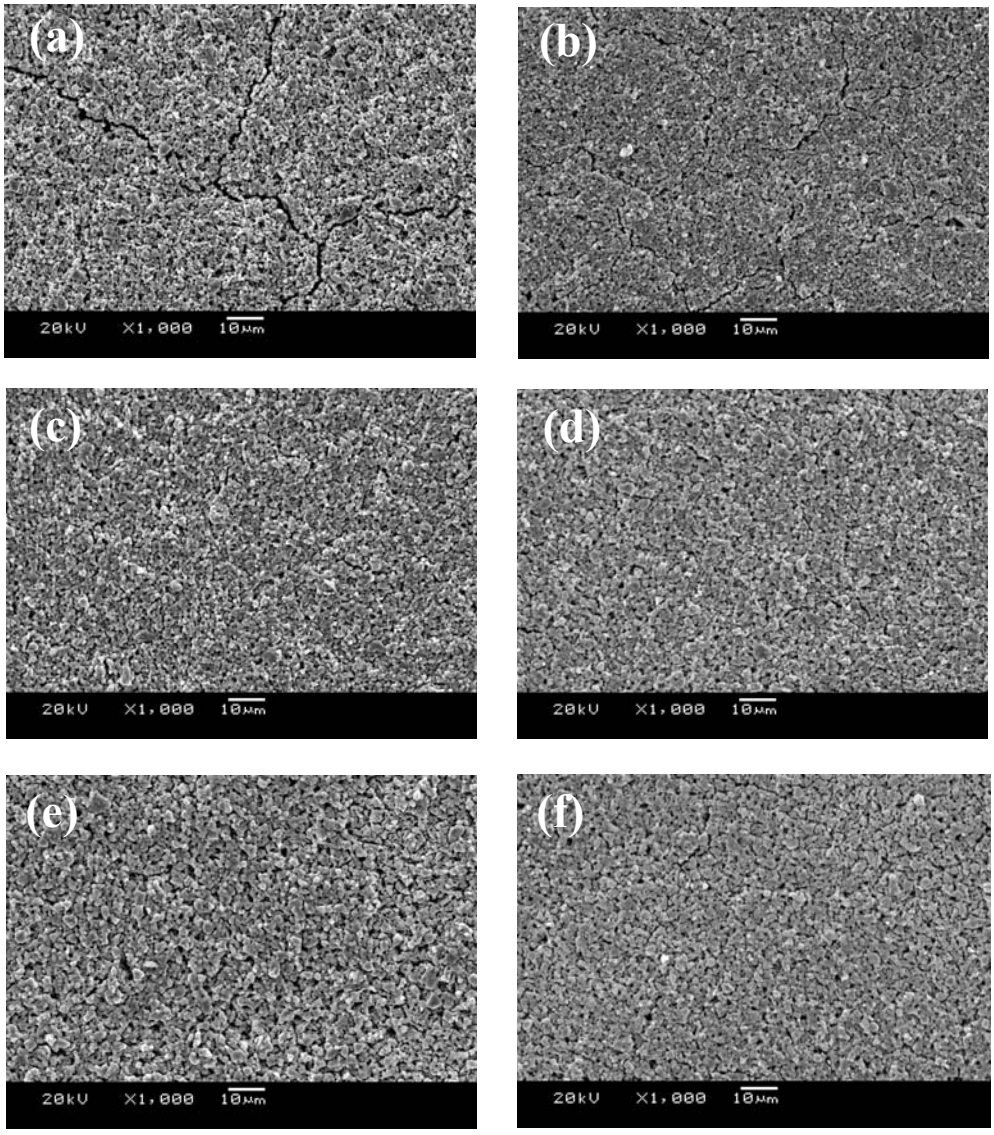

Figure 4.6 SEM micrographs showing the surface structure of the $Nd_{1-x}Sr_xCoO_{3-\delta}$ cathodes after testing the $Nd_{1-x}Sr_xCoO_{3-\delta}$/LSGM/Ni-GDC single cells at 800 ^oC: (a) x = 0, (b) x = 0.1, (c) x = 0.2, (d), x = 0.3, (e) x = 0.4, and (f) x = 0.5.

discussed earlier, the bulk path may be unfavorable for the samples with $0 \leq x \leq 0.3$ due to the rather low concentration of oxide ion vacancies. On the other hand, the bulk path may become favorable for $x \geq 0.4$ due to the presence of significant amount of oxide ion vacancies at higher temperatures as indicated by the TGA data (Figure 4.2), leading to good electrochemical performance.

However, the electrochemical performance decreases on going from $x = 0.4$ to $x = 0.5$. Both the variations in the anode/electrolyte over-potential arising from the nonuniformity of the anode or electrolyte as well as cathode over-potential could contribute to the observed decrease in the electrochemical performance. Table 4.4 compares the anode/electrolyte over-potential and cathode over-potential values for $0.3 \leq x \leq 0.5$. As seen in Table 4.4, the change in the anode/electrolyte over-potential on going from $x = 0.4$ to 0.5 is much smaller compared to that in the cathode over-potential. Therefore, it is clear that cathode over-potential is the predominant factor in influencing the power density.

Table 4.4 Electrochemical performance data of $Nd_{1-x}Sr_xCoO_{3-\delta}$/LSGM/GDC-Ni single cells at 800 ^oC (open circuit voltage: 1.09 V).

x	Current density (A/cm^2)	Cell voltage (V)	Power density (W/cm^2)	Cathode over-potential (V)	Electrolyte/anode over-potential (V)
0.3	0.28	0.28	0.08	0.49	0.32
0.4	0.28	0.55	0.15	0.20	0.34
0.5	0.28	0.33	0.09	0.37	0.39

In order to understand the origin of the increase in cathode over-potential on going from x = 0.4 to 0.5, the interfacial reaction between the LSGM electrolyte and the $Nd_{0.5}Sr_{0.5}CoO_{3-\delta}$ cathode has to be considered. Figure 4.7 compares the X-ray powder diffraction patterns of $Nd_{1-x}Sr_xCoO_{3-\delta}$ and LSGM mixtures for $0.3 \leq x \leq 0.5$ after heating at 1000 ^oC for 3 h. While no new reaction product is observed for the x = 0.3 and 0.4 compositions, the insulating $LaSrGa_3O_7$ reaction product is found for the x = 0.5 composition. This observation is also supported by the SEM/EDS analysis. SEM micrographs of the cross sections of the $Nd_{0.6}Sr_{0.4}CoO_{3-\delta}$/LSGM and $Nd_{0.5}Sr_{0.5}CoO_{3-\delta}$/LSGM interfaces are shown in Figures 4.8a and 4.8b and the corresponding EDS analysis data are shown in Figures 4.8c and 4.8d. While no significant interdiffusion at the interface between $Nd_{0.6}Sr_{0.4}CoO_{3-\delta}$ and LSGM is seen, high Co diffusion into the electrolyte and fluctuations in the La and Ga concentrations are seen at the interface between $Nd_{0.5}Sr_{0.5}CoO_{3-\delta}$ and LSGM. Interdiffuaion of Co and the formation of $LaSrGa_3O_7$ were also seen by Huang *et al.*[100] on heating $La_{0.5}Sr_{0.5}CoO_{3-\delta}$ and LSGM at 1050 ^oC for 2 h. It is clear that the interfacial reaction between the electrolyte and the cathode leads to a decrease in electrochemical performance on going from x = 0.4 to x = 0.5.

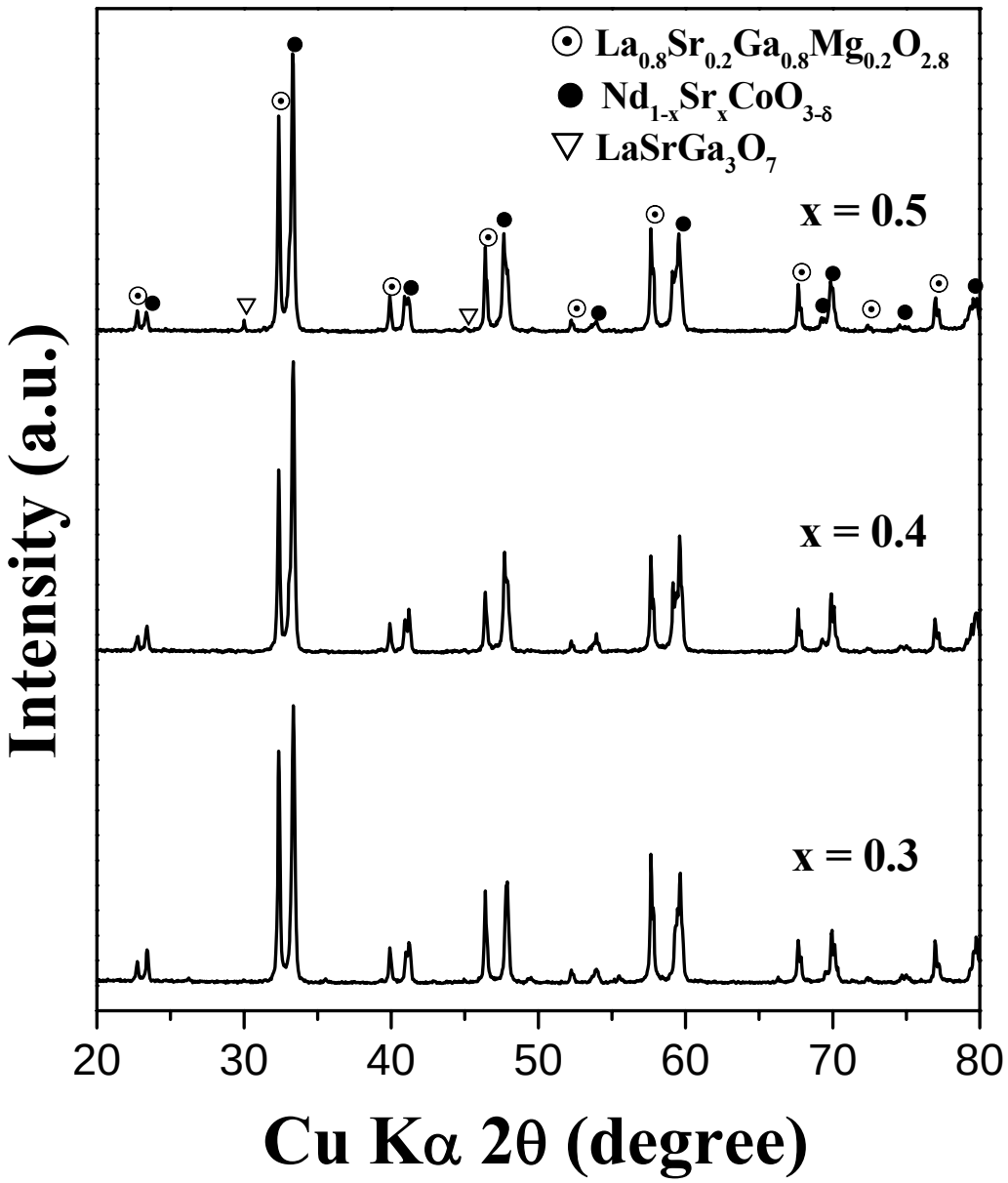

Figure 4.7 X-ray powder diffraction patterns recorded after heating the $Nd_{1-x}Sr_xCoO_{3-\delta}$ (x = 0.3, 0.4, and 0.5) cathode and the LSGM electrolyte powders at 1000 ^oC for 3 h.

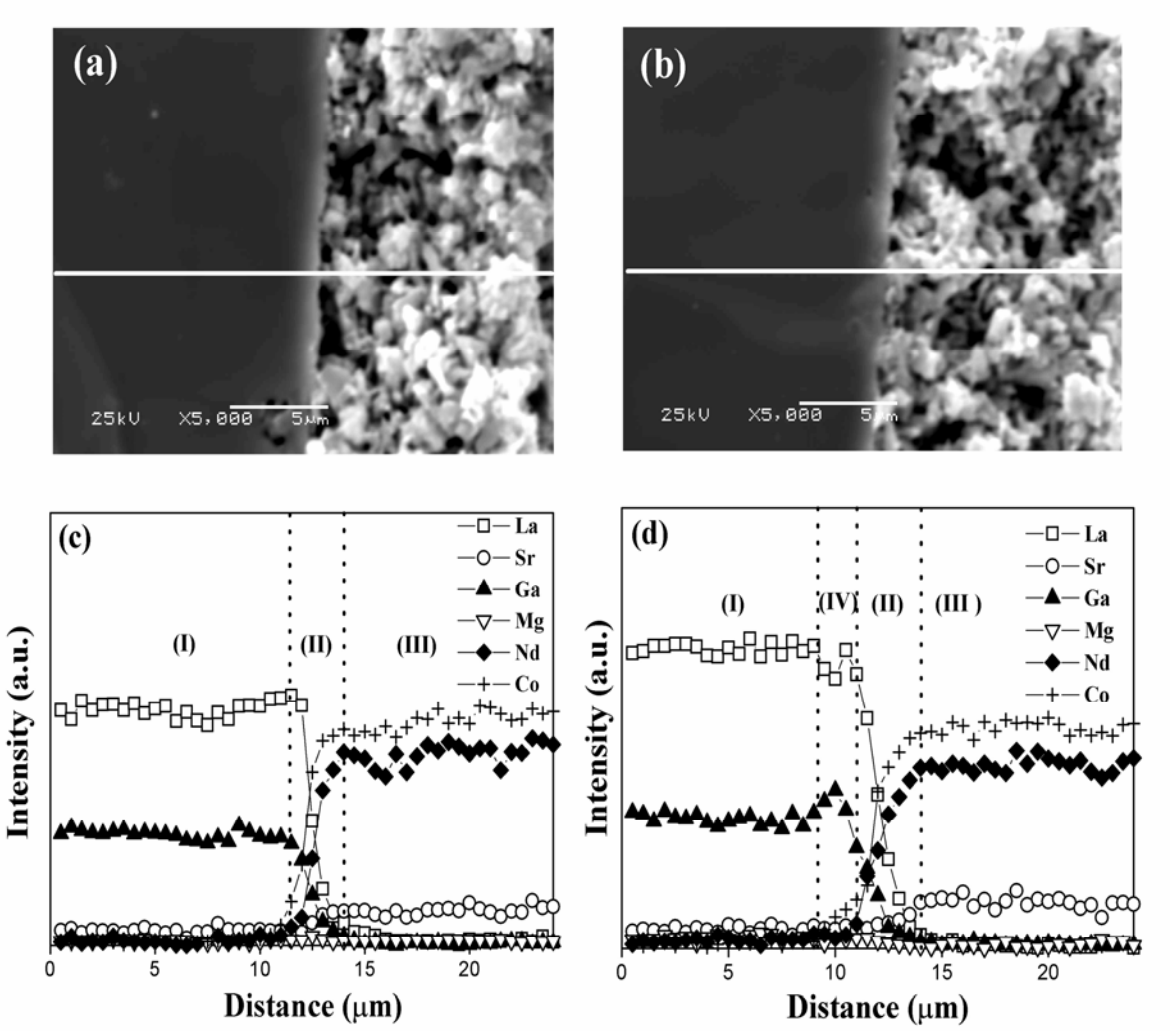

Figure 4.8 SEM micrographs of (a) the $Nd_{0.6}Sr_{0.4}CoO_{3-\delta}$/LSGM interface and (b) the $Nd_{0.5}Sr_{0.5}CoO_{3-\delta}$/LSGM interface. EDS analysis across (c) the $Nd_{0.6}Sr_{0.4}CoO_{3-\delta}$/LSGM interface and (d) the $Nd_{0.5}Sr_{0.5}CoO_{3-\delta}$/LSGM interface after single cell test. Region (I): electrolyte zone. Region (II): interdiffusion zone. Region (III): electrode zone. Region (IV): new reaction product ($LaSrGa_3O_7$) formation zone.

In order to study the effect of synthesis procedure on the electrochemical performance, the performance of the x = 0.4 composition that was prepared by a standard solid-state reaction and a coprecipitation method has been also compared. Figure 4.9 compares the I-V curves, power density, and the over-potential of the $Nd_{0.6}Sr_{0.4}CoO_{3-\delta}$ cathode obtained by the two synthesis procedures. The $Nd_{0.6}Sr_{0.4}CoO_{3-\delta}$ cathode obtained by the coprecipitation method exhibits a lower over-potential and a higher maximum power density value of 0.24 W/cm^2 at 800 ^oC than that prepared by the solid-state reaction. The microstructures of the $Nd_{0.6}Sr_{0.4}CoO_{3-\delta}$ cathodes prepared by the two procedures are compared in Figure 4.10. While the cathode obtained by solid-state reaction method shows only point contacts between particles and poor adhesion between the cathode and electrolyte, the cathode obtained by the coprecipitation method shows area contact between particles and good adhesion between the cathode and electrolyte, which lead to low contact and charge transfer resistances and better electrochemical performance.

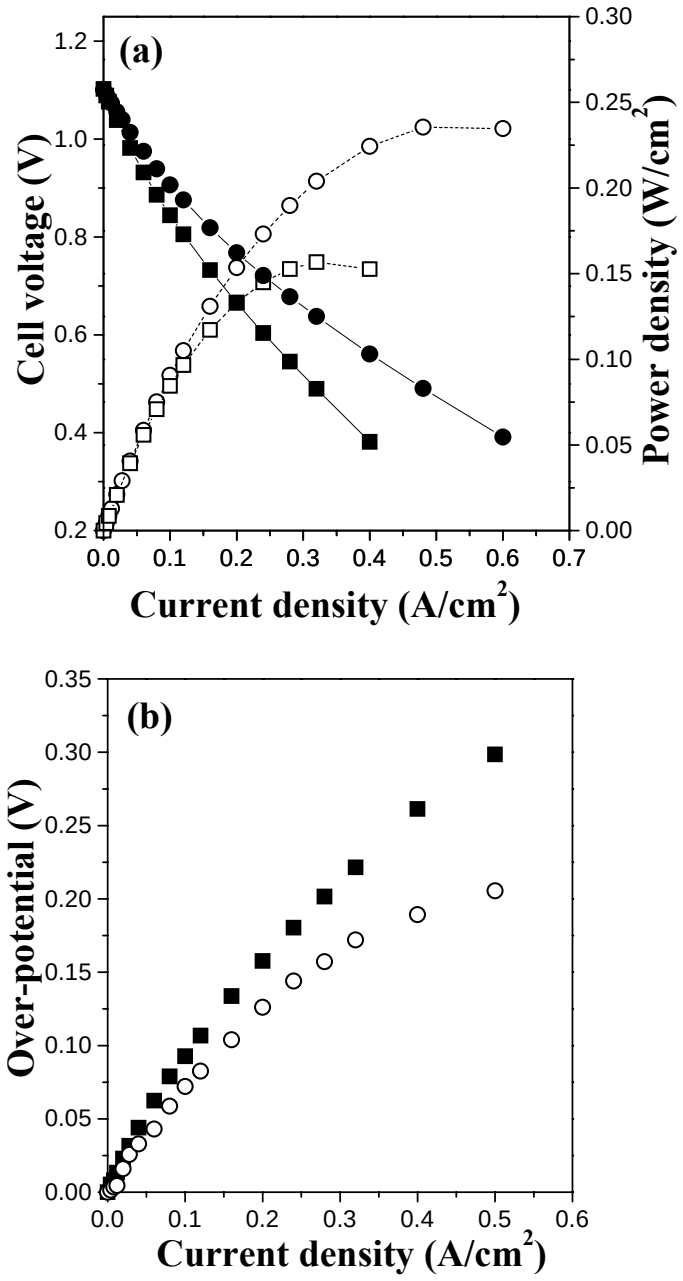

Figure 4.9 Comparison of (a) the I-V curves (closed symbols) and power densities (open symbols) and (b) cathode over-potential for the $Nd_{0.6}Sr_{0.4}CoO_{3-\delta}$ cathodes that were synthesized by solid-state reaction (squares) and coprecipitation method (circles).

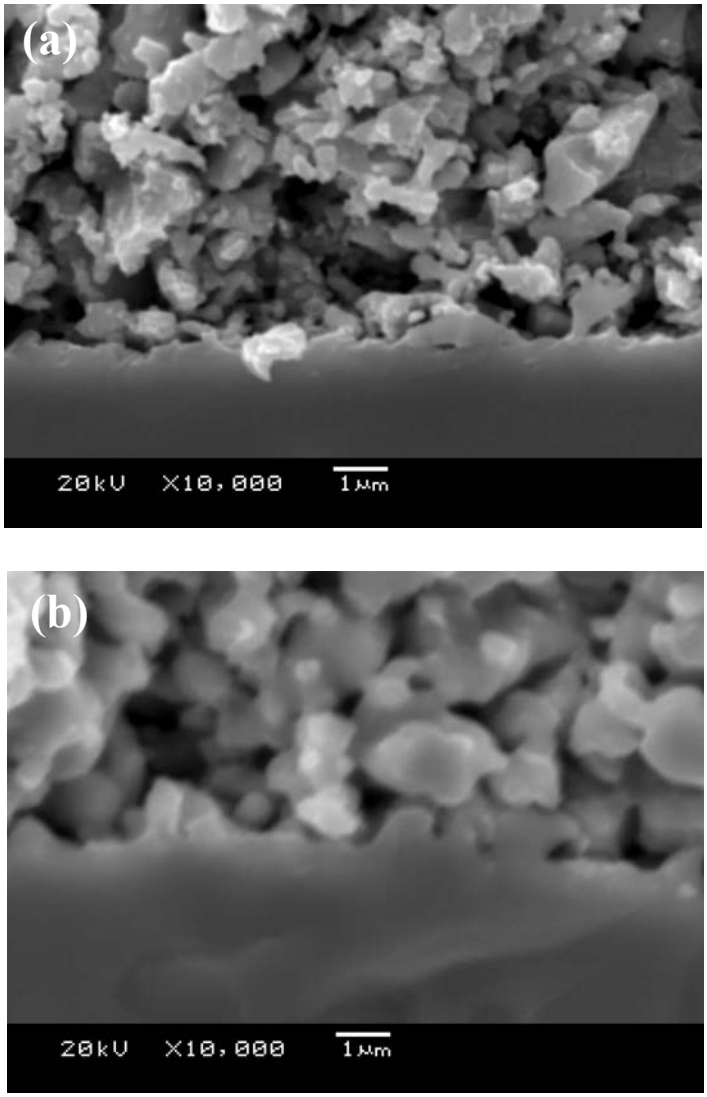

Figure 4.10 SEM micrographs of $Nd_{0.6}Sr_{0.4}CoO_{3-\delta}$ cathodes that were synthesized by (a) solid-state reaction and (b) coprecipitation method. The micrographs were recorded after the single cell test at 800 ^{o}C.

4.4 CONCLUSIONS

$Nd_{1-x}Sr_xCoO_{3-\delta}$ ($0 \leq x \leq 0.5$) perovskite oxides have been evaluated as cathode materials for intermediate temperature SOFC. The thermal expansion coefficient decreases with x initially and reaches a minimum around x = 0.3 due to the suppression of spin state transitions associated with Co^{3+}. The electrical conductivity increases with increasing Sr content and the system exhibits a semiconductor to metal transition around x = 0.3. While the sample with $x \leq 0.3$ do not lose much oxygen on heating, the x = 0.4 and 0.5 samples lose oxygen at T > 300 ^oC, suggesting good mixed electronic-ionic conductivity at high temperatures. The x = 0.4 composition with good mixed conduction exhibits the best electrochemical performance with a maximum power density value of 0.24 W/cm^2 at 800 ^oC in single cells fabricated with 1.0 mm thick LSGM electrolyte and Ni-$Ce_{0.9}Gd_{0.1}O_{1.95}$ (GDC) cermet anode. Although the x = 0.5 composition would be expected to show similar or better performance than the x = 0.4 sample, it suffers from interfacial reaction with the electrolyte. With an ionic size and electronegativity of Nd^{3+} intermediate between those of La^{3+} and Gd^{3+}, the $Nd_{1-x}Sr_xCoO_{3-\delta}$ system offers significant advantages with a combination of low thermal expansion, high electrical conductivity, and low reactivity compared to the other $Ln_{1-x}Sr_xCoO_{3-\delta}$ systems.

CHAPTER 5

CHARACTERIZATION OF $Nd_{0.6}Sr_{0.4}Co_{1-y}M_yO_{3-\delta}$ (M = Fe AND Mn) PEROVSKITE OXIDE CATHODE MATERIALS

5.1 INTRODUCTION

Although the Co containing perovskite oxides cathodes show good catalytic activity toward oxygen reduction reaction,[45,57,83] oxides with significant amounts of Sr or Co exhibit high thermal expansion due to the low spin to high spin transition associated with the Co^{3+} ions and chemical reactivity with the electrolyte.[75] These difficulties could be minimized by an appropriate choice of lanthanide ion and optimum Sr content in $Ln_{1-x}Sr_xCoO_{3-\delta}$ perovskites. In Chapters 4 and 5, the $Nd_{1-x}Sr_xCoO_{3-\delta}$ system among the $Ln_{1-x}Sr_xCoO_{3-\delta}$ (Ln = La, Pr, Nd, Sm, Gd) perovskite oxides was recognized to offer a tradeoff between thermal expansion and electronic conductivity, and the x = 0.4 composition in the system $Nd_{1-x}Sr_xCoO_{3-\delta}$ was found to show the highest catalytic activity without encountering any interfacial reaction with the LSGM electrolyte. Although the catalytic activity observed at the intermediate temperatures is satisfactory, the TEC of $Nd_{0.6}Sr_{0.4}CoO_{3-\delta}$ is still high. With an aim to lower the TEC, this chapter focuses on the substitution of Fe or Mn for Co and a characterization of the $Nd_{0.6}Sr_{0.4}Co_{1-y}M_yO_{3-\delta}$ (M = Fe and Mn) cathodes. The effect of Fe or Mn content on the crystal chemistry, thermal expansion, electrical conductivity, and electrochemical performance in single cell SOFC is presented.

5.2 EXPERIMENTAL

5.2.1 Materials Synthesis

The $Nd_{0.6}Sr_{0.4}Co_{1-y}M_yO_{3-\delta}$ (M = Fe and Mn) cathode materials were synthesized by firing required amounts of Nd_2O_3, $SrCO_3$, Co_3O_4, and Fe_2O_3 or Mn_2O_3 in air at 900 ^oC for 12 h, followed by regrinding, pressing into pellets, and sintering for 24 h at 1200 ^oC for the Fe-doped system and 1300 ^oC for the Mn-doped system. The sintering was repeated for another 24 h after regrinding and repelletizing in order to improve the product homogeneity. The LSGM electrolyte disks and the NiO-$Ce_{0.9}Gd_{0.1}O_{1.95}$ (GDC) cermet (Ni:GDC = 70:30 vol %) anode powder were prepared by solid-state reaction and glycine-nitrate combustion method, respectively, as described in Chapter 2.

5.2.2 Fabrication of Single Cells

The $Nd_{0.6}Sr_{0.4}Co_{1-y}M_yO_{3-\delta}$ (M = Fe and Mn) cathode and NiO-GDC cermet anode were prepared by screen printing onto 0.7-0.8 mm thick LSGM electrolyte pellet, as described in Chapter 2, followed by firing for 3 h at 1000 ^oC for the Fe-doped system, 1100 ^oC for the Mn-doped system, and 1200 ^oC for the anode.

5.2.3 Characterization

The samples prepared were characterized by XRD, BET surface area, TGA, TMA, electrical conductivity, and single cell measurement as described in Chapter 2. The reactivity tests between cathodes and the LSGM electrolyte were carried out for 3 h at 1000 ^{o}C in air for the Fe-doped system and 1100 ^{o}C for the Mn-doped system.

5.3 RESULTS AND DISCUSSION

5.3.1 Crystal Chemistry and Thermogravimetric Analysis

X-ray diffraction patterns of the $Nd_{0.6}Sr_{0.4}Co_{1-y}M_yO_{3-\delta}$ (M = Fe and Mn) samples are shown in Figures 5.1 and 5.2. All samples were found to be single phase and the X-ray diffraction patterns could be indexed with the orthorhombic $GdFeO_3$ type perovskite structure for $0 \leq y \leq 0.5$. The lattice parameters, BET surface area, and average crystallite size of the samples are summarized in Table 5.1. The lattice parameters and the lattice volume increase with increasing y due to the replacement of the smaller Co^{3+}/Co^{4+} (average ionic radius, r = 0.538 Å) ions by the larger Fe^{3+}/Fe^{4+} (r = 0.615 Å) or Mn^{3+}/Mn^{4+} (r = 0.589 Å) ions.

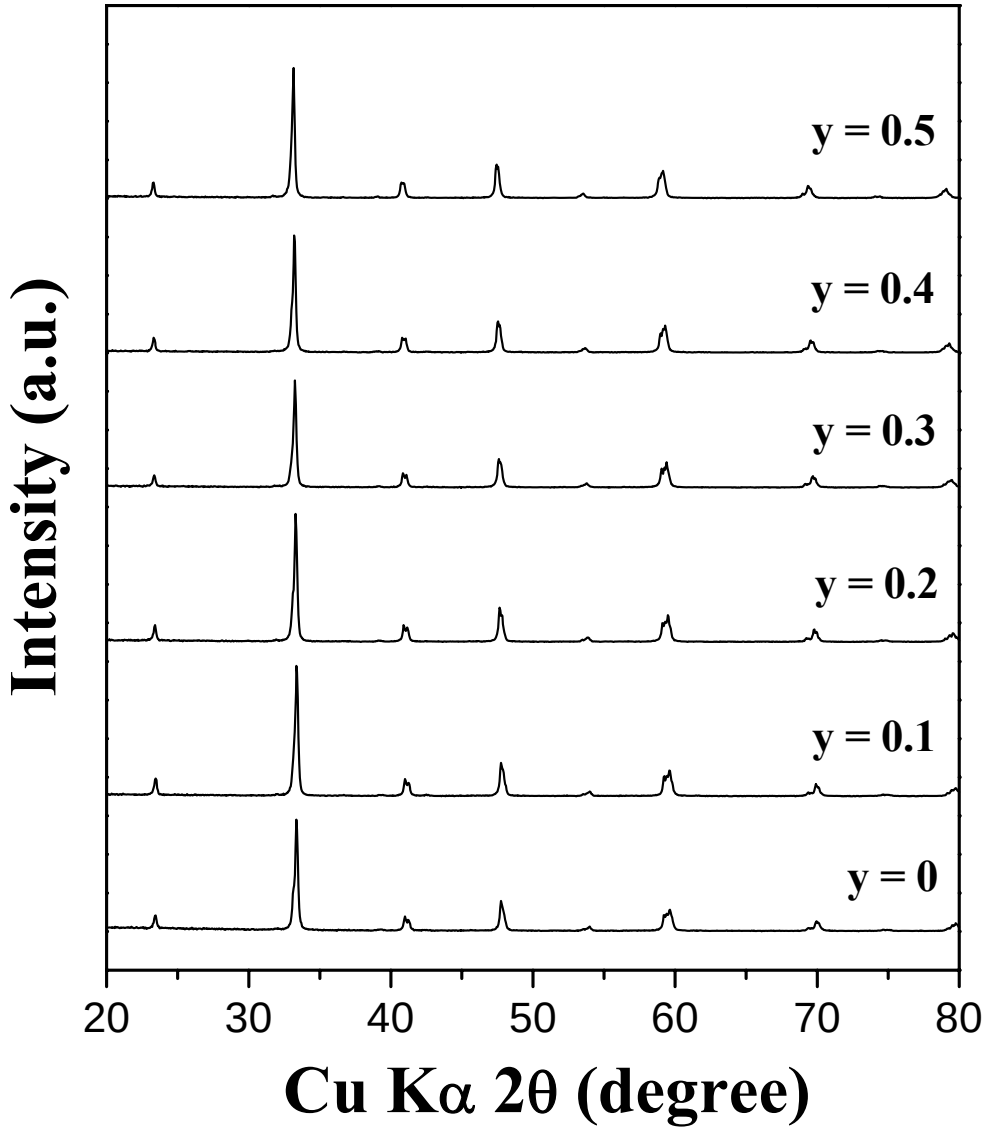

Figure 5.1 X-ray powder diffraction patterns of $Nd_{0.6}Sr_{0.4}Co_{1-y}Fe_yO_{3-\delta}$ sintered at 1200 ^oC for 24 h.

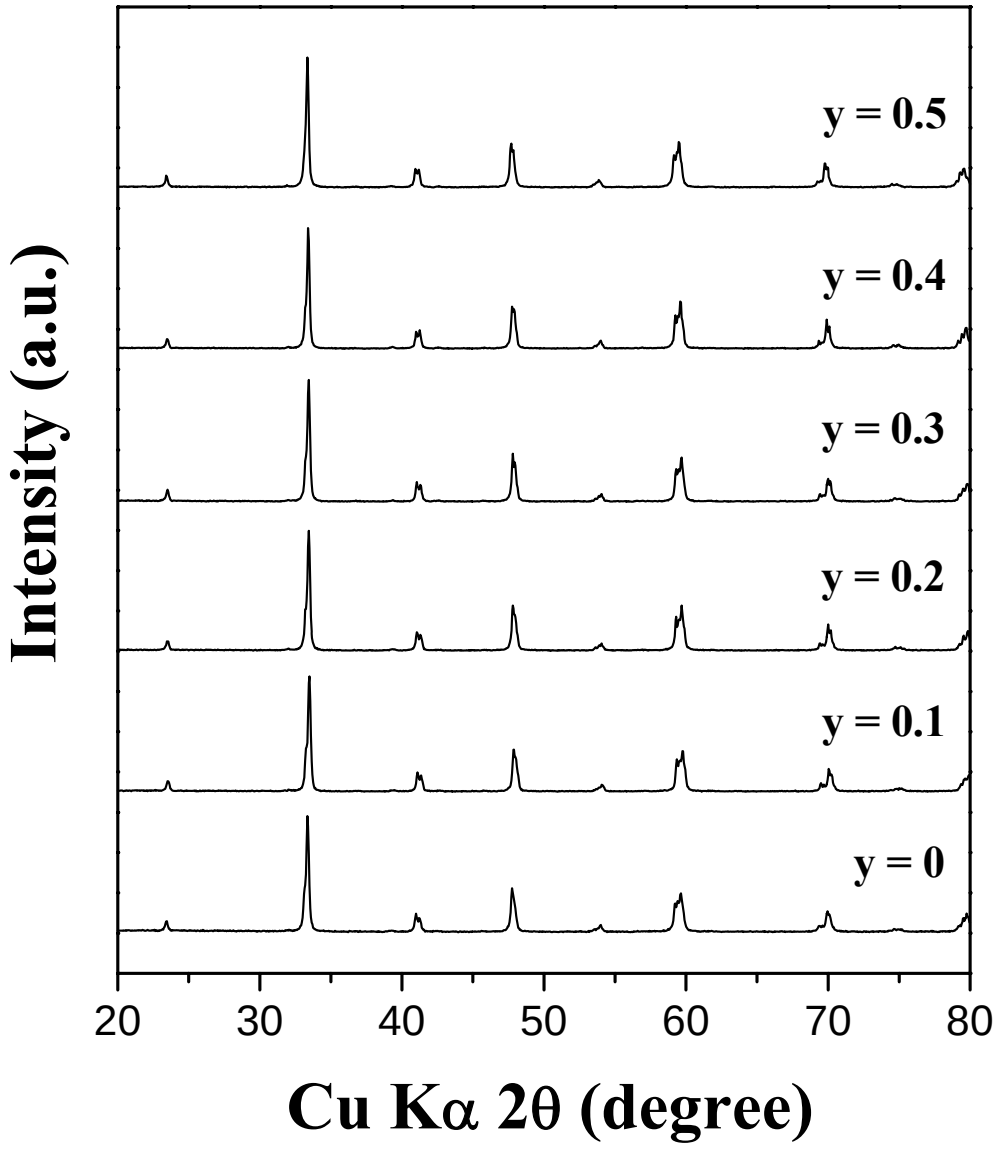

Figure 5.2 X-ray powder diffraction patterns of $Nd_{0.6}Sr_{0.4}Co_{1-y}Mn_yO_{3-\delta}$ sintered at 1300 ^oC for 24 h.

Table 5.1 Crystal chemistry data, BET surface area, and average crystallite size of $Nd_{0.6}Sr_{0.4}Co_{1-y}M_yO_{3-\delta}$ (M = Fe and Mn).

M	y	*a* (Å)	*b* (Å)	*c* (Å)	Lattice volume (Å^3)	BET surface area (m^2/g)	Average crystallite size [a] (Å)
Fe	0.0	5.3626(5)	5.4111(4)	7.5859(8)	220.1	4.8	520
	0.1	5.3693(5)	5.4177(5)	7.5964(7)	221.0	4.0	560
	0.2	5.3783(5)	5.4256(4)	7.6093(7)	222.0	5.0	460
	0.3	5.3867(6)	5.4317(5)	7.6200(8)	223.0	4.9	460
	0.4	5.3974(6)	5.4385(5)	7.6352(7)	224.1	5.2	450
	0.5	5.4113(6)	5.4485(5)	7.6547(8)	225.7	4.2	580
Mn	0.0	5.3626(5)	5.4111(4)	7.5859(8)	220.1	4.2	480
	0.1	5.3632(4)	5.4127(4)	7.5872(6)	220.3	4.3	460
	0.2	5.3677(4)	5.4163(4)	7.5922(6)	220.7	3.1	520
	0.3	5.3691(4)	5.4169(4)	7.5955(6)	220.9	4.1	460
	0.4	5.3757(4)	5.4219(3)	7.6042(5)	221.6	3.6	510
	0.5	5.3839(4)	5.4287(3)	7.6139(5)	222.5	3.8	490

[a] Average crystallite size was estimated with the line broadening of XRD peaks, and the error bar is ± 10 Å.

The TGA plots of the $Nd_{0.6}Sr_{0.4}Co_{1-y}M_yO_{3-\delta}$ samples recorded in air are shown in Figure 5.3. The samples exhibited good reversibility during the heating-cooling cycles in TGA, indicating that the observed weight loss during heating is due to the loss of oxygen from the lattice. Therefore, the relative degree of oxygen loss from the lattice for the samples could be clearly assessed with the TGA curves.

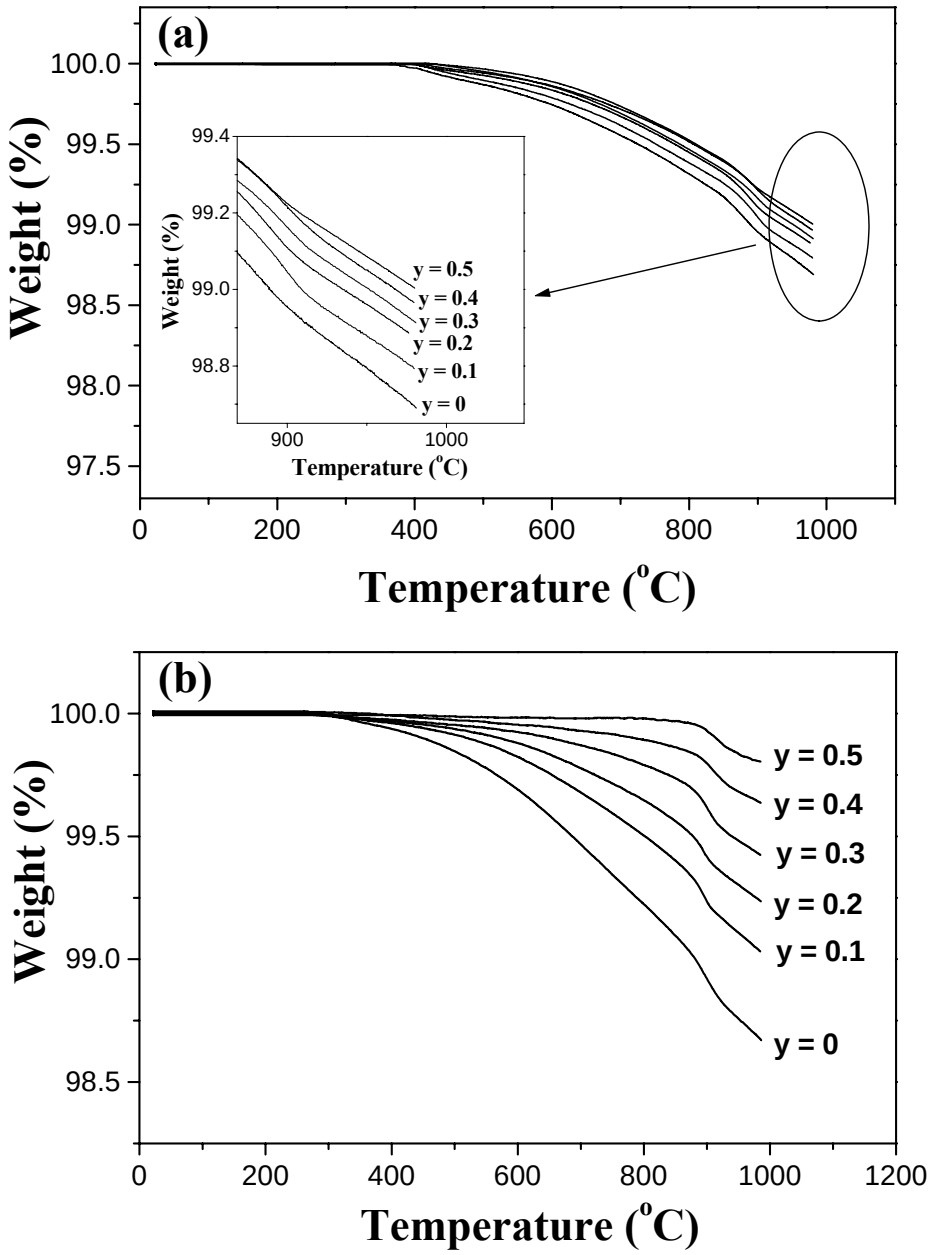

Figure 5.3 TGA plots of $Nd_{0.6}Sr_{0.4}Co_{1-y}M_yO_{3-\delta}$ ($0 \leq y \leq 0.5$) recorded in air with a heating rate of 2 °C/min: (a) M = Fe and (b) M = Mn.

The amount of oxygen loss occurring at high temperatures decreases with increasing Fe or Mn content. Tai *et al.*[58] and Kozhevnikov *et al.*[101] reported a similar trend for the analogous $La_{1-x}Sr_xCo_{1-y}Fe_yO_3$ and $La_{1-x}Sr_xCo_{1-z}Mn_zO_{3-\delta}$ systems respectively. The decrease in the amount of oxygen loss with Fe- and Mn- doping could be attributed to the increase in the binding energy of the oxide ions in the lattice. This is in agreement with the report by Steele[102] that perovskite oxides with Fe^{3+} and Mn^{3+} ions are thermally more stable than those with Co^{3+} ions due to the stronger Fe-O and Mn-O bonds compared to the Co-O bond. It is also in accordance with the finding that the oxygen non-stoichiometry δ in $La_{1-x}Sr_xFeO_{3-\delta}$ and $La_{1-x}Sr_xMnO_{3-\delta}$ is almost fixed at $\delta \approx 0.5x$ over a wide range of pO_2, while that in $La_{1-x}Sr_xCoO_{3-\delta}$ increases with decreasing pO_2.[103,104] Moreover, the degree of oxygen loss decreases more significantly with increasing Mn content than that with increasing Fe content due to a greater stability of Mn^{4+} and stronger Mn-O bonds compared to Fe^{4+} and Fe-O bonds at higher temperatures.

5.3.2 Thermal Expansion Behavior

The average thermal expansion coefficient values of $Nd_{0.6}Sr_{0.4}Co_{1-y}M_yO_{3-\delta}$ (M = Fe and Mn) at 50-700 ^oC in air are plotted as a function of dopant concentration y in Figure 5.4. The TEC values decrease with increasing Fe or Mn content y.

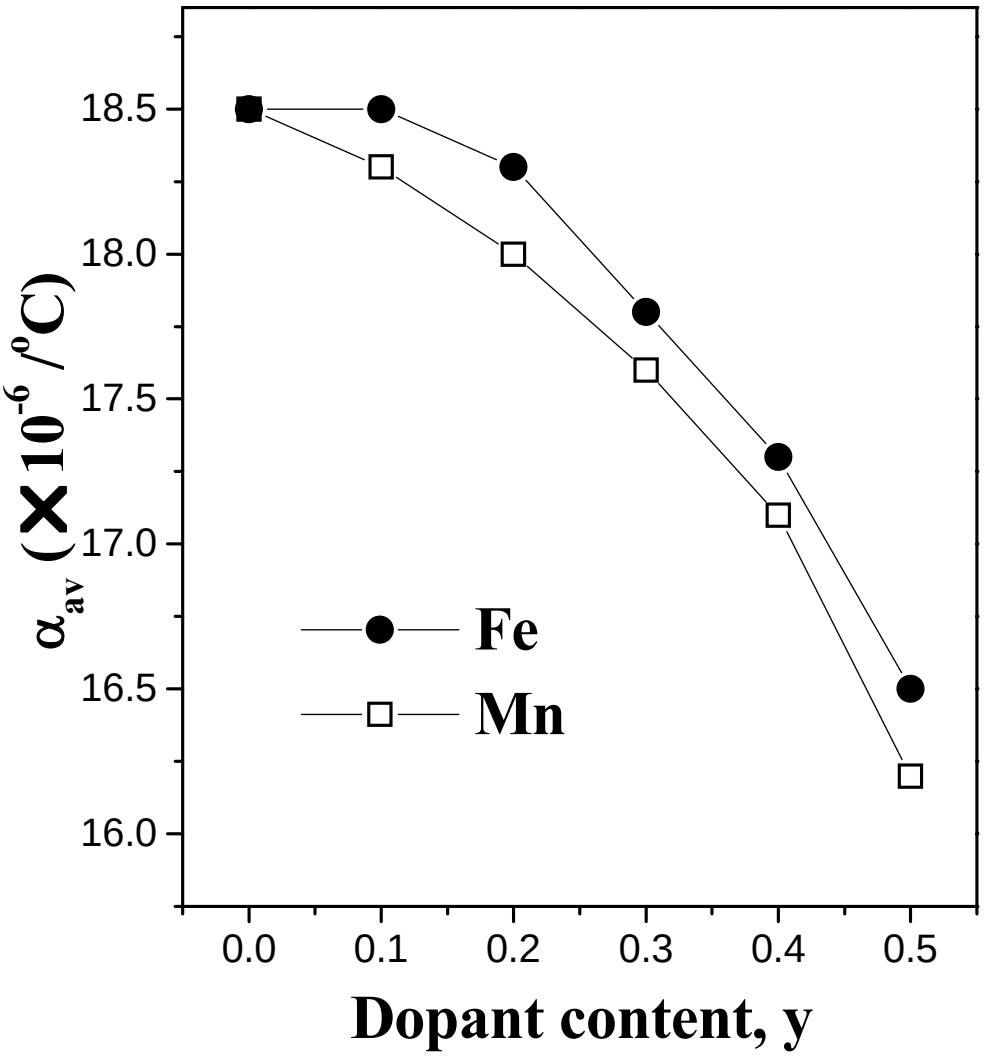

Figure 5.4 Variations of the average thermal expansion coefficients (50-700 ^{o}C) of $Nd_{0.6}Sr_{0.4}Co_{1-y}M_yO_{3-\delta}$ (M = Fe and Mn) with dopant concentration y.

The larger TEC for the cobaltites can be attributed to the following two factors: (i) electronic transition from the low spin Co^{III} state ($t_{2g}^6 e_g^0$) to the high spin Co^{3+} state ($t_{2g}^4 e_g^2$) that is accompanied by an increase in ionic radius from 0.545 Å (low spin) to 0.61 Å (high spin)[75] and (ii) formation of oxygen vacancies that results in a decrease in the formal oxidation state of the transition metal ion and a consequent increase in ionic size.[74] Therefore, the decrease in TEC with Fe^{3+} and Mn^{3+} doping could be understood to be due to a decrease in the Co^{3+} content and a consequent suppression of both the spin state transitions and formation of oxygen vacancies as revealed by the TGA data in Figure 5.3. Furthermore, TEC is inversely proportional to the bonding energy between the ions in the lattice.[74] Thus, the greater decrease in TEC with the Mn doping compared to the Fe doping could be attributed to the stronger Mn-O bond compared to the Fe-O bond.

5.3.3 Electrical Conductivity

The temperature dependence of the electrical conductivity of the $Nd_{0.6}Sr_{0.4}Co_{1-y}M_yO_{3-\delta}$ (M = Fe and Mn) samples is shown in Figure 5.5. The faster decrease in conductivity at higher temperatures could be due to the oxygen loss from the lattice at higher temperatures as indicated by the TGA data (Figure 5.3) and the consequent decrease in carrier concentration. Additionally, the increasing oxygen vacancy concentration can perturb the periodic potential of the (Co,M)-O-(Co,M) network and lead to a trapping of the carriers.

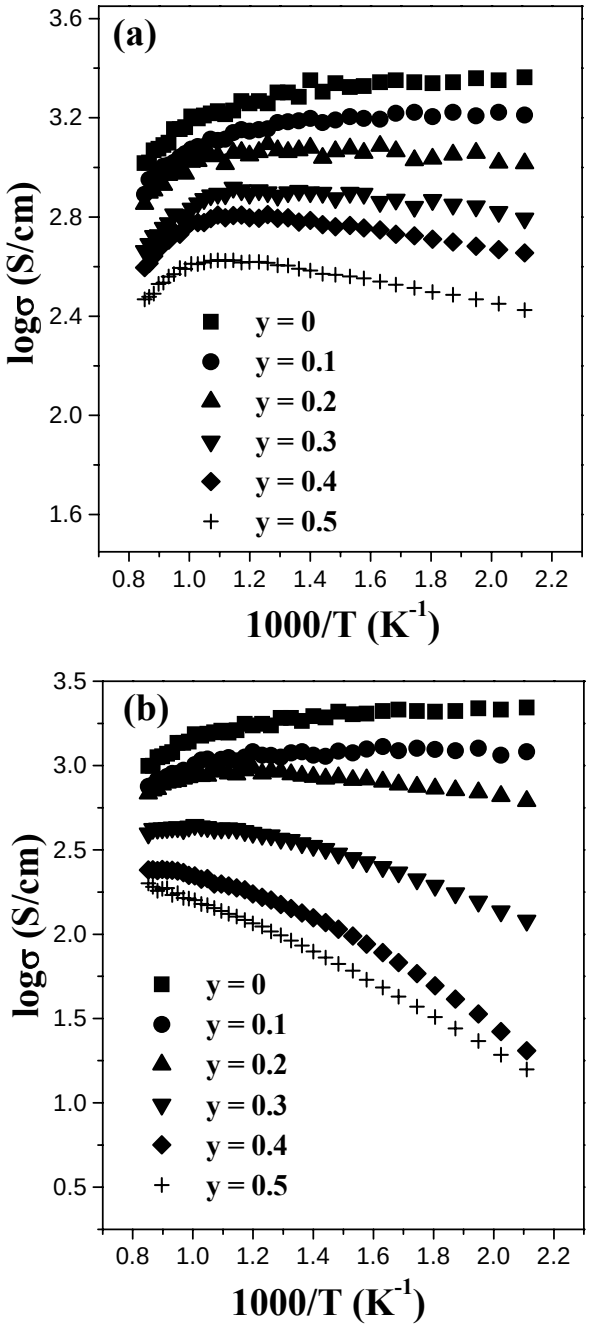

Figure 5.5 Variations of the electrical conductivity measured in air of (a) $Nd_{0.6}Sr_{0.4}Co_{1-y}Fe_yO_{3-\delta}$ and (b) $Nd_{0.6}Sr_{0.4}Co_{1-y}Mn_yO_{3-\delta}$ with temperature for various value of y.

At a given temperature, the electrical conductivity decreases with increasing Fe and Mn contents. The $Nd_{0.6}Sr_{0.4}Co_{1-y}M_yO_{3-\delta}$ (M = Fe and Mn) samples are mixed hopping conductors with more than one type of transition metal ions. It has been reported that the electronic charge compensation occurs preferentially by the formation of Fe^{4+} and Mn^{4+} rather than Co^{4+} on substituting Sr^{2+} for lanthanide ions, respectively, in the $La_{0.6}Sr_{0.4}Co_{1-y}Fe_yO_{3-\delta}$ and $Pr_{1-x}Sr_xCo_{1-y}Mn_yO_{3-\delta}$ systems.[105,106] Thus, the preferential formation of Fe^{4+} and Mn^{4+} compared to Co^{4+} and the decreased covalency of the Fe^{4+}-O and Mn^{4+}-O bonds compared to the Co^{4+}-O bonds result in an increase in the electron localization and a decrease in the electrical conductivity with increasing Fe or Mn content.

The $Nd_{0.6}Sr_{0.4}Co_{1-y}M_yO_{3-\delta}$ (M = Fe and Mn) system exhibits a metal to semiconductor transition around y = 0.2 as seen in Figure 5.5. The metal to semi-conductor transition in $Nd_{0.6}Sr_{0.4}Co_{1-y}M_yO_{3-\delta}$ (M = Fe and Mn) with Fe and Mn doping could be explained by considering the changes in the structural parameters. The end member $Nd_{0.6}Sr_{0.4}CoO_{3-\delta}$ is a metallic conductor with sufficient bandwidth and little or no charge transfer gap between the $Co^{3+/4+}$:3d and O^{2-}:2p bands.[60] The substitution of a larger Fe^{3+} or Mn^{3+} ion for Co^{3+} leads to an increase in the average ionic radius of the B site cations in the ABO_3 perovskite structure, resulting in a decrease in the tolerance factor and an increase in the bending of the O-(Co,M)-O bonds with bond angles of $< 180^o$. The increase in the bending of the O-(Co,M)-O bonds, causing a decrease in the bandwidth and a consequent opening of the charge

transfer gap, could be envisioned to cause a metal to semiconductor transition in the $Nd_{0.6}Sr_{0.4}Co_{1-y}M_yO_{3-\delta}$ (M = Fe and Mn) system with increasing Fe or Mn doping.

The activation energies obtained from the Arrhenius plots of ln(σT) versus 1/T are given in Table 5.2.

Table 5.2 Activation energies (E_a) for electrical conduction in $Nd_{0.6}Sr_{0.4}Co_{1-y}M_yO_{3-\delta}$ (M = Fe and Mn) at 200-700 ^oC in air.

y	E_a for M = Fe (eV)	E_a for M = Mn (eV)
0.2	0.060	0.087
0.3	0.070	0.159
0.4	0.084	0.237
0.5	0.094	0.238

The activation energy increases with increasing Fe and Mn contents. The temperature dependence of the conductivity for a semiconductor can be described by the small polaron hopping mechanism and the activation energy for hopping is strongly related to polaron binding energy and bandwidth. The substitution of a larger Fe^{3+} and Mn^{3+} for Co^{3+} and the preferential formation of Fe^{4+} and Mn^{4+} compared to Co^{4+} result in a bending of the O-(Co,M)-O bonds and deep localization of charge carriers with a decrease in bandwidth. Thus, the decrease in the bandwidth and the increase in polaron binding energy lead to an increase in the activation energy with increasing Fe and Mn contents. For a given degree of doping, the Mn-doped system shows higher

activation energies than the Fe-doped system, which implies a lower covalency and larger charge transfer gap for the former compared to the latter.

5.3.4 Reactivity and Microstructure

The BET surface area and average crystallite size do not vary significantly with y in $Nd_{0.6}Sr_{0.4}Co_{1-y}M_yO_{3-\delta}$ (M = Fe and Mn) as seen in Table 5.1, and so influence of the geometrical morphology on electrochemical performance in this study could be considered negligible. The X-ray powder diffraction patterns of $Nd_{0.6}Sr_{0.4}Co_{1-y}M_yO_{3-\delta}$ (M = Fe and Mn) and LSGM mixtures after heating for 3 h at 1000 ^oC for the Fe-doped cathode and 1100 ^oC for the Mn-doped cathode are shown in Figure 5.6. No reaction product is observed for all compositions. Typical SEM micrographs of the cross-section of $Nd_{0.6}Sr_{0.4}Co_{0.7}Fe_{0.3}O_{3-\delta}$ and $Nd_{0.6}Sr_{0.4}Co_{0.8}Mn_{0.2}O_{3-\delta}$ porous cathodes on LSGM electrolyte after firing for 3 h at 1000 ^oC and 1100 ^oC, respectively, are shown in Figure 5.7. Appropriate area contact between grains and good adhesion between the cathode and electrolyte are also observed.

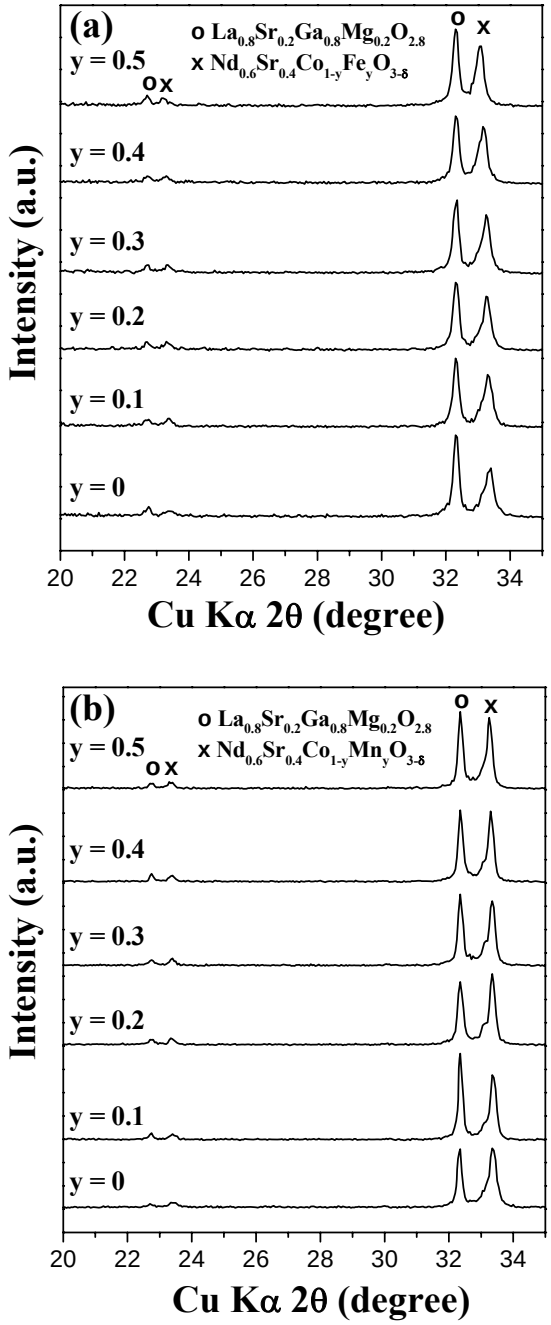

Figure 5.6 X-ray powder diffraction patterns recorded after heating the $Nd_{0.6}Sr_{0.4}Co_{1-y}M_yO_{3-\delta}$ cathode and the LSGM electrolyte powders for 3 h at (a) 1000 ^oC for the Fe-doped composition and (b) 1100 ^oC for the Mn-doped composition.

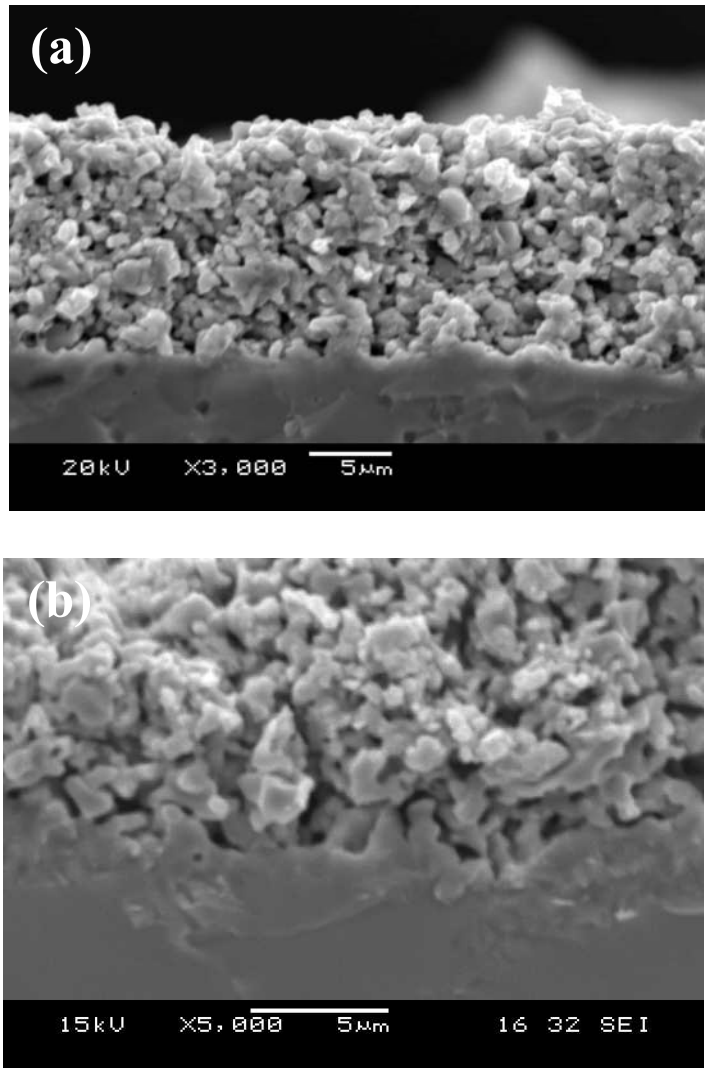

Figure 5.7 SEM micrographs of (a) $Nd_{0.6}Sr_{0.4}Co_{0.7}Fe_{0.3}O_{3-\delta}$ cathode and (b) $Nd_{0.6}Sr_{0.4}Co_{0.8}Mn_{0.2}O_{3-\delta}$ cathode on LSGM electrolyte after firing for 3 h at 1000 ^{o}C for the Fe-doped composition and 1100 ^{o}C for the Mn-doped composition, respectively.

5.3.5 Electrochemical Performance

The variations of the power density and the over-potential with current density at 800 ^{o}C for the various $Nd_{0.6}Sr_{0.4}Co_{1-y}M_yO_{3-\delta}$ (M = Fe and Mn) cathode compositions are shown in Figures 5.8 and 5.9. The power density decreases and the over-potential increases with increasing Fe and Mn contents y. Oxygen reduction at a porous cathode is closely related not only to the charge transfer and the adsorption/dissociation of oxygen, but also to the transport speed of oxide ions through the cathode bulk and across the cathode/electrolyte interface. High oxide ion vacancy concentration in the surface of cathode materials could improve oxygen exchange (the adsorption/dissociation of oxygen molecule). The oxide ion vacancies and electrical conductivity decrease with increasing Fe and Mn doping as seen in Figures 5.3 and 5.5. Thus, the decrease in the oxygen exchange, charge transfer, and transport speed of oxide ions caused by a decrease in the oxygen vacancy concentration and electrical conductivity with a substitution of Fe or Mn for Co leads to an increase in over-potential or a decrease in catalytic activity. Additionally, the rapid increase in over-potential for the Mn-doped system compared to the Fe-doped system is due to a faster decrease in the oxide ion and electronic conductivities.

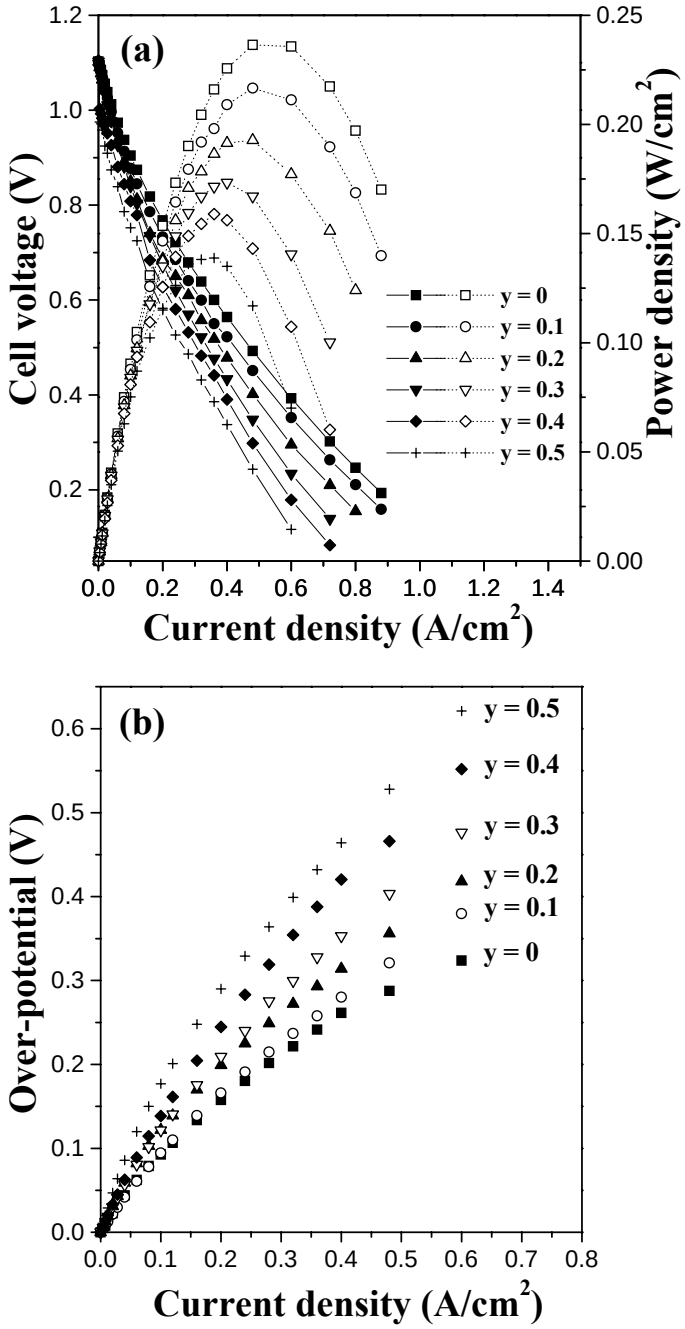

Figure 5.8 Electrochemical performance data of $Nd_{0.6}Sr_{0.4}Co_{1-y}Fe_yO_{3-\delta}$/LSGM/Ni-GDC single cells at 800 ^oC: variations of (a) the I-V curve (closed symbols) and power density (open symbols) and (b) cathode over-potential.

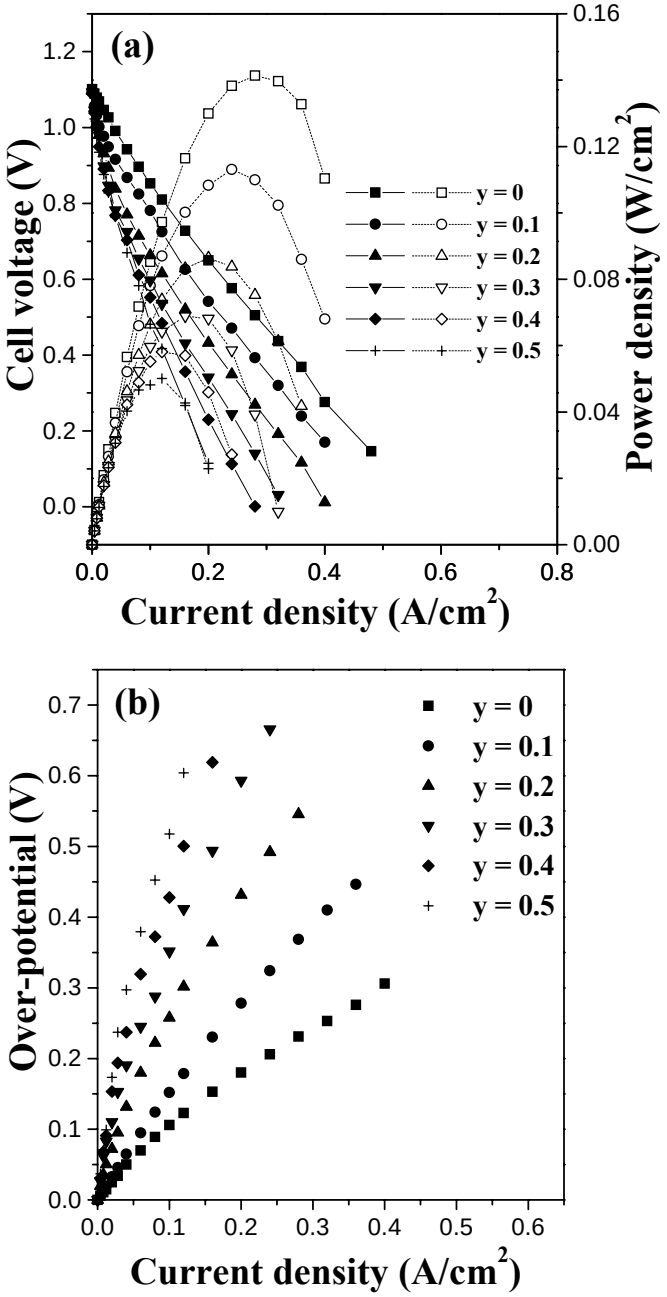

Figure 5.9 Electrochemical performance data of $Nd_{0.6}Sr_{0.4}Co_{1-y}Mn_yO_{3-\delta}$/LSGM/Ni-GDC single cells at 800 ^oC: variations of (a) the I-V curve (closed symbols) and power density (open symbols) and (b) cathode over-potential.

5.4 CONCLUSIONS

$Nd_{0.6}Sr_{0.4}Co_{1-y}M_yO_{3-\delta}$ (M = Fe and Mn) perovskite oxides have been synthesized for $0 \leq y \leq 0.5$ and characterized as cathode materials for intermediate temperature SOFC. All the compositions have an orthorhombic structure and the lattice volume increase with increasing Fe and Mn content. The oxygen non-stoichiometry δ decreases with Fe and Mn doping due to stronger Fe-O and Mn-O bonds compared to the Co-O bonds. The electrical conductivity decreases with increasing Fe and Mn content due to the increased carrier localization, and the system exhibits a metal to semiconductor transition around y = 0.2 due to a decrease in the O-(Co,M)-O bond angle below 180^o and a consequent decrease in the bandwidth with Fe and Mn doping. The thermal expansion coefficient decreases with increasing Fe and Mn contents due to a suppression of the spin state transitions associated with Co^{3+} and an increase in the bonding energy between the $M^{3+/4+}$ and O^{2-} ions in the lattice. The substitution of $Fe^{3+/4+}$ and $Mn^{3+/4+}$ for $Co^{3+/4+}$ decreases the mobility of the oxide ions as well as the electronic conductivity, which leads to a decrease in electrocatalytic activity. The Fe-doped system exhibits higher electrocatalytic activity but larger TEC than the Mn-doped system. Although Fe and Mn dopings decrease the catalytic activity, they offer an important advantage of lowering the TEC.

CHAPTER 6

ELECTROCHEMICAL PERFORMANCE OF $Nd_{0.6}Sr_{0.4}Co_{0.5}Fe_{0.5}O_{3-\delta}$-Ag COMPOSITE CATHODE MATERIALS

6.1 INTRODUCTION

As discussed in the previous chapters, the Co rich perovskite systems exhibit large thermal expansion coefficient. With an aim to reduce the TEC, various strategies such as the replacement of La by other smaller lanthanides, or the substitution of Co by Fe or Mn have been pursued.[59-62,107] For instance, the $Nd_{0.6}Sr_{0.4}Co_{0.5}Fe_{0.5}O_{3-\delta}$ composition exhibits a smaller TEC (16.7×10^{-6} $^{o}C^{-1}$)[108] than $La_{0.6}Sr_{0.4}CoO_{3-\delta}$ (21.3×10^{-6} $^{o}C^{-1}$)[109] due to the substitution of both Nd for La and Fe for Co, but its electrocatalytic activity is lower than that of $La_{0.6}Sr_{0.4}CoO_{3-\delta}$ due to the reduced electronic and ionic conductivities as shown in Chapter 5.

It is well known that the addition of precious metals such as Pt into porous cathodes enhances the electrocatalytic activity.[110-113] Ag is also known to improve the electrocatalytic properties for the oxygen reduction reaction,[114] and several oxide-Ag cermet cathodes have been found to show good electrochemical performance.[115-118] With an aim to improve the electrocatalytic activity of $Nd_{0.6}Sr_{0.4}Co_{0.5}Fe_{0.5}O_{3-\delta}$ while taking advantage of its lower TEC,[108] this chapter explores the fabrication and electrochemical performance of the $Nd_{0.6}Sr_{0.4}Co_{0.5}Fe_{0.5}O_{3-\delta}$-Ag composite cathodes for the oxygen reduction reaction in intermediate temperature SOFC. The

electrochemical performances of SOFC single cells having the composite cathodes that were prepared by a ball milling and an impregnation methods followed by firing at different temperatures are compared.

6.2 EXPERIMENTAL

6.2.1 Materials Synthesis

The $Nd_{0.6}Sr_{0.4}Co_{0.5}Fe_{0.5}O_{3-\delta}$ powder was synthesized by a coprecipitation method. Required amounts of Nd_2O_3, $SrCO_3$, $Co(CH_3COO)_2{\cdot}4H_2O$, and $Fe(CH_3COO)_2$ were dissolved in dilute nitric acid and the metal ions were coprecipitated as carbonates and hydroxides by adding a mixture of KOH and K_2CO_3. The coprecipiate was washed with deionized water, dried, fired at 500 ^oC for 5 h, ground, and finally fired at 1200 ^oC for 24 h. The composite cathode powders were then prepared by ball milling the $Nd_{0.6}Sr_{0.4}Co_{0.5}Fe_{0.5}O_{3-\delta}$ powders with various amounts of Ag_2O for 24 h using a zirconia ball medium. The particle sizes of $Nd_{0.6}Sr_{0.4}Co_{0.5}Fe_{0.5}O_{3-\delta}$ and Ag_2O after ball milling were, respectively, 0.3 and 0.5 μm as estimated from the line broadening of the X-ray diffraction peaks using the Scherrer equation as given in Chapter 2. The LSGM electrolyte disks and the NiO-$Ce_{0.9}Gd_{0.1}O_{1.95}$ (GDC) cermet (Ni:GDC = 70:30 vol %) anode powder were prepared by solid-state reaction and glycine-nitrate combustion method, respectively, as described in Chapter 2.

6.2.2 Fabrication of Single Cells

The ball milled $Nd_{0.6}Sr_{0.4}Co_{0.5}Fe_{0.5}O_{3-\delta}$-$Ag_2O$ composite cathodes were first screen printed onto 0.8 mm thick LSGM electrolyte pellet, and then transformed to $Nd_{0.6}Sr_{0.4}Co_{0.5}Fe_{0.5}O_{3-\delta}$-Ag composite by firing at 920 ^oC for 3 h. With an aim to have a better dispersion of the Ag particles, the $Nd_{0.6}Sr_{0.4}Co_{0.5}Fe_{0.5}O_{3-\delta}$-Ag composite cathodes were also fabricated by an impregnation method. In this case, the porous $Nd_{0.6}Sr_{0.4}Co_{0.5}Fe_{0.5}O_{3-\delta}$ cathodes were first prepared by screen printing onto an 0.8 mm thick LSGM electrolyte, followed by firing at 1100 ^oC for 3 h. The porous $Nd_{0.6}Sr_{0.4}Co_{0.5}Fe_{0.5}O_{3-\delta}$ cathodes were then impregnated with an aqueous $AgNO_3$ solution, followed by firing at 700 ^oC for 3 h. The amount of Ag particles loaded in the impregnation method was 0.1 mg/cm^2 (~ 0.5 wt. %). The NiO-GDC cermet anode was also prepared by screen printing onto LSGM electrolyte pellet, followed by firing at 1200 ^oC for 3 h as described in Chapter 2.

6.2.3 Characterization

Microstructural characterizations were carried out with a Hitachi field emission scanning electron microscope (SEM). AC impedance analysis and current-voltage (I-V) measurements of the single cells were carried out as described in Chapter 2.

6.3 RESULTS AND DISCUSSION

6.3.1 Electrochemical Performance of the Ball Milled $Nd_{0.6}Sr_{0.4}Co_{0.5}Fe_{0.5}O_{3-\delta}$-Ag Composite Cathodes

The I-V curves and the over-potentials at 800 ^{o}C for the composite cathodes containing different amounts of Ag that were prepared by ball milling the $Nd_{0.6}Sr_{0.4}Co_{0.5}Fe_{0.5}O_{3-\delta}$ powders with required amounts of Ag_2O are compared in Figure 6.1. The cathode with 3 wt. % Ag shows the best electrochemical performance. Figure 6.2 shows the effect of Ag incorporation on the power density and over-potential at 0.24 A/cm^2. The power density increases with the Ag content, reaches a maximum at 3 wt. % Ag, and then decreases, with the over-potential correspondingly reaching a minimum at 3 wt. % Ag. The performance of the cathodes is strongly influenced by both the electronic and oxide ion conductivities of the electrode. The initial improvement in the electrochemical performance with Ag incorporation (up to ~ 3 wt. %) is due to an increase in the electronic conductivity and catalytic activity while maintaining adequate amount of reaction sites, *e.g.* the three-phase boundary (TPB). However, with > 3 wt. % Ag, the continuity of the oxide ion conducting paths within the $Nd_{0.6}Sr_{0.4}Co_{0.5}Fe_{0.5}O_{3-\delta}$ network may be interrupted by the Ag particles, which is not an oxide ion conductor, resulting in a blocking of oxide ion conduction and consequent decrease in electrochemical performance despite an increase in the overall electronic conductivity.

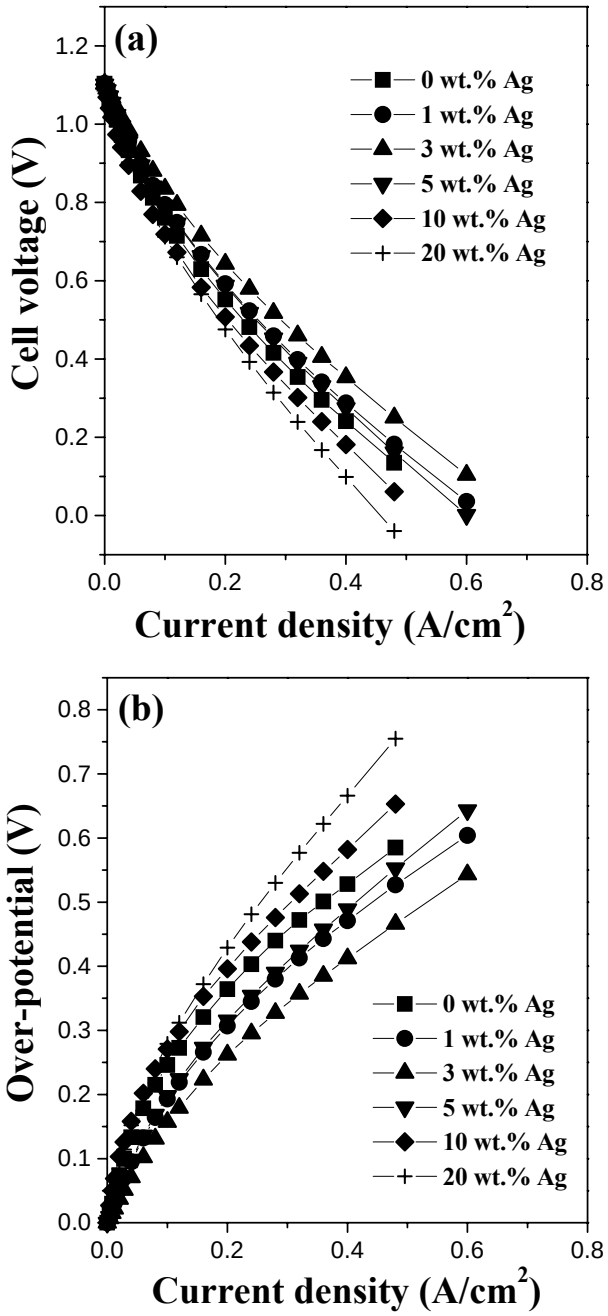

Figure 6.1 Electrochemical performance data at 800 ^{o}C of $Nd_{0.6}Sr_{0.4}Co_{0.5}Fe_{0.5}O_{3-\delta}$-Ag/LSGM/Ni-GDC single cells with various amount of Ag incorporated into the cathode by ball milling followed by firing at 920 ^{o}C: Variations of (a) the I-V curves and (b) cathode over-potential.

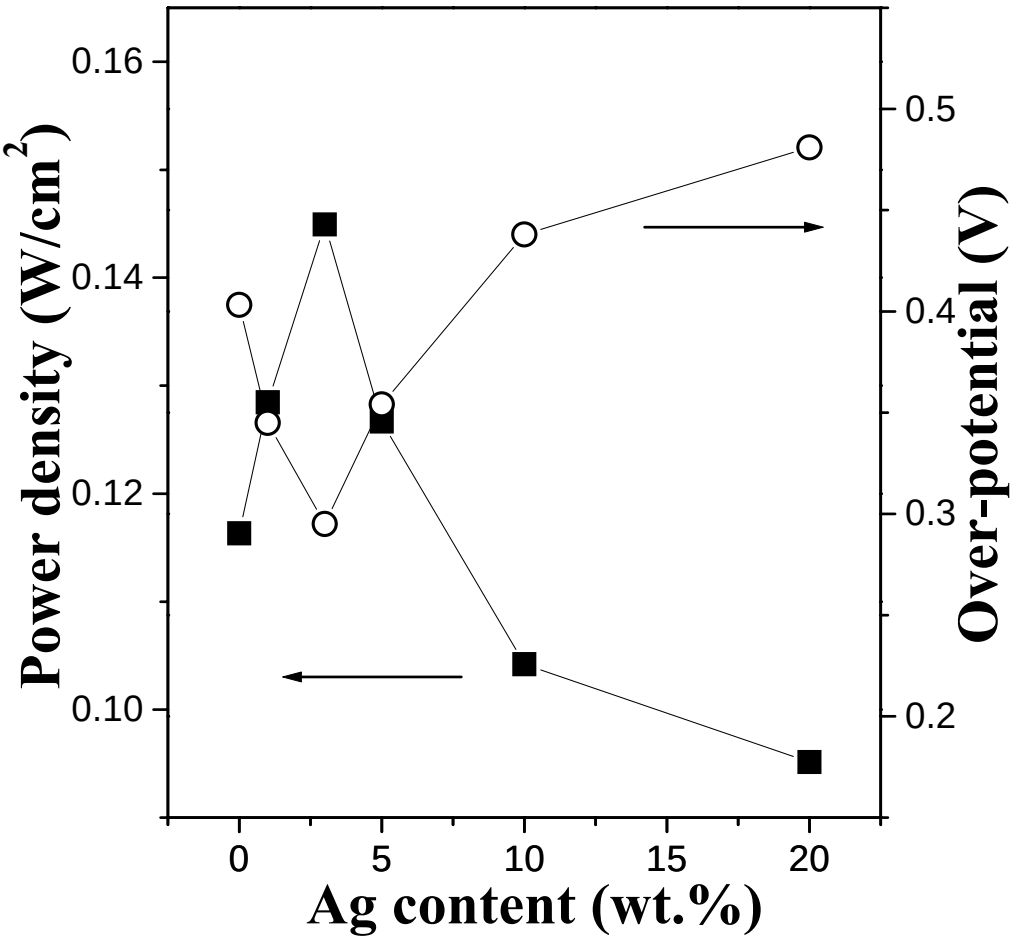

Figure 6.2 Variations of the power density and cathode over-potential with Ag content at 0.24 A/cm^2 and 800 ^{o}C. The cathodes were fabricated by ball milling followed by firing at 920 ^{o}C as in Figure 6.1.

Figure 6.3 compares the AC impedance spectra recorded at 800 ^{o}C in air of the ball milled $Nd_{0.6}Sr_{0.4}Co_{0.5}Fe_{0.5}O_{3-\delta}$-Ag cathodes containing various amount of Ag after firing at 920 ^{o}C.

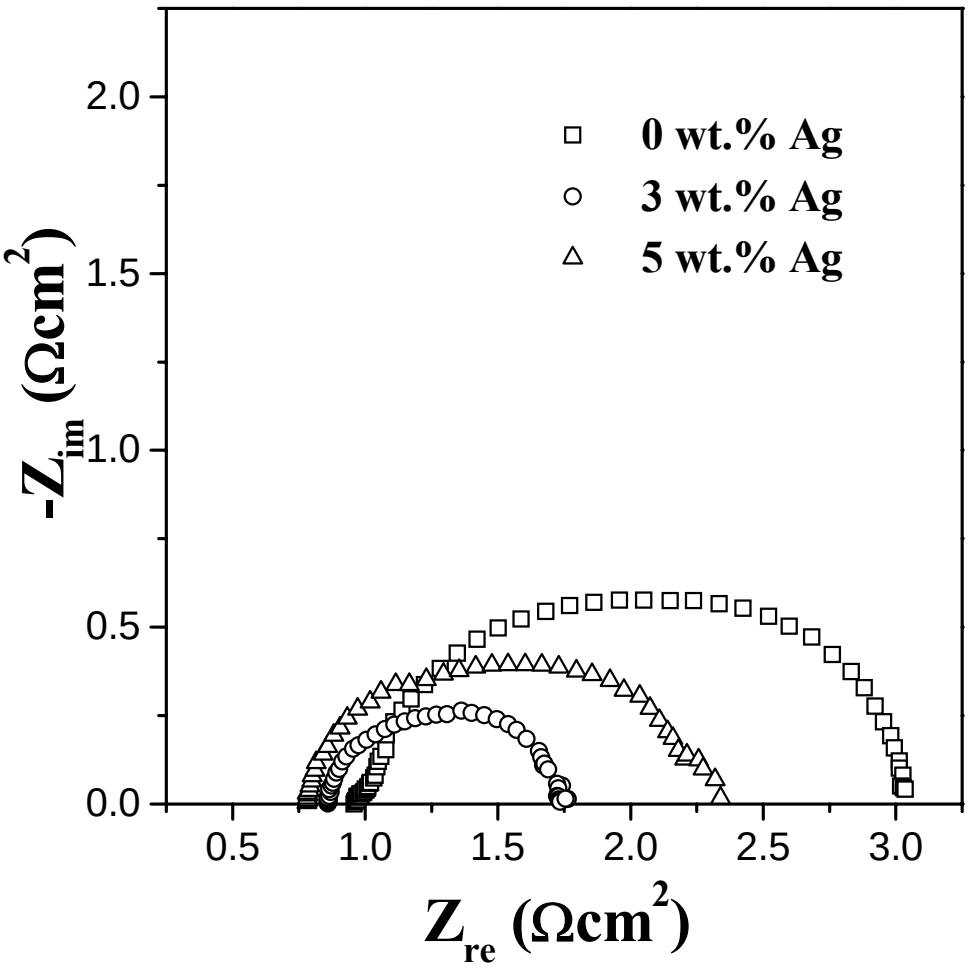

Figure 6.3 Typical AC impedance spectra recorded at 800 ^{o}C in air of the ball milled $Nd_{0.6}Sr_{0.4}Co_{0.5}Fe_{0.5}O_{3-\delta}$-Ag cathodes with various amount of Ag after firing at 920 ^{o}C for 3 h.

The ohmic resistance R_b (left intercept on Z_{re} axis), total resistance R_{tot} (right intercept on Z_{re} axis), and polarization resistance R_p ($R_{tot} - R_b$) at 800 ^oC in air that were calculated from the AC impedance spectra are given in Table 6.1.

Table 6.1 The ohmic resistance R_b, total resistance R_{tot}, and polarization resistance R_p of the ball milled $Nd_{0.6}Sr_{0.4}Co_{0.5}Fe_{0.5}O_{3-\delta}$-Ag composite cathodes at 800 ^oC in air.

Ag content (wt.%)	R_b (Ω/cm^2)	R_{tot} (Ω/cm^2)	R_p (Ω/cm^2)
0	0.97	3.02	2.05
3	0.86	1.73	0.87
5	0.78	2.34	1.56

While the ohmic resistance decreases with increasing Ag content, the polarization resistance decreases significantly at 3 wt. % Ag and then increases again at 5 wt. % Ag. This result is consistent with the single cell performance data in Figures 6.1 and 6.2. The data suggest that the ohmic resistance decreases due to an increase in electronic conductivity and better adhesion with the addition of Ag, while the polarization resistance decreases first due to an increase in catalytic activity at 3 wt. % Ag, but increases then due to an interruption of the oxide ion conduction by the Ag particles at 5 wt. % Ag.

6.3.2 Microstructural Analysis

The main drawback with the above ball milled $Nd_{0.6}Sr_{0.4}Co_{0.5}Fe_{0.5}O_{3-\delta}$-Ag composite cathodes is a poor adhesion between the cathode and the LSGM electrolyte due to the low firing temperature (920 ^{o}C) employed, which is dictated by the melting point of Ag (961 ^{o}C). Impregnation is known to be an effective method to incorporate highly dispersed fine particles into porous electrode structures without interrupting the matrix network.[119] Figure 6.4 compares the back-scattered SEM micrographs of the $Nd_{0.6}Sr_{0.4}Co_{0.5}Fe_{0.5}O_{3-\delta}$ cathodes with and without Ag after firing at various temperatures for 3 h. The cathodes with and without Ag after firing at 920 ^{o}C (Figures 6.4a and 6.4b) show only point contact between the particles and poor adhesion between the cathode and the electrolyte. On the other hand, the cathodes without Ag after firing at 1100 ^{o}C (Figure 6.4c) and the cathodes with impregnated Ag followed by firing at 700 ^{o}C (but the LSGM-$Nd_{0.6}Sr_{0.4}Co_{0.5}Fe_{0.5}O_{3-\delta}$ assembly was prepared first by firing at 1100 ^{o}C) (Figure 6.4d) show good area contact and adhesion with the electrolyte with similar microstructures, suggesting that the impregnation of Ag does not affect the microstructure adversely. However, it was not possible to visualize the Ag particles in the impregnated cathode by SEM due to the very small amount of Ag (~ 0.5 wt. %). Uhlenbruck *et al.*[117] have also reported similar difficulties with the $La_{0.65}Sr_{0.3}MnO_3$-Ag composite system containing 1 wt. % Ag.

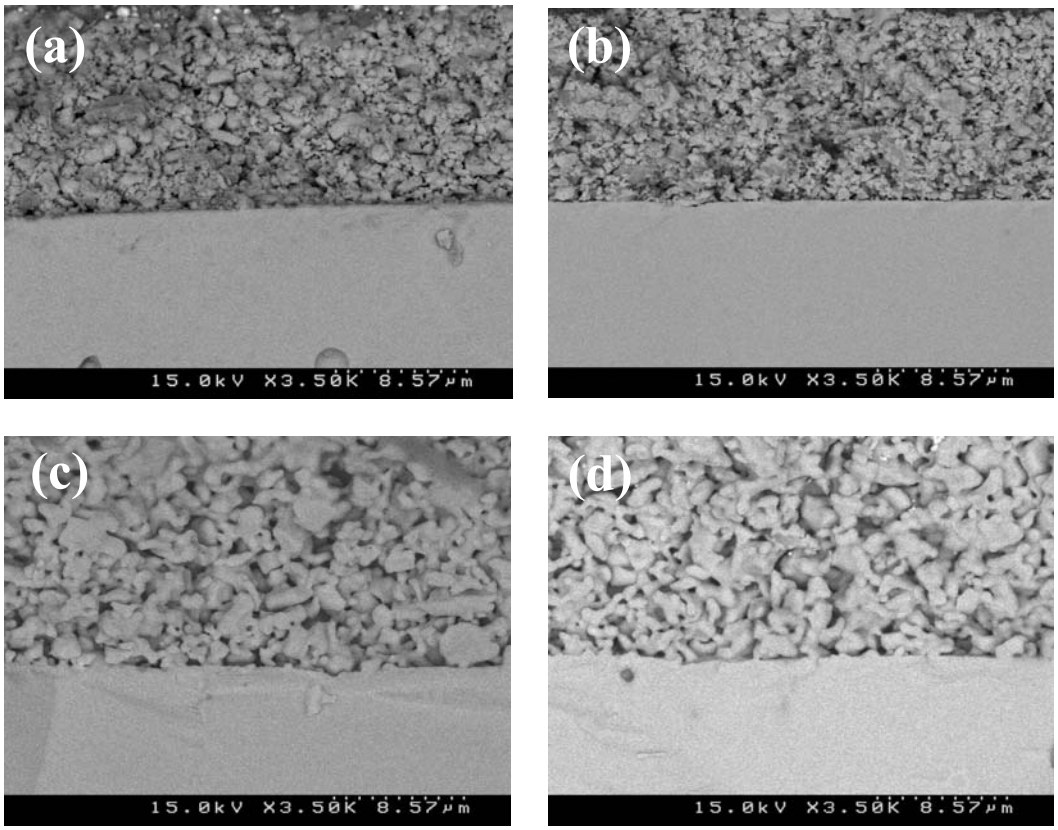

Figure 6.4 Back-scattered SEM micrographs of the cathodes after firing at various temperatures for 3 h: (a) $Nd_{0.6}Sr_{0.4}Co_{0.5}Fe_{0.5}O_{3-\delta}$ without Ag (920 ^{o}C), (b) $Nd_{0.6}Sr_{0.4}Co_{0.5}Fe_{0.5}O_{3-\delta}$ with 3 wt. % Ag (920 ^{o}C), (c) $Nd_{0.6}Sr_{0.4}Co_{0.5}Fe_{0.5}O_{3-\delta}$ without Ag (1100 ^{o}C), and (d) $Nd_{0.6}Sr_{0.4}Co_{0.5}Fe_{0.5}O_{3-\delta}$ impregnated with 0.1 mg/cm^2 Ag (1100 ^{o}C). The temperature in (d) refers to the firing of the LSGM-$Nd_{0.6}Sr_{0.4}Co_{0.5}Fe_{0.5}O_{3-\delta}$ assembly before impregnating Ag.

6.3.3 Effect of Ag Impregnation on Electrochemical Performance

Figure 6.5 compares the AC impedance spectra recorded at 800 ^{o}C in air of the $Nd_{0.6}Sr_{0.4}Co_{0.5}Fe_{0.5}O_{3-\delta}$ cathodes without Ag after firing at 1100 ^{o}C and the $Nd_{0.6}Sr_{0.4}Co_{0.5}Fe_{0.5}O_{3-\delta}$ cathodes after firing at 1100 ^{o}C for 3 h followed by impregnating 0.1 mg/cm^2 (~ 0.5 wt. %) of Ag and finally firing at 700 ^{o}C for 3 h. Both the ohmic and polarization resistances of the cathodes at 800 ^{o}C are reduced by the impregnation of Ag. The temperature dependences of the ohmic (R_b) and polarization (R_p) resistances are shown in Figure 6.6. While the ohmic resistance of the cathode with Ag at any temperature is only slightly lower than that of the cathode without Ag, the polarization resistance is much lower than that of the cathode without Ag. Especially, the polarization resistance at 650 ^{o}C is reduced by about 40 % with 0.5 wt. % impregnated Ag. This observation suggests that the Ag catalyst within the $Nd_{0.6}Sr_{0.4}Co_{0.5}Fe_{0.5}O_{3-\delta}$ cathode works more effectively at lower temperatures.

Figure 6.7 shows the effect of the firing temperature and Ag impregnation on the electrochemical performance. The single cells with and without Ag cathode fired at 1100 ^{o}C show better electrochemical performance compared to those fired at 920 ^{o}C. The better performance of the former cathodes is due to the good area contact among the cathode particles as well as the good adhesion between the cathode and electrolyte, as seen in Figure 6.4. More importantly, with the same firing temperature of 920 or 1100 ^{o}C, the cathodes impregnated with 0.1 mg/cm^2 (~ 0.5 wt. %) Ag exhibit better electrochemical performance compared to those without Ag.

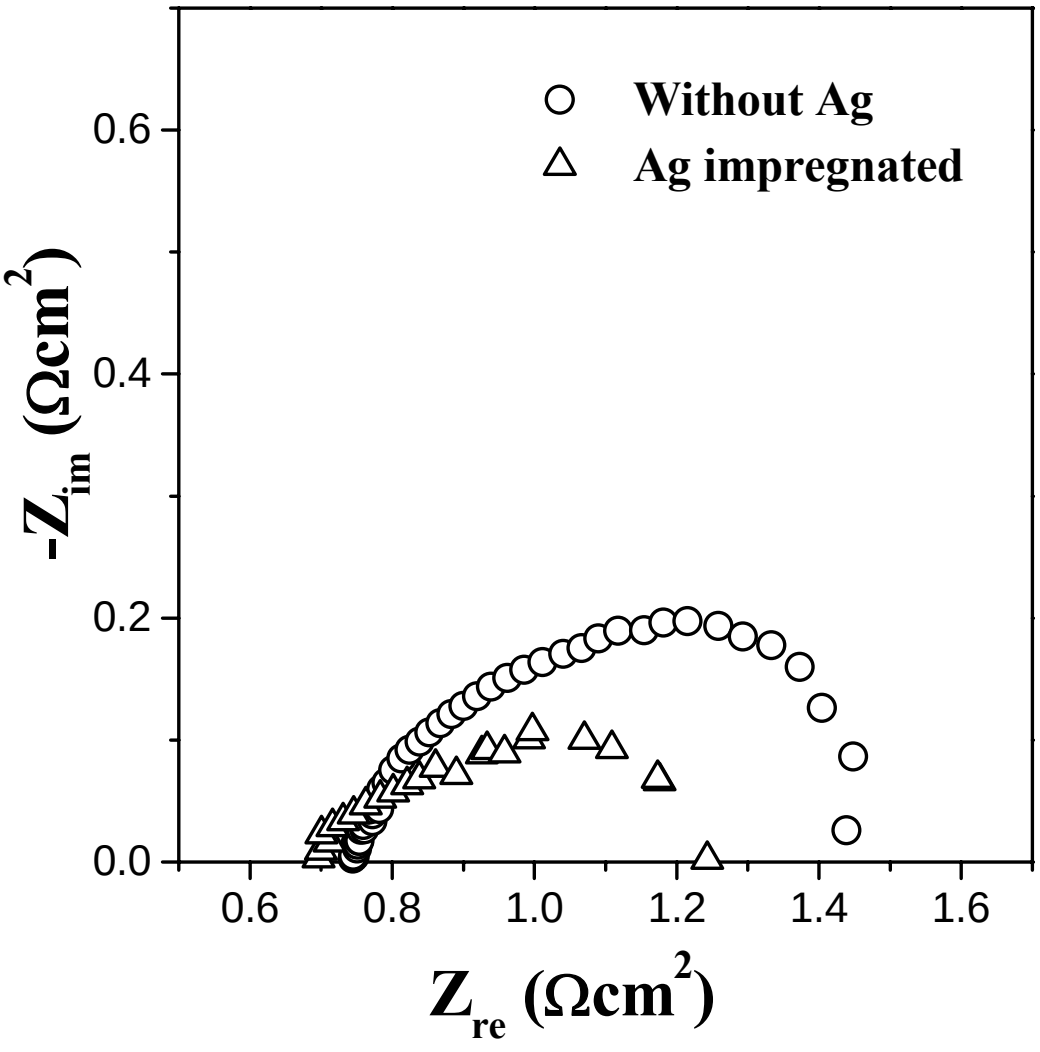

Figure 6.5 Typical AC impedance spectra recorded at 800 ^{o}C in air of the $Nd_{0.6}Sr_{0.4}Co_{0.5}Fe_{0.5}O_{3-\delta}$ cathode without Ag after firing at 1100 ^{o}C for 3 h and the $Nd_{0.6}Sr_{0.4}Co_{0.5}Fe_{0.5}O_{3-\delta}$ cathode after firing at 1100 ^{o}C for 3 h followed by impregnating with 0.1 mg/cm^2 of Ag and finally firing at 700 ^{o}C for 3 h.

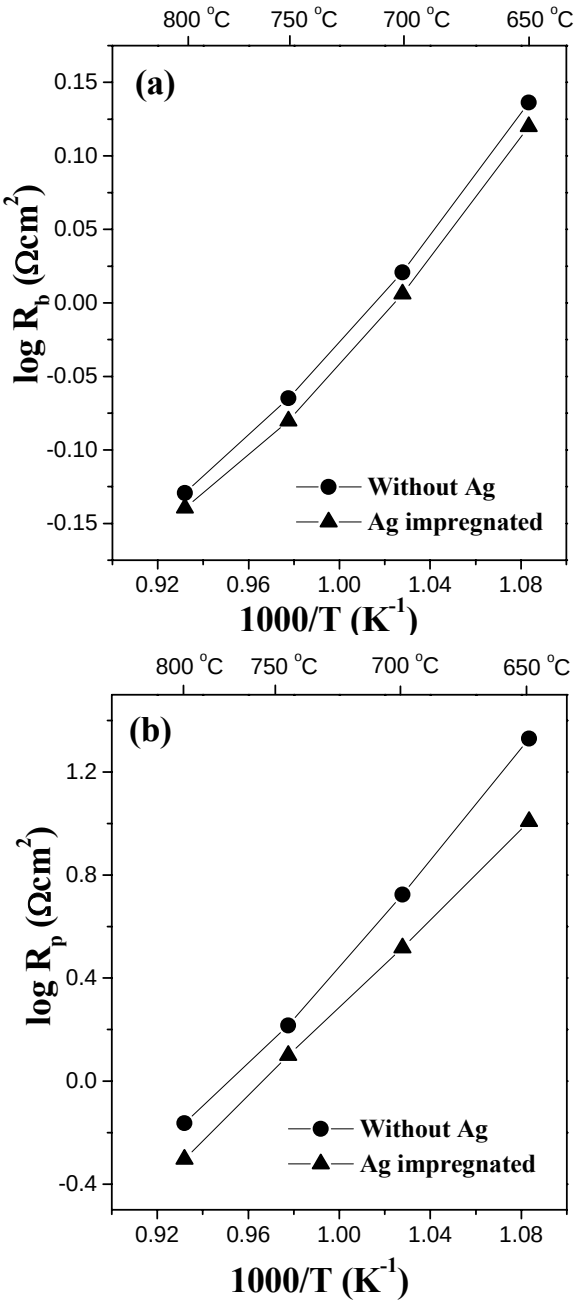

Figure 6.6 Temperature dependence of (a) ohmic (R_b) and (b) polarization (R_p) resistances of the $Nd_{0.6}Sr_{0.4}Co_{0.5}Fe_{0.5}O_{3-\delta}$ cathode without Ag after firing at 1100 °C for 3 h and the $Nd_{0.6}Sr_{0.4}Co_{0.5}Fe_{0.5}O_{3-\delta}$ cathode after firing at 1100 °C for 3 h followed by impregnating with 0.1 mg/cm^2 of Ag and finally firing at 700 °C for 3 h. The results were derived from the impedance data.

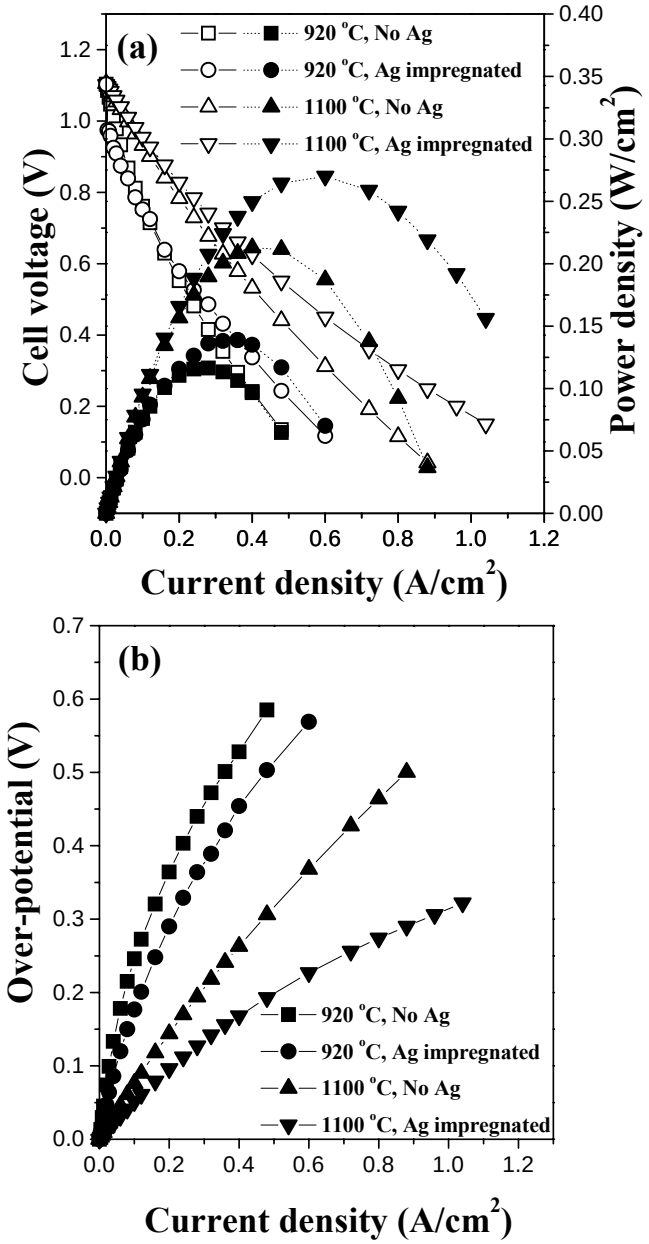

Figure 6.7 Electrochemical performance data at 800 °C of the single cells fabricated with $Nd_{0.6}Sr_{0.4}Co_{0.5}Fe_{0.5}O_{3-\delta}$ cathodes with and without Ag after firing at 920 or 1100 °C for 3 h: Variations of (a) the I-V curves (open symbols) and power density (closed symbols), and (b) cathode over-potentials. In the case of 1100 °C firing temperature with impregnated Ag, the LSGM-$Nd_{0.6}Sr_{0.4}Co_{0.5}Fe_{0.5}O_{3-\delta}$ assembly was first fired at 1100 °C before impregnating Ag and then fired at 700 °C for 3 h, after impregnating Ag.

The cathode impregnated with 0.1 mg/cm^2 (~ 0.5 wt. %) Ag with a firing temperature of 1100 ^{o}C exhibits the highest performance with a power density of 0.27 W/cm^2 at 800 ^{o}C. This indicates that even a small amount of Ag dispersed in the $Nd_{0.6}Sr_{0.4}Co_{0.5}Fe_{0.5}O_{3-\delta}$ cathode could enhance the cell performance significantly without major microstructural changes. Based on the AC impedance analysis (Figures 6.5 and 6.6), the reduction in the cathodic over-potential caused by Ag impregnation could be attributed possibly to the high catalytic activity of Ag rather than simply to the reduction in the ohmic resistance. It has been reported that nanosize Pt promotes surface reaction at the boundary between Pt and La(Sr)CoO_3.[113] Also, Wang *et al.*[118] have reported that Ag coating improves the oxygen exchange reaction in the $La_{0.6}Sr_{0.4}Co_{0.8}Fe_{0.2}O_3$-$Ce_{0.8}Gd_{0.2}O_{1.9}$-Ag cathode. Thus, the Ag catalyst presumably helps the surface exchange step (the dissociative adsorption of O_2 molecules to O_{ad} and/or the exchange reaction between the oxygen atoms (O_{ad}) and oxide ion vacancies in the $Nd_{0.6}Sr_{0.4}Co_{0.5}Fe_{0.5}O_{3-\delta}$ lattice). Additionally, Ag can provide electrons readily through the cathode surface due to its high electronic conductivity. Therefore, with respect to surface exchange and charge transfer, the oxygen reduction reaction at the boundary of Air/Ag/$Nd_{0.6}Sr_{0.4}Co_{0.5}Fe_{0.5}O_{3-\delta}$ could be more effective than at the boundary of Air/$Nd_{0.6}Sr_{0.4}Co_{0.5}Fe_{0.5}O_{3-\delta}$, and consequently the electrochemical performance is enhanced by the impregnation of Ag catalyst.

6.4 CONCLUSIONS

The $Nd_{0.6}Sr_{0.4}Co_{0.5}Fe_{0.5}O_{3-\delta}$-Ag composite cathodes containing ~ 0.5 wt. % impregnated Ag exhibit higher catalytic activity for the oxygen reduction reaction in intermediate temperature SOFC compared to the $Nd_{0.6}Sr_{0.4}Co_{0.5}Fe_{0.5}O_{3-\delta}$ cathode due to the increased electronic conductivity and electrocatalytic activity contributed by Ag. The incorporation of Ag into porous $Nd_{0.6}Sr_{0.4}Co_{0.5}Fe_{0.5}O_{3-\delta}$ offers the advantage of enhancing the catalytic activity while keeping the TEC low. The study demonstrates that cathodes prepared by impregnating the less expensive Ag may offer an attractive strategy to develop successful cathodes with a combination of low TEC and high electronic and ionic conductivities for intermediate temperature SOFC.

PART II

PEROVSKITE–RELATED INTERGROWTH OXIDE CATHODE MATERIALS FOR INTERMEDIATE TEMPERATURE SOFC

CHAPTER 7

CHARACTERIZATION OF $LaSr_3Fe_{3-y}Co_yO_{10-\delta}$ ($0 \leq y \leq 1.5$) INTERGROWTH OXIDE CATHODE MATERIALS

7.1 INTRODUCTION

$ABO_{3-\delta}$ perovskite oxides are the most widely investigated mixed ionic-electronic conductors and cathodes for SOFC in the literature. More recently, perovskite-related intergrowth oxides[120-122] $A_{n+1}B_nO_{3n+1}$ (A = lanthanide or alkaline earth, B = transition metal, and n = 1, 2, and 3) belonging to the Ruddlesden-Popper series have drawn some attention as mixed conductors.[120-125] These intergrowth oxides have structures in which the $(AO)_2$ double rock-salt layers alternate with the $A_{n-1}B_nO_{3n-1}$ perovskite layers along the *c* axis, giving a two-dimensional structure.[126] Figure 7.1 compares the typical crystal structures of the intergrowth oxides $Sr_{3-x}La_xFe_{2-y}Co_yO_{7-\delta}$ (n = 2) and $Sr_{4-x}La_xFe_{3-y}Co_yO_{10-\delta}$ (n = 3) with that of the perovskite oxide $La_{1-x}Sr_xCoO_{3-\delta}$ (n = ∞).

It has been reported that the intergrowth oxides $Sr_{3-x}La_xFe_{2-y}Co_yO_{7-\delta}$ with $0 \leq x \leq 0.3$ and $0 \leq y \leq 1.0$ (n = 2 member) and $LaSr_3Fe_{3-y}Co_yO_{10-\delta}$ with $0 \leq y \leq 1.5$ (n = 3 member) exhibit good mixed ionic-electronic conduction with adequate oxide ion and electronic conductivities and are attractive as oxygen separation membranes.[122-125] More importantly, these oxides exhibit excellent structural stability with no crystallographic phase transformations up to 900 °C even under low pO_2 conditions,

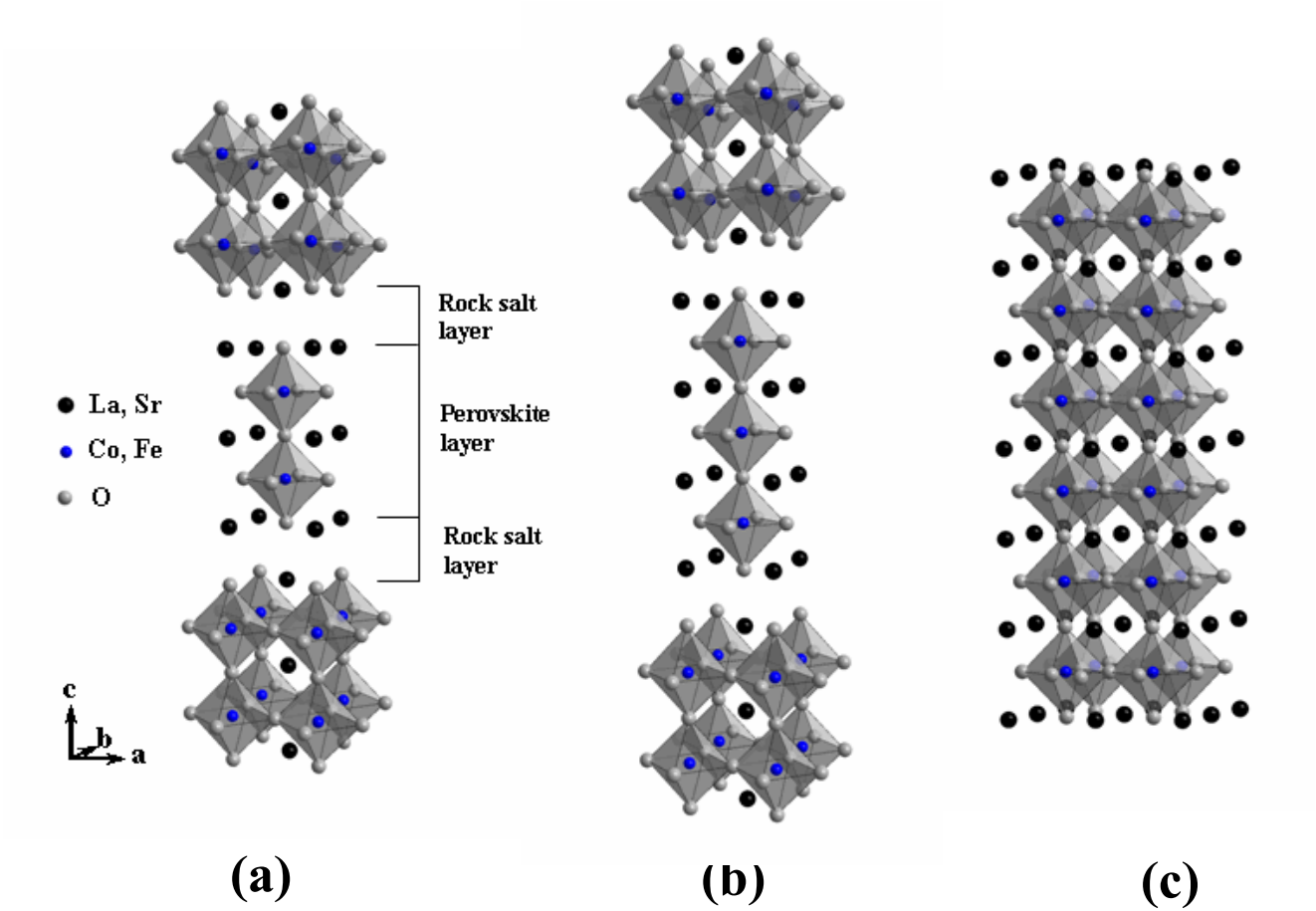

Figure 7.1 Crystal structures of (a) $Sr_{3-x}La_xFe_{2-y}Co_yO_{7-\delta}$ (n = 2), (b) $Sr_{4-x}La_xFe_{3-y}Co_yO_{10-\delta}$ (n = 3), and (c) $La_{1-x}Sr_xCoO_{3-\delta}$ (n = ∞).

unlike most of the Co- and Fe-containing $ABO_{3-\delta}$ perovskite oxides, suggesting good long-term stability for the intergrowth oxides.

However, the $A_{n+1}B_nO_{3n+1}$ intergrowth oxides have not been explored as cathodes for SOFC, excepting the n = 1 member $La_2NiO_{4+\delta}$[120,121] that contains δ excess oxide ions located at the tetrahedral interstitial sites of the $(LaO)_2$ double rock-salt layers. $La_2NiO_{4+\delta}$ exhibits rather low electronic conductivity due to the $Ni^{2+/3+}$ couple. In contrast, the n = 2 and 3 members with the $Fe^{3+/4+}$ and Co^{3+4+} couples offer much higher electronic conductivity due to an increased O-B-O interaction along the *c* axis and a smaller charge transfer gap between the $Fe^{3+/4+}$:3d or Co^{3+4+}:3d band and the O^{2-}:2p band.[122-125] With this perspective, this chapter presents the characterization of $LaSr_3Fe_{3-y}Co_yO_{10-\delta}$ with $0 \leq y \leq 1.5$ (n = 3 member) as cathode materials for intermediate temperature SOFC. The effect of Co content on the electrical conductivity, thermal expansion, chemical compatibility, and electrochemical performance is presented. The effect of $Ce_{0.9}Gd_{0.1}O_{1.95}$ (GDC) interlayer in preventing undesirable reactions between the cathode and the electrolyte is also discussed.

7.2 EXPERIMENTAL

7.2.1 Materials Synthesis

The $LaSr_3Fe_{3-y}Co_yO_{10-\delta}$ ($0 \leq y \leq 1.5$) samples were synthesized by solid-state reaction. Required amounts of La_2O_3, $SrCO_3$, Fe_2O_3, and Co_3O_4 were first calcined at

1000 ^{o}C for 12 h, ground, and finally fired at 1400 ^{o}C for 24 h. The LSGM electrolyte disks and the NiO-$Ce_{0.9}Gd_{0.1}O_{1.95}$ (GDC) cermet (Ni:GDC = 70:30 vol %) anode powder were synthesized by solid-state reaction and glycine-nitrate combustion method, respectively, as described in Chapter 2.

7.2.2 Fabrication of Single Cells

The $LaSr_3Fe_{3-y}Co_yO_{10-\delta}$ cathodes were prepared by screen printing onto a 0.7 mm thick LSGM electrolyte pellet, followed by firing at 950 ^{o}C for 3 h. For the $LaSr_3Fe_{3-y}Co_yO_{10-\delta}$ cathodes with the GDC interlayer, both the cathode and interlayer were first prepared by screen printing and then co-fired at 1100 ^{o}C for 3 h. For a comparison, the electrochemical performance was also evaluated with the $La_{0.6}Sr_{0.4}CoO_{3-\delta}$ (LSC) perovskite cathode that was synthesized by a solid-state reaction at 1200 ^{o}C for 24 h and fired after screen printing at 1000 ^{o}C for 3 h. The NiO-GDC cermet anode was also prepared by screen printing, followed by firing at 1200 ^{o}C for 3 h.

7.2.3 Characterization

The samples were characterized by electrical conductivity, TMA, AC impedance analysis, and single cell measurement as described in Chapter 2. The reactivity tests were carried out at various temperatures for 3 h in air.

7.3 RESULTS AND DISCUSSION

7.3.1 Electrical Conductivity

The temperature dependence of the electrical conductivity of the $LaSr_3Fe_{3-y}Co_yO_{10-\delta}$ samples is shown in Figure 7.2. All the samples exhibit a semiconducting behavior at lower temperatures (< 400 ^oC), with the conductivity increasing with increasing temperature. However, the conductivity decreases with increasing temperature above a transition temperature T_t of about 300-500 ^oC due to a significant loss of oxygen from the lattice as indicated by the TGA data.[124] The formation of oxide ion vacancies accompanied by a reduction of Fe^{4+} to Fe^{3+} or Co^{4+} to Co^{3+} at higher temperatures causes a decrease in the charge carrier concentration and covalent interaction due to a perturbation of the O-(Fe,Co)-O periodic potential,[66] resulting in a decrease in conductivity. The transition temperature T_t decreases slightly with increasing Co content y due to a lowering of the temperature at which oxygen loss begins to occur in air with increasing Co content.[124] At a given temperature, the electrical conductivity increases monotonically with increasing Co content due to an increase in the covalency of the (Co-Fe)-O bond. Matsumoto *et al.*[127] and Dasgupta *et al.*[128] have also reported a similar trend, respectively, for the perovskite systems $La_{1-x}Sr_xFe_{1-y}Co_yO_3$ and $Nd_{0.7}Sr_{0.3}Fe_{1-x}Co_xO_3$.

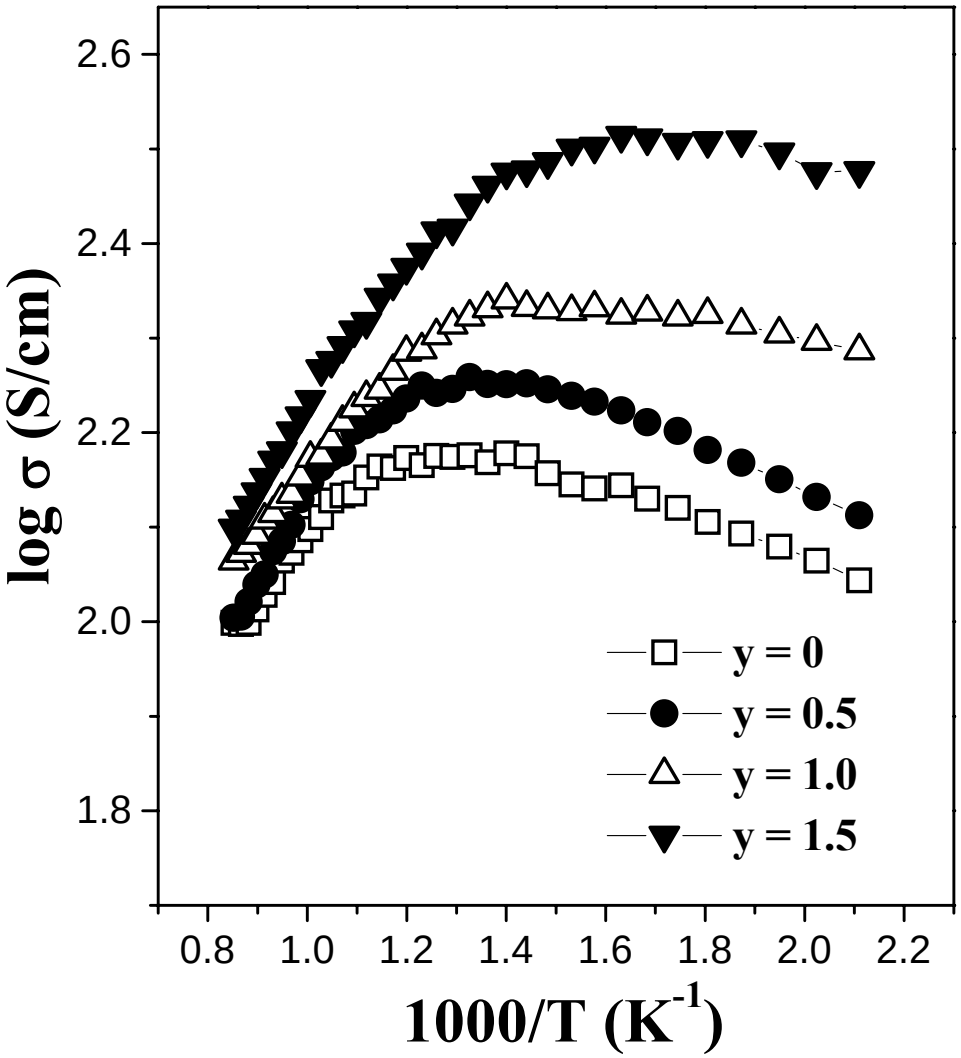

Figure 7.2 Variations of the electrical conductivity of $LaSr_3Fe_{3-y}Co_yO_{10-\delta}$ ($0 \leq y \leq 1.5$) with temperature in air.

7.3.2 Thermal Expansion Behavior

The thermal expansion behaviors of the $LaSr_3Fe_{3-y}Co_yO_{10-\delta}$ samples at 50-700 ^oC in air are shown in Figure 7.3a. The non-linear thermal expansion curve could be fitted with a forth polynomial regression[89] and the average TEC values obtained with the fitting are plotted as a function of Co content in Figure 7.3b. The TEC value increases with increasing Co content. The Co^{3+} ions are known to experience a low spin ($t_{2g}^6 e_g^0$) to high spin ($t_{2g}^4 e_g^2$) transition as the temperature increases.[91,129] Considering the larger ionic radius of the high spin Co^{3+} ion (r = 0.61 Å) compared to that of the low spin Co^{3+} ion (r = 0.545 Å), the spin state transition leads to a larger TEC for the Co-based perovskite systems.[72,75] Therefore, the spin state transitions associated with the Co^{3+} ions within the perovskite blocks of the present intergrowth oxide system could contribute to the increase in TEC with Co doping. TEC can also increase with increasing oxide ion vacancies due to a reduction in the electrostatic attractive forces between the cations and anions[94,95] and a reduction of the smaller Fe^{4+} or Co^{4+} to larger Fe^{3+} or Co^{3+} ions. Since the degree of oxygen loss increases with Co content in $LaSr_3Fe_{3-y}Co_yO_{10-\delta}$,[124] it could also contribute to the increase in TEC with Co content. The temperature at which the expansion curve deviates from linearity decreases slightly with increasing Co content, which attests to the influence of the formation of oxide ion vacancies on the lattice expansion. Furthermore, TEC is inversely proportional to the bonding energy between the ions in the lattice.[73]

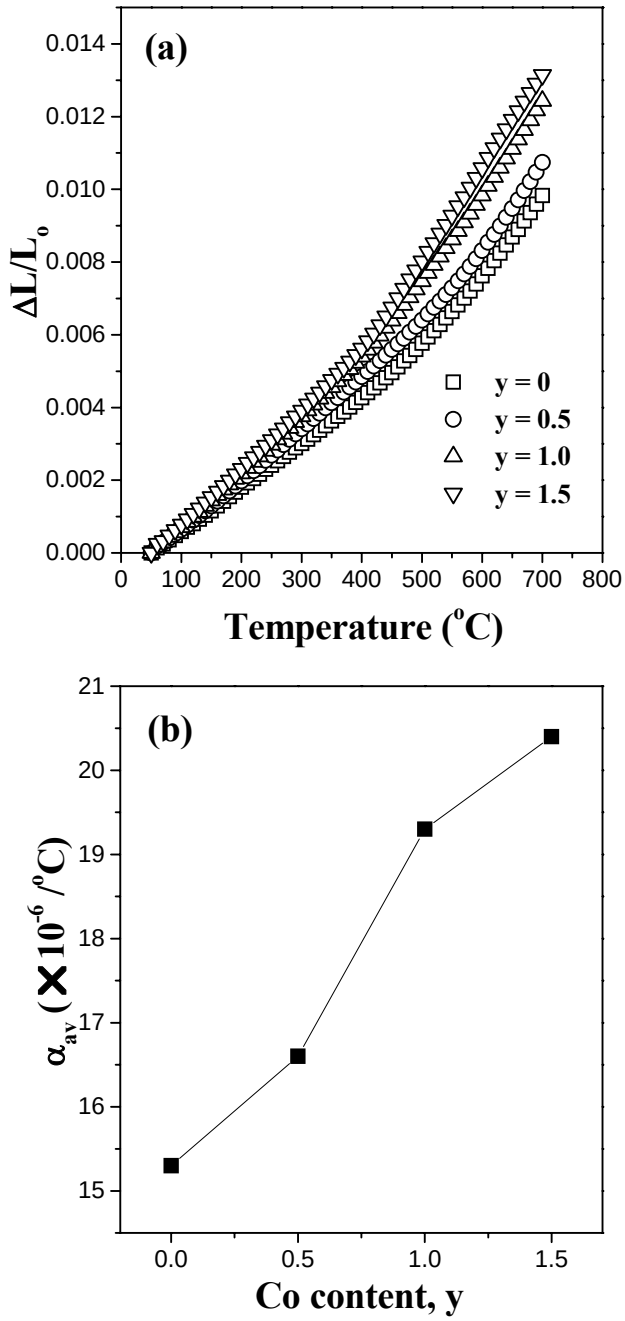

Figure 7.3 Thermal expansion behaviors of $LaSr_3Fe_{3-y}Co_yO_{10-\delta}$ ($0 \le y \le 1.5$) in air: (a) thermal expansion ($\Delta L/L_o$) curves with temperature and (b) average thermal expansion coefficients (α_{av}) with Co content y in the temperature range of 50-700 ^oC.

A lower standard Gibbs free energy of formation for Co_3O_4 (-794.871 kJ/mol) compared to that for Fe_3O_4 (-1017.438 kJ/mol)[130] implies that the Co-O bond is weaker than the Fe-O bond. Thus, the decrease in bonding energy with Co doping could also cause an increase in TEC.

7.3.3 Reactivity and Microstructure

One issue with the perovskite-related intergrowth oxide cathodes is the interfacial reaction with the yttria-stabilized zirconia (YSZ) or the LSGM electrolytes. The $LaSr_3Fe_{3-y}Co_yO_{10-\delta}$ samples react with LSGM at 1000 ^oC and form undesired reaction products. This reaction problem could be overcome by adopting an interlayer between the cathode and the electrolyte, and there is some knowledge of the CeO_2-based interlayers on the YSZ electrolyte.[131-134] The interlayer or the buffer layer should not react with both the cathode and the electrolyte, and should have high oxide ion conductivity in order to enhance the oxide ion diffusion. Figure 7.4 shows the X-ray diffraction patterns of the $LaSr_3Fe_{1.5}Co_{1.5}O_{10-\delta}$ and GDC ($Ce_{0.9}Gd_{0.1}O_{1.95}$) mixtures after heat treatment at various temperatures. While the samples fired at 1000 and 1100 ^oC show no interfacial reaction, reflections corresponding to unknown reaction products are found on firing at 1200 ^oC. The compositions with lower Co contents also do not react with GDC at 1100 ^oC (Figure 7.5). This indicates that the intergrowth oxide cathodes could be fired at least at 1100 ^oC to get good adhesion without the undesired interfacial reaction. Similarly, no reaction product was detected

after firing GDC and LSGM at 1200 ^{o}C for 3h. However, although X-ray diffraction does not indicate the formation of new phases, diffusion of ionic species across the interface between different phases could not be completely ruled out.

The firing temperature of the cathode could also affect the microstructure and consequently the electrochemical performance. Figure 7.6 shows the typical SEM micrographs of the cross-section of the porous $LaSr_3Fe_{1.5}Co_{1.5}O_{10-\delta}$ cathodes without and with the GDC interlayer on the LSGM electrolyte after firing, respectively, at 950 and 1100 ^{o}C for 3 h. Without the GDC interlayer, the $LaSr_3Fe_{1.5}Co_{1.5}O_{10-\delta}$ cathode should be fired below 1000 ^{o}C in order to avoid the interfacial reaction. As seen in Figure 7.6, the $LaSr_3Fe_{1.5}Co_{1.5}O_{10-\delta}$ cathode without the GDC interlayer fired at 950 ^{o}C has only point contacts between particles and poor adhesion between the cathode and electrolyte due to low firing temperature. On the other hand, the $LaSr_3Fe_{1.5}Co_{1.5}O_{10-\delta}$ cathode with the GDC interlayer fired at 1100 ^{o}C shows area contacts between particles and good adhesion between each layer. The smaller grain size of the GDC interlayer compared to that of the $LaSr_3Fe_{1.5}Co_{1.5}O_{10-\delta}$ layer is due to the poor sinterability of the GDC particles. In addition to preventing the interfacial reaction, the GDC layer should be sufficiently dense to maximize the oxide ion transport since it is an extension of the electrolyte as an oxide ion conductor. Therefore, further studies to improve the sinterability of the GDC interlayer could prove beneficial.

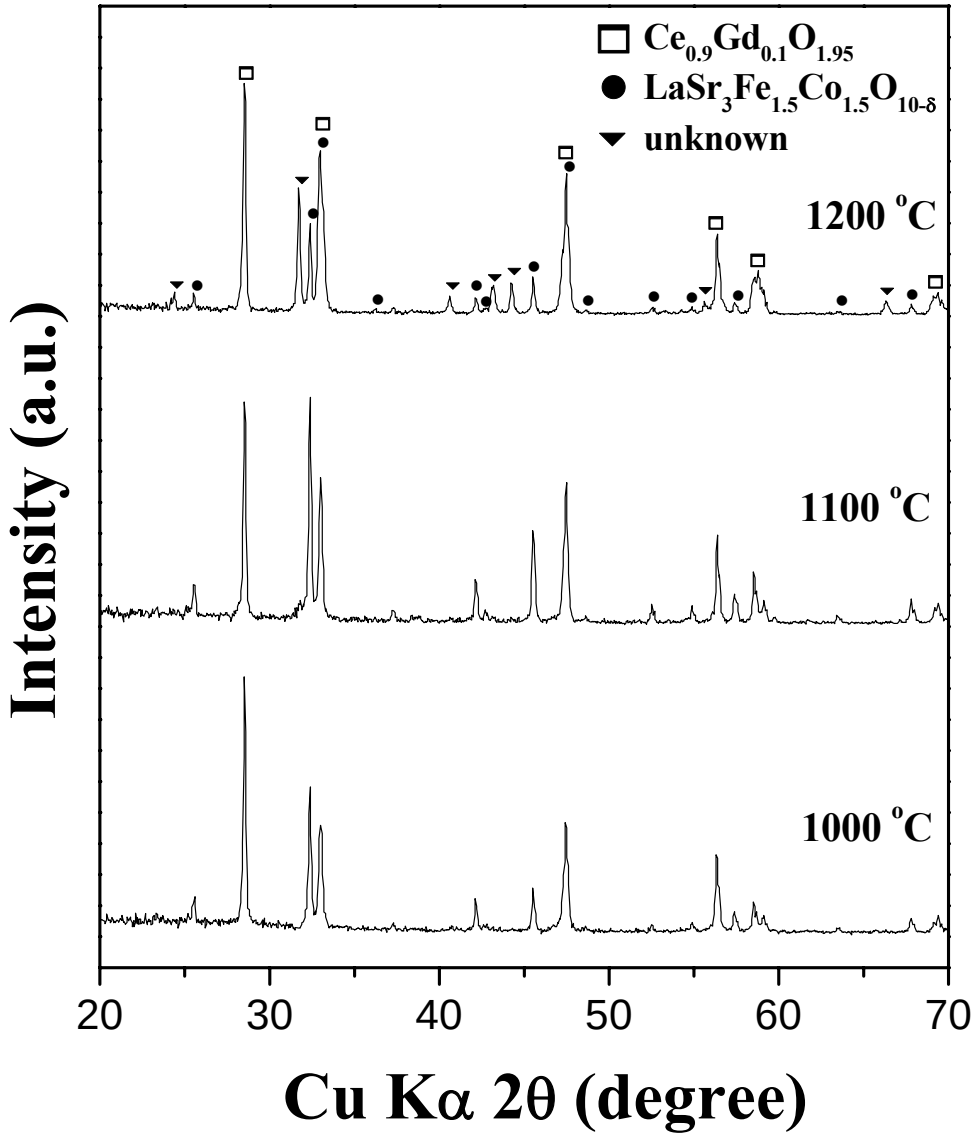

Figure 7.4 X-ray power diffraction patterns of $LaSr_3Fe_{1.5}Co_{1.5}O_{10-\delta}$ and GDC mixture after firing at various temperatures for 3 h in air.

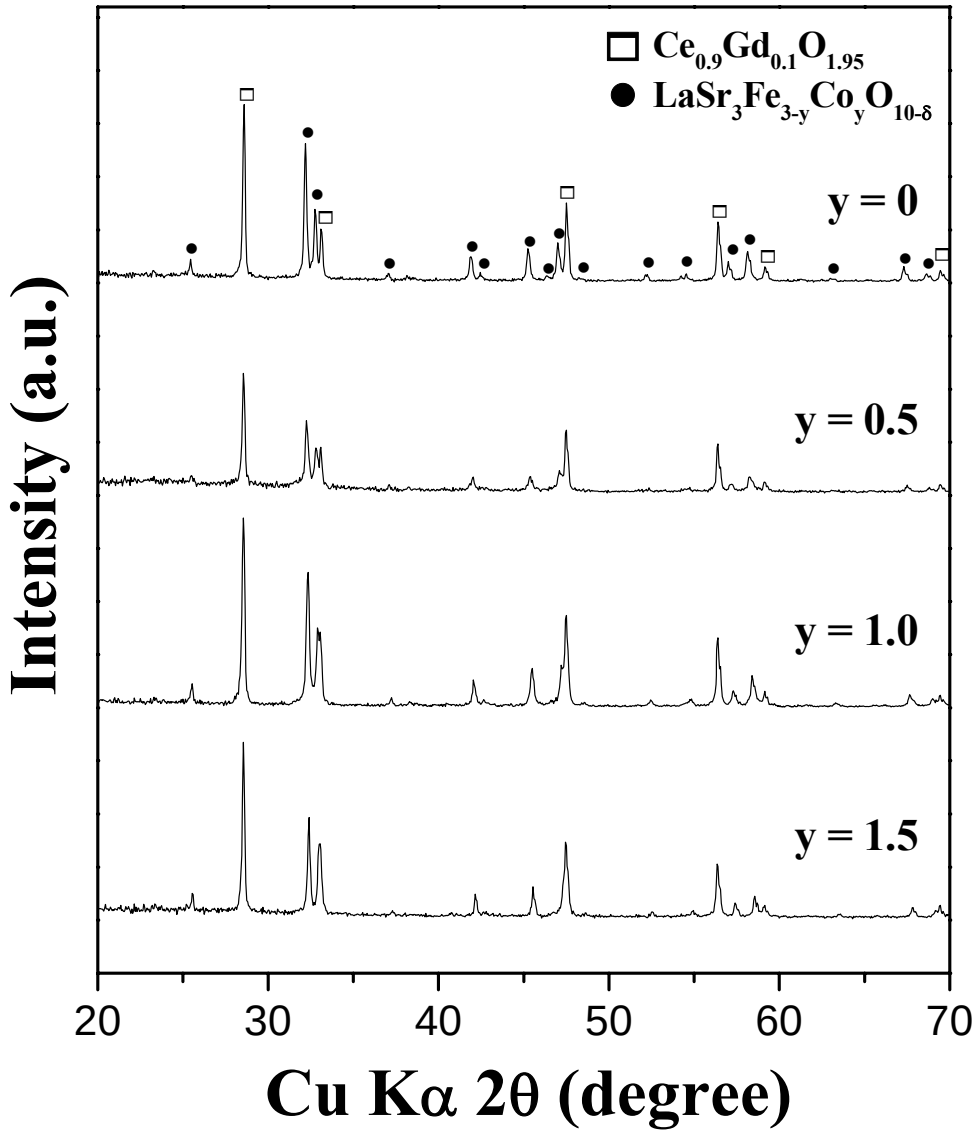

Figure 7.5 X-ray power diffraction patterns of $LaSr_3Fe_{3-y}Co_yO_{10-\delta}$ ($0 \le y \le 1.5$) and GDC mixture after firing at 1100 ^oC for 3 h in air.

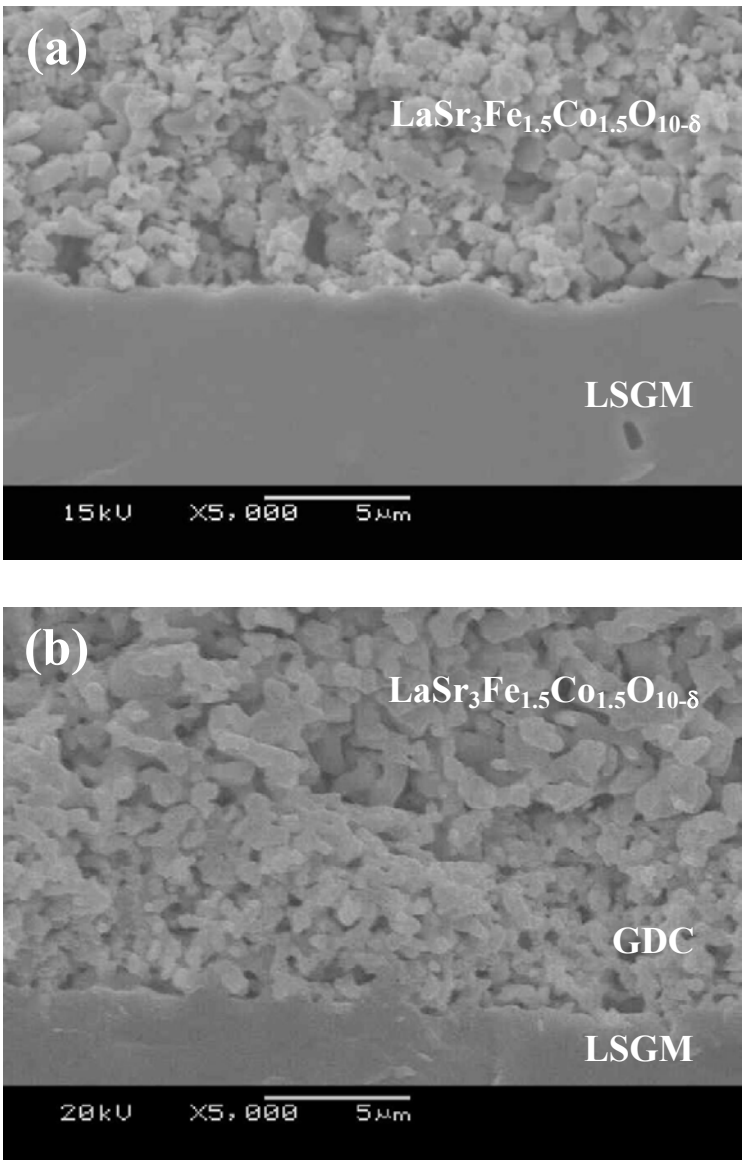

Figure 7.6 SEM micrographs of the $LaSr_3Fe_{1.5}Co_{1.5}O_{10-\delta}$ cathodes that were prepared (a) without and (b) with the GDC interlayer by firing, respectively, at 950 and 1100 ^{o}C for 3 h.

7.3.4 Electrochemical Performance

The electrochemical performances of the $LaSr_3Fe_{3-y}Co_yO_{10-\delta}$ cathodes were evaluated with an electrolyte-supported single cell fabricated with the LSGM electrolyte and GDC-Ni (30:70 vol %) anode. Figure 7.7 compares the I-V curves, power density, and the over-potential of the $LaSr_3Fe_{1.5}Co_{1.5}O_{10-\delta}$ cathodes with and without the GDC interlayer at 800 ^oC. The $LaSr_3Fe_{1.5}Co_{1.5}O_{10-\delta}$ cathode with the GDC interlayer exhibits a lower over-potential and a higher maximum power density than that without the GDC interlayer. This indicates that the $LaSr_3Fe_{1.5}Co_{1.5}O_{10-\delta}$ cathode with the GDC interlayer exhibits good catalytic activity and the GDC interlayer does not sacrifice the catalytic activity.

The AC impedance spectra of the $LaSr_3Fe_{1.5}Co_{1.5}O_{10-\delta}$ cathodes with and without the GDC interlayer at various temperatures in air are shown in Figure 7.8. At all temperatures, the $LaSr_3Fe_{1.5}Co_{1.5}O_{10-\delta}$ cathode with GDC interlayer shows lower total resistance R_{tot} (right intercept on Z_{re} axis) than that without the GDC interlayer. The temperature dependences of the ohmic resistance R_b (left intercept on Z_{re} axis) and polarization resistance R_p ($R_{tot} - R_b$) are shown in Figure 7.9. Although GDC has much higher resistivity than $LaSr_3Fe_{1.5}Co_{1.5}O_{10-\delta}$, the cathode with the GDC interlayer shows lower ohmic resistance than that without the GDC interlayer (Figure 7.9a).

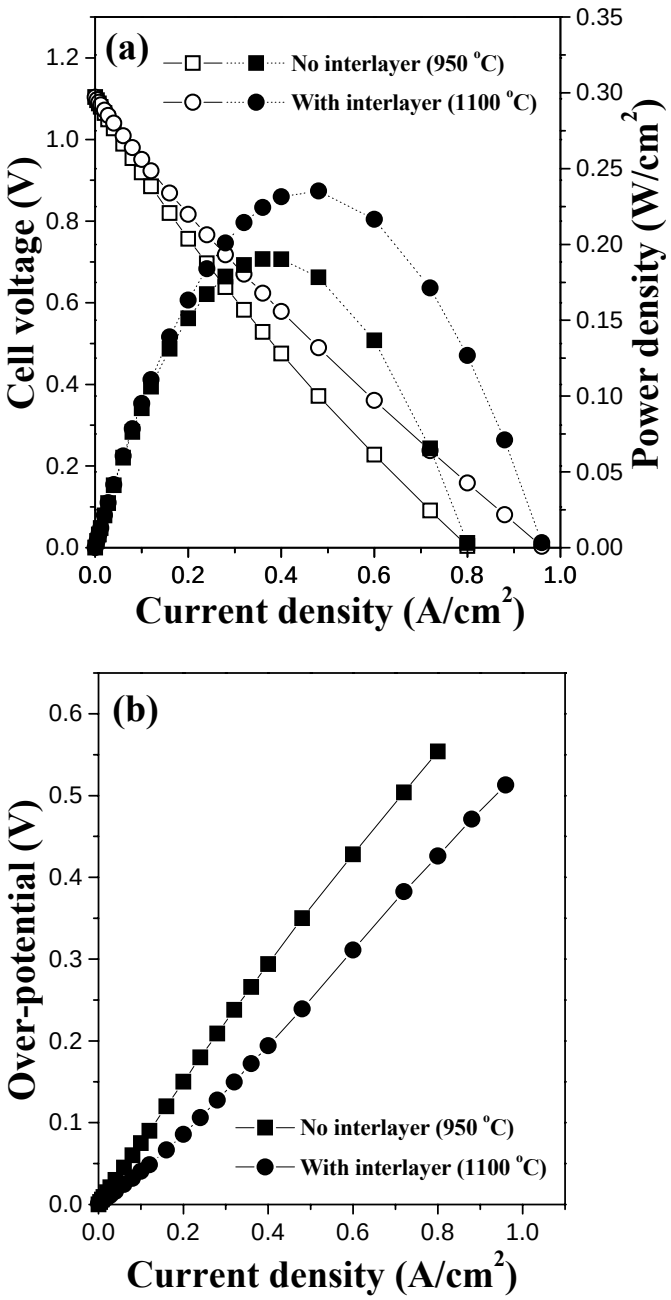

Figure 7.7 Comparison of (a) the I-V curves (open symbols) and power densities (closed symbols) and (b) cathode over-potentials of the $LaSr_3Fe_{1.5}Co_{1.5}O_{10-\delta}$ cathodes with and without the GDC interlayer at 800 °C. The temperatures in the legend refer to the co-firing temperatures.

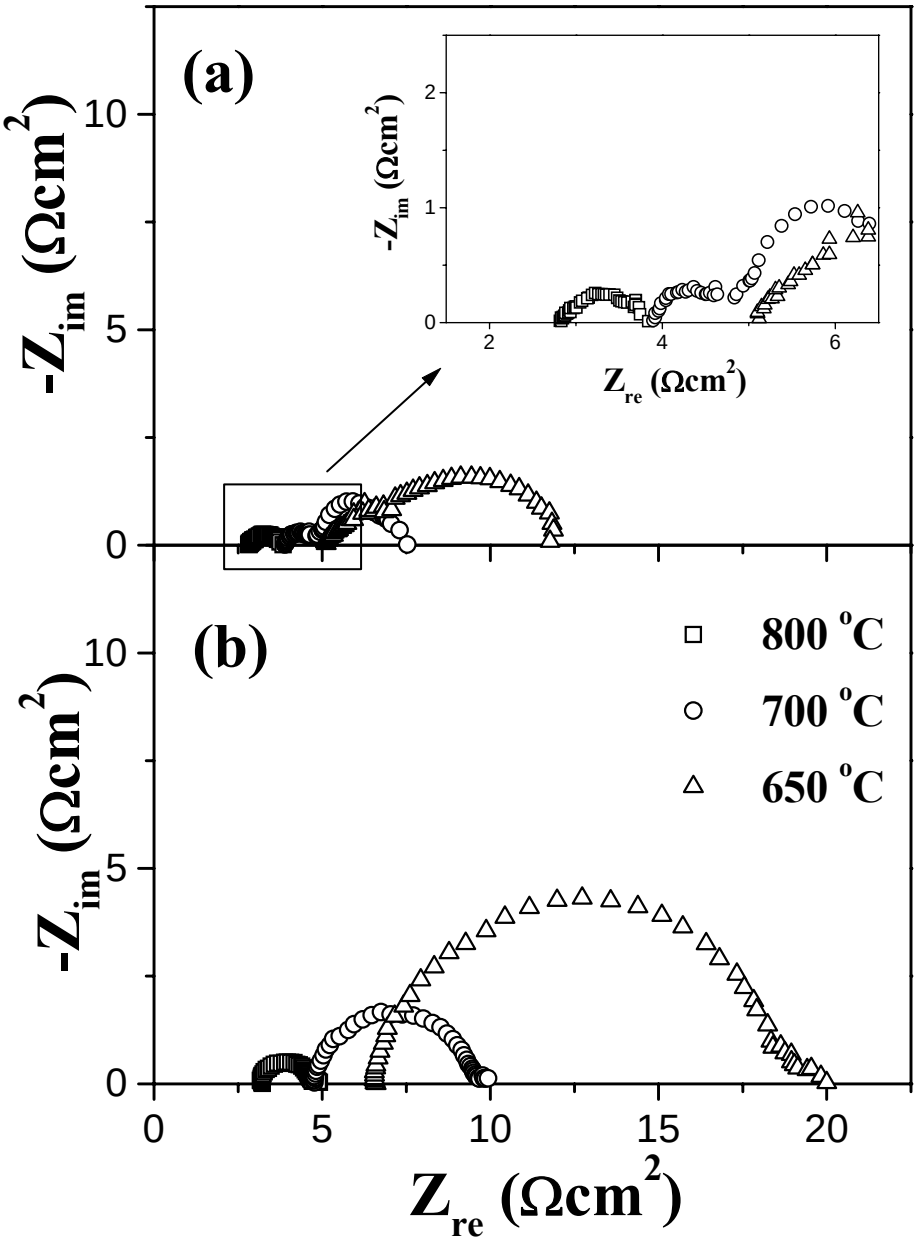

Figure 7.8 Typical AC impedance spectra of the $LaSr_3Fe_{1.5}Co_{1.5}O_{10-\delta}$ cathodes (a) with and (b) without the GDC interlayer at various temperatures in air. The inset in (a) shows an expansion of the high frequency region.

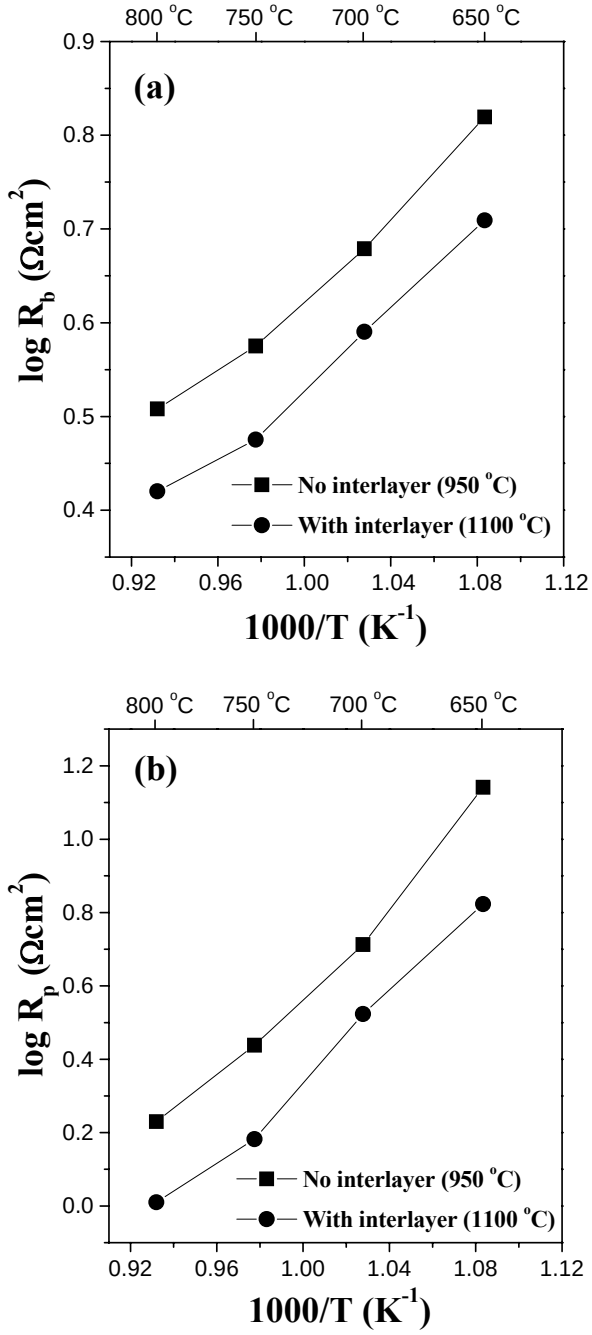

Figure 7.9 Temperature dependence of (a) ohmic (R_b) and (b) polarization (R_p) resistances of the $LaSr_3Fe_{1.5}Co_{1.5}O_{10-\delta}$ cathodes with and without the GDC interlayer. The results were derived from the AC impedance data. The temperatures in the legend refer to the co-firing temperatures.

As seen in Figure 7.6, the $LaSr_3Fe_{1.5}Co_{1.5}O_{10-\delta}$ cathode with the GDC interlayer fired at 1100 ^oC for 3 h has good area contact between particles with good adhesion between the cathode and electrolyte layers, which leads to lower contact and ohmic resistances. Large enough area contact and good adhesion can not only decrease the contact resistance but also improve the electron motion and oxide ion diffusion, resulting in decreased polarization resistance as shown in Figure 7.9b. It is possible that the GDC interlayer may also offer some catalytic activity for the oxygen reduction reaction as has been reported by others.[131-133,135] Thus, the better single cell performance of the $LaSr_3Fe_{1.5}Co_{1.5}O_{10-\delta}$ cathode with the GDC interlayer (Figure 7.7) is due to a reduction in not only the ohmic loss but also the polarization loss. However, the exact role of GDC interlayer on the oxygen reduction reaction is still not clear. Therefore, further studies to identify the mechanism of the oxygen reduction reaction within the GDC interlayer are needed.

The variations of the I-V curve, power density, and over-potential at 800 ^oC for the various $LaSr_3Fe_{3-y}Co_yO_{10-\delta}$ cathode compositions with the GDC interlayer are shown in Figure 7.10. For a comparison, the data for the perovskite $La_{0.6}Sr_{0.4}CoO_{3-\delta}$ (LSC) cathode with the GDC interlayer under similar experimental conditions are also shown in Figure 7.10. The power density increases and the over-potential decreases with increasing Co content for the intergrowth $LaSr_3Fe_{3-y}Co_yO_{10-\delta}$ cathodes. For all the compositions investigated, the electrochemical performance was found to be stable without any significant degradation during the test period.

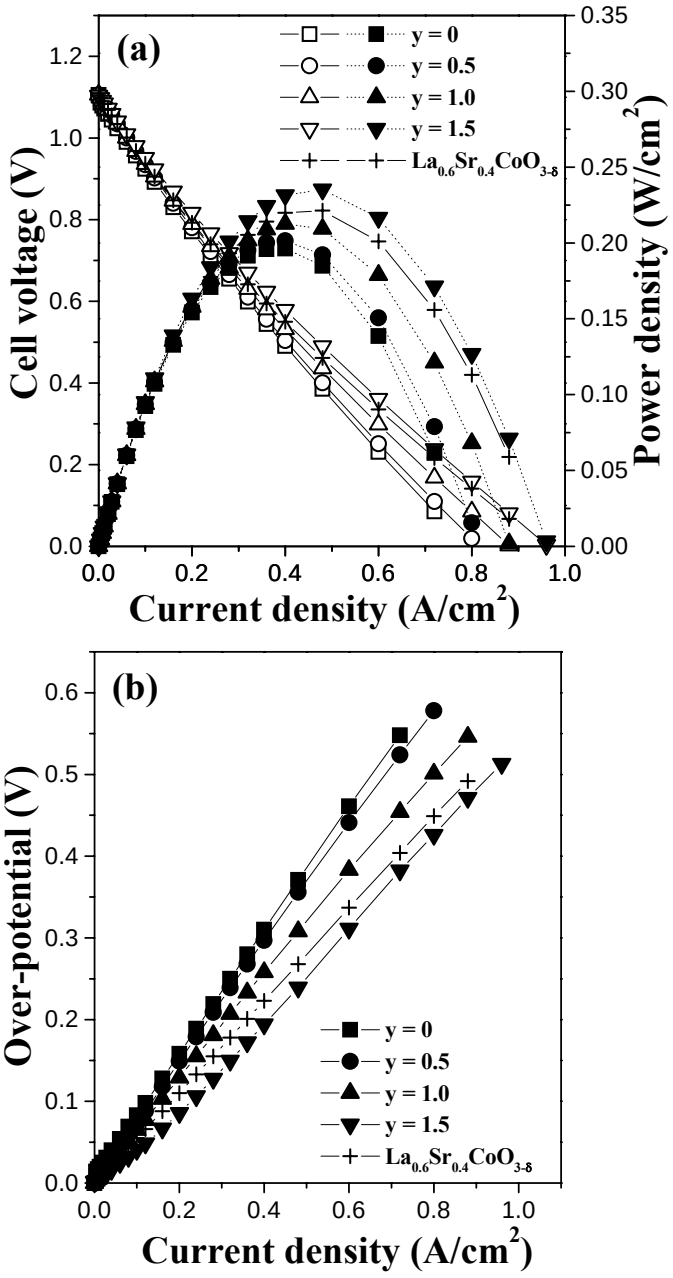

Figure 7.10 Comparison of (a) the I-V curves (open symbols) and power densities (closed symbols) and (b) cathode over-potentials of the intergrowth $LaSr_3Fe_{3-y}Co_yO_{10-\delta}$ ($0 \le y \le 1.5$) cathodes with the GDC interlayer (fired at 1100 ^oC for 3 h) at 800 ^oC. For a comparison, the data for the perovskite $La_{0.6}Sr_{0.4}CoO_{3-\delta}$ (fired at 1000 ^oC for 3 h) are also shown.

Since the oxygen reduction reaction is considered as a multiphase catalytic reaction, the oxide ion mobility and surface exchange (the adsorption/dissociation of oxygen molecule) as well as the electronic conductivity of the cathode material are critical to maximize the electrochemical performance. The electrical conductivity increases with increasing Co content (Figure 7.2), and the substitution of Co^{3+} for Fe^{3+} increases the concentration of the oxide ion vacancies as indicated by the TGA data.[124] The oxygen permeability, which is controlled by the transport or mobility of oxide ions, also increases with increasing Co content.[124] The surface oxygen exchange coefficient is directly proportional to the mobile fraction of the oxide ion vacancies.[136] Gao *et al.*[77] have also reported that high oxide ion vacancy concentration on the surface of the cathode material could improve the oxygen dissociation. Thus, an increase in the charge transfer kinetics, oxide ion mobility, and surface exchange resulting from a substitution of Co^{3+} for Fe^{3+} leads to an increase in the electrochemical performance. More importantly, the $LaSr_3Fe_{1.5}Co_{1.5}O_{10-\delta}$ cathodes with the GDC interlayer show slightly better electrochemical performance than the perovskite $La_{0.6}Sr_{0.4}CoO_{3-\delta}$ cathode. The lower TEC of the intergrowth $LaSr_3Fe_{3-y}Co_yO_{10-\delta}$ cathodes (15.2–20.4 $\times$ 10^{-6} $^oC^{-1}$) compared to that of the perovskite $La_{0.6}Sr_{0.4}CoO_{3-\delta}$ cathode (21.3 $\times$ 10^{-6} $^oC^{-1}$)[109] provides an added advantage with this new class of cathodes.

7.4 CONCLUSIONS

With an aim to develop new cathode materials for intermediate temperature SOFC, the mixed conducting $LaSr_3Fe_{3-y}Co_yO_{10-\delta}$ ($0 \leq y \leq 1.5$) oxides with a perovskite-related intergrowth structure have been investigated. The electrical conductivity of these intergrowth oxides are > 100 S/cm above 500 ^oC, which is acceptable to employ them as cathodes in SOFC, and the substitution of Co for Fe increases the conductivity due to an increase in the covalency of the (Fe,Co)-O bond. The TEC increases with increasing Co content due to the spin state transitions associated with the Co^{3+} ions and the formation of increasing degree of oxide ion vacancies. The porous GDC interlayer successfully prevents the unfavorable reaction between cathode and electrolyte, and the cathode with GDC interlayer exhibits good electrocatalytic activity. The electrochemical performance of the $LaSr_3Fe_{3-y}Co_yO_{10-\delta}$ cathodes with a GDC interlayer increases with increasing Co content due to an increase in the electrical conductivity and oxide ion conduction. While the electrochemical performance is comparable to that of the well-known perovskite $La_{0.6}Sr_{0.4}CoO_{3-\delta}$ cathode, this new class of $LaSr_3Fe_{3-y}Co_yO_{10-\delta}$ intergrowth cathodes offer an important advantage of significantly lower TEC compared to that of the $La_{0.6}Sr_{0.4}CoO_{3-\delta}$ perovskite. Additionally, the good structural stability of the intergrowth oxides without any phase transitions compared to the perovskite oxides may provide added benefits with respect to long-term stability.

CHAPTER 8

CHARACTERIZATION OF $Sr_{3-x}La_xFe_{2-y}Co_yO_{7-\delta}$ ($0.3 \leq x \leq 0.6$ AND $0 \leq y \leq 0.6$) INTERGROWTH OXIDE CATHODE MATERIALS

8.1 INTRODUCTION

In an effort to develop new cathode materials for intermediate temperature SOFC, the perovskite-related intergrowth oxides, which belong to the Ruddlesden-Popper (R-P) series[126] with the general formula $(La,Sr)_{n+1}(Fe,Co)_nO_{3n+1}$, have been considered. The crystal structures of the intergrowth oxides $Sr_{3-x}La_xFe_{2-y}Co_yO_{7-\delta}$ (n = 2) and $Sr_{4-x}La_xFe_{3-y}Co_yO_{10-\delta}$ (n = 3) with that of the perovskite oxide $La_{1-x}Sr_xCoO_{3-\delta}$ (n = ∞) have already been described in Chapter 7. While double and triple perovskite layers, respectively, alternate with double rock salt layers in $Sr_{3-x}La_xFe_{2-y}Co_yO_{7-\delta}$ (n = 2) and $Sr_{4-x}La_xFe_{3-y}Co_yO_{10-\delta}$ (n = 3), ∞ number of perovskite layers is stacked along the *c* axis in $La_{1-x}Sr_xCoO_{3-\delta}$ (n = ∞). Thus the (Fe,Co)-O interaction is two-dimensional in the former two systems (n = 2 and 3), while it is three-dimensional in the latter (n = ∞) system.

It has been previously reported that both the $Sr_{3-x}La_xFe_{2-y}Co_yO_{7-\delta}$ (n = 2), $LaSr_3Fe_{3-y}Co_yO_{10-\delta}$ (n = 3) systems exhibit high oxide ion and electronic conductivities with good structural stability over a range of oxygen partial pressures and are attractive as oxygen separation membranes.[122-125] As shown in Chapter 7, the

n = 3 member $LaSr_3Fe_{3-y}Co_yO_{10-\delta}$ exhibits high catalytic activity for the oxygen reduction reaction in intermediate temperature SOFC with a lower TEC than the $La_{1-x}Sr_xCoO_{3-\delta}$ perovskite oxides. This chapter explores the n = 2 member $Sr_{3-x}La_xFe_{2-y}Co_yO_{7-\delta}$ ($0.3 \leq x \leq 0.6$ and $0 \leq y \leq 0.6$) as a cathode material for intermediate temperature SOFC with a $Ce_{0.9}Gd_{0.1}O_{1.95}$ (GDC) interlayer between the cathode and the electrolyte to prevent chemical reaction. The effects of Co and La contents on oxygen content, TEC, electrical conductivity, and electrocatalytic activity are presented. Also, the properties and performance of the cathodes are compared with those of the $LaSr_3Fe_{3-y}Co_yO_{10-\delta}$ intergrowth and $La_{0.6}Sr_{0.4}CoO_{3-\delta}$ perovskite oxides.

8.2 EXPERIMENTAL

8.2.1 Materials Synthesis

The $Sr_{3-x}La_xFe_{2-y}Co_yO_{7-\delta}$ samples were prepared by calcining required amounts of $SrCO_3$, La_2O_3, Fe_2O_3, and Co_3O_4 in air at 900 ºC for 12 h, followed by grinding, pressing into pellets, and sintering in air at 1300 ºC for 24 h. The LSGM electrolyte disks and the NiO-$Ce_{0.9}Gd_{0.1}O_{1.95}$ (GDC) cermet (Ni:GDC = 70:30 vol %) anode powder were prepared by solid-state reaction and glycine-nitrate combustion method, respectively, as described in Chapter 2.

8.2.2 Fabrication of Single Cells

The anode and interlayer were fabricated with screen printing directly onto the 0.7 mm thick LSGM electrolyte pellet. The cathode was likewise fabricated with screen printing directly onto the interlayer. The screen printed anode, interlayer, and cathode were fired for 3 h, respectively, at 1200, 1100, and 1000 ºC.

8.2.3 Characterization

The $Sr_{3-x}La_xFe_{2-y}Co_yO_{7-\delta}$ samples were characterized by XRD, iodometric titration to determine the average oxidation state of transition metals and oxygen content, TGA, TMA, electrical conductivity, SEM, and electrochemical single cell measurements as described in Chapter 2. The reactivity of the cathode compositions with GDC or LSGM was assessed by heating the mixtures at 1000 and 1100 ºC for 3 h, followed by examining the product by XRD.

8.3 RESULTS AND DISCUSSION

8.3.1 Crystal Chemistry and Oxygen Content

The XRD patterns of the $Sr_{3-x}La_xFe_{2-y}Co_yO_{7-\delta}$ samples are shown in Figure 8.1. The data reveal that single phase products are formed for $0 \leq y \leq 0.6$ in $Sr_{2.7}La_{0.3}Fe_{2-y}Co_yO_{7-\delta}$ and for $Sr_{2.4}La_{0.6}Fe_{1.4}Co_{0.6}O_{7-\delta}$.[122,123] However, at higher La

contents of x = 1 as in $Sr_2LaFe_{1.4}Co_{0.6}O_{7-\delta}$, impurity phases are formed as seen in Figure 8.1.

The average oxidation state values of the transition metal ions and the oxygen contents determined by the iodometric titration are given in Table 8.1. With a given La content x, the oxygen content decreases with increasing Co content y due to a lower stability of Co^{4+} compared to Fe^{4+}.[122] With a given Co content y = 0.6, the oxygen content increases with the La content due to a replacement of lower valent Sr^{2+} by the higher valent La^{3+}. Figure 8.2 shows the variations of the oxygen content with temperature in air for various values of x and y. The oxygen content remains constant up to about 300 ºC, and then decreases with increasing temperature. With a given La content x = 0.3, the degree of oxygen loss with temperature increases with increasing Co content. This suggests a weaker binding of the oxide ions with increasing Co content, which is consistent with a lower standard Gibbs free energy of formation for Co_3O_4 (-794.871 kJ/mol) than that for Fe_3O_4 (-1017.438 kJ/mol) .[130] On the other hand, with a given Co content y = 0.6, the degree of oxygen loss decreases with increasing La content x. This indicates a stronger La^{3+}-O bond compared to the Sr^{2+}-O bond, which is in accordance with the higher bond enthalpy for LaO (799 kJ/mol) compared to that for SrO (426.3 kJ/mol)[137] and a much lower vapor pressure of LaO compared to that of SrO in the LSGM sample.[138]

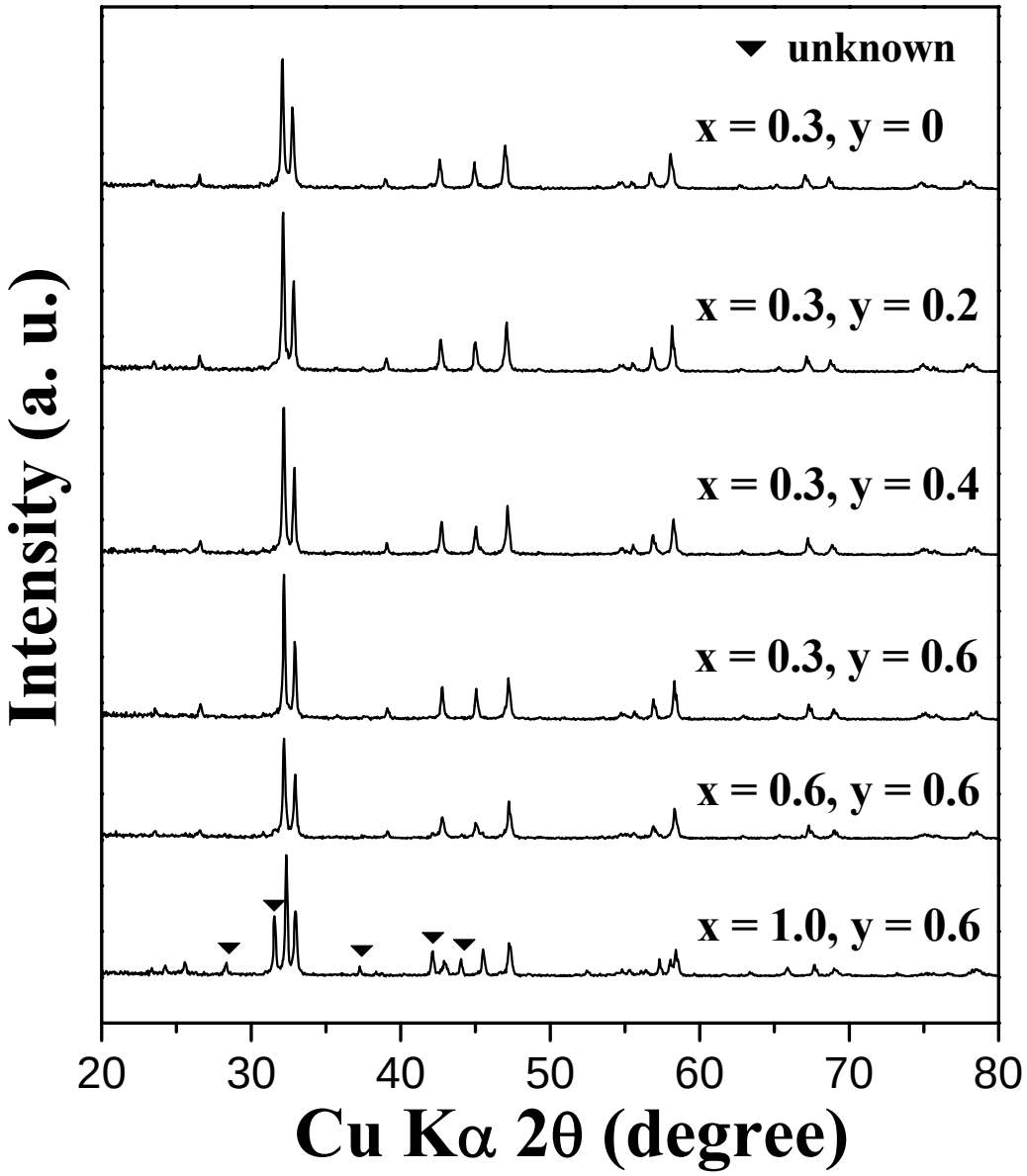

Figure 8.1 X-ray diffraction patterns of $Sr_{3-x}La_xFe_{2-y}Co_yO_{7-\delta}$ sintered at 1300 ^oC for 24 h.

Table 8.1 Oxygen content analysis data of $Sr_{3-x}La_xFe_{2-y}Co_yO_{7-\delta}$.

X	y	Oxidation state of Fe/Co	Oxygen content (7-δ)
0.3	0	3.75	6.90
	0.2	3.71	6.86
	0.4	3.67	6.82
	0.6	3.62	6.77
0.6	0.6	3.55	6.85

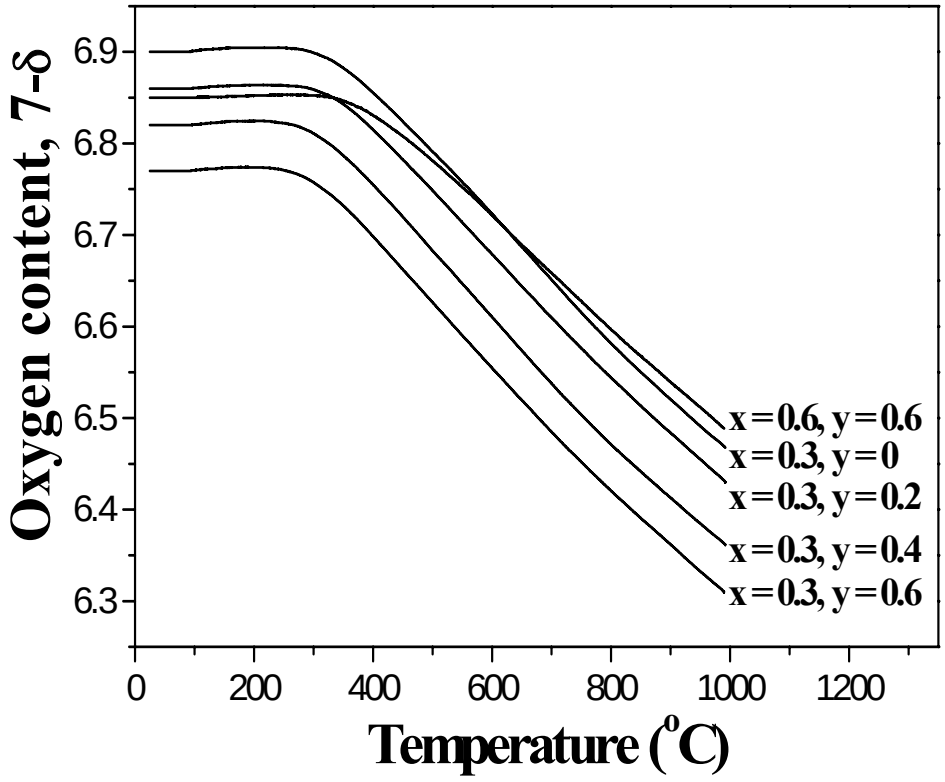

Figure 8.2 TGA plots of $Sr_{3-x}La_xFe_{2-y}Co_yO_{7-\delta}$ recorded in air with a heating rate of 2 °C/min.

8.3.2 Thermal Expansion Behavior

The thermal expansion behaviors of the $Sr_{3-x}La_xFe_{2-y}Co_yO_{7-\delta}$ samples are presented in Figure 8.3. With a given La content x = 0.3, the average TEC increases with increasing Co content due to a higher degree of oxide ion vacancies and the low spin to high spin transition associated with the Co^{3+} ion. TEC is inversely proportional to bond strength,[73] and a weakening of the electrostatic bond strength with increasing concentration of oxide ion vacancies causes an increase in TEC. High spin configurations have a larger ionic size than the low spin configurations, and the low spin to high spin Co^{3+} transition occurring with increasing temperature increases the TEC.[72,83] On the other hand, with a given Co content y = 0.6, TEC decreases with La content due to the replacement of the weaker, more ionic Sr^{2+}-O bond by a stronger, less ionic La^{3+}-O bond.

The $Sr_{3-x}La_xFe_{2-y}Co_yO_{7-\delta}$ system offers a modest improvement in TEC compared to the well-known $La_{1-x}Sr_xCoO_{3-\delta}$ perovskite system. The TEC values seen in Figure 8.3b are lower than that found, for example, with $La_{0.6}Sr_{0.4}CoO_{3-\delta}$ (21.3×10^{-6} ºC^{-1}).[109] However, the $Sr_{3-x}La_xFe_{2-y}Co_yO_{7-\delta}$ (n = 2) system has a slightly higher TEC ($17.4\text{-}21.1 \times 10^{-6}$ ºC^{-1}) compared to the $LaSr_3Fe_{3-y}Co_yO_{10-\delta}$ (n = 3) system ($15.2\text{-}20.4 \times 10^{-6}$ ºC^{-1}).[139] The difference in TEC among the three systems could be understood by considering the differences in the oxide ion vacancy concentration. While the $Sr_{3-x}La_xFe_{2-y}Co_yO_{7-\delta}$ (n = 2) system has $\delta \approx 0.4 - 0.6$ in air at high temperatures (800-900 ^{o}C), which corresponds to 5.7 – 8.6 % vacancies in the oxide

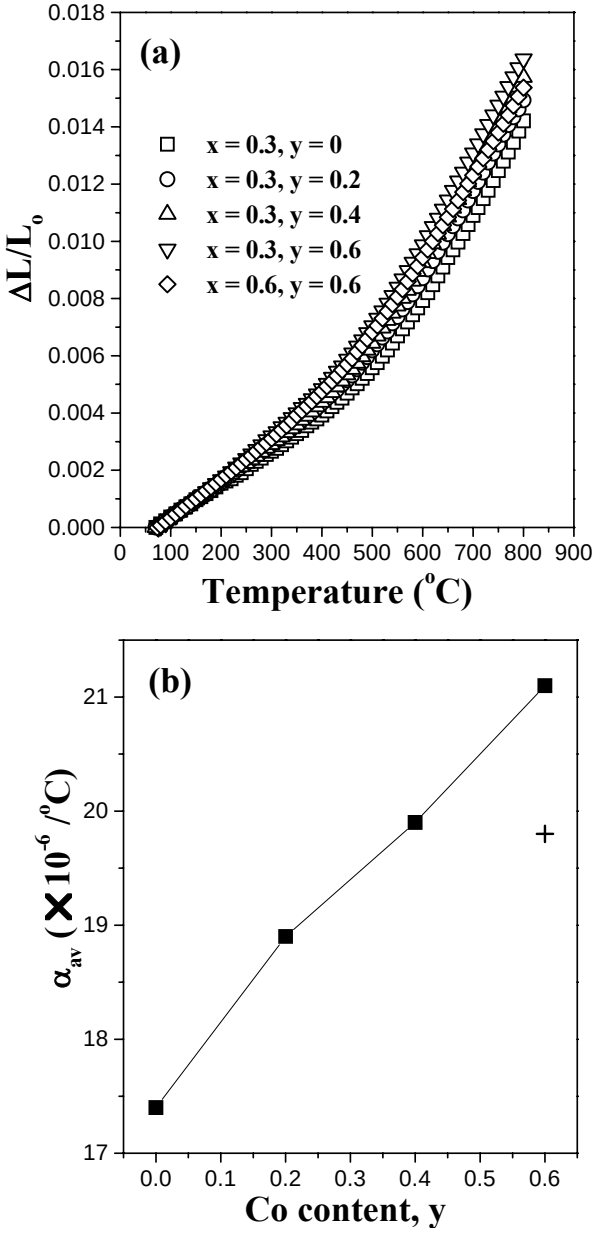

Figure 8.3 Thermal expansion behaviors of $Sr_{3-x}La_xFe_{2-y}Co_yO_{7-\delta}$ in air: (a) thermal expansion ($\Delta L/L_o$) curves as a function of temperature and (b) variation of average thermal expansion coefficients (α_{Av}) with Co content y in the temperature range of 50-800 ^oC: x = 0.3 (■) and x = 0.6 (+).

ion sites, the $LaSr_3Fe_{3-y}Co_yO_{10-\delta}$ (n = 3) system has $\delta \approx 0.3 - 0.45$ (3 – 4.5 % vacancies in the oxide ion sites)[124] under the same conditions. A larger % of oxide ion vacancies in the $Sr_{3-x}La_xFe_{2-y}Co_yO_{7-\delta}$ system leads to a higher TEC. On the other hand, the largest TEC value of $La_{0.6}Sr_{0.4}CoO_{3-\delta}$ (n = ∞) is due to both a large % of oxide ion vacancies (6 % with $\delta \approx 0.18$)[25] and 100 % Co (without any Fe) that may undergo low spin to high spin transition.

8.3.3 Electrical Conductivity

The temperature dependence of electrical conductivity of the $Sr_{3-x}La_xFe_{2-y}Co_yO_{7-\delta}$ samples is plotted in Figure 8.4. The conductivity from 100-400 ºC was found to increase with increasing temperature, indicating a semiconducting behavior. After reaching a maximum around 400 ºC, the conductivity value decreases with further increase in temperature, which could be attributed to the oxygen loss from the lattice as indicated by the TGA data in Figure 8.2 and the subsequent decrease in the carrier concentration and (Fe,Co)-O covalency.[58,66,140] At a given temperature, the conductivity value increases with increasing Co and La contents. The increase in conductivity with the Co content at a given La content is due to an increase in the covalency of the O-(Fe,Co)-O bonds, resulting from a smaller charge transfer gap between the $Co^{3+/4+}$:3d and O^{2-}:2p bands compared to that between the $Fe^{3+/4+}$:3d and O^{2-}:2p bands.[141,142]

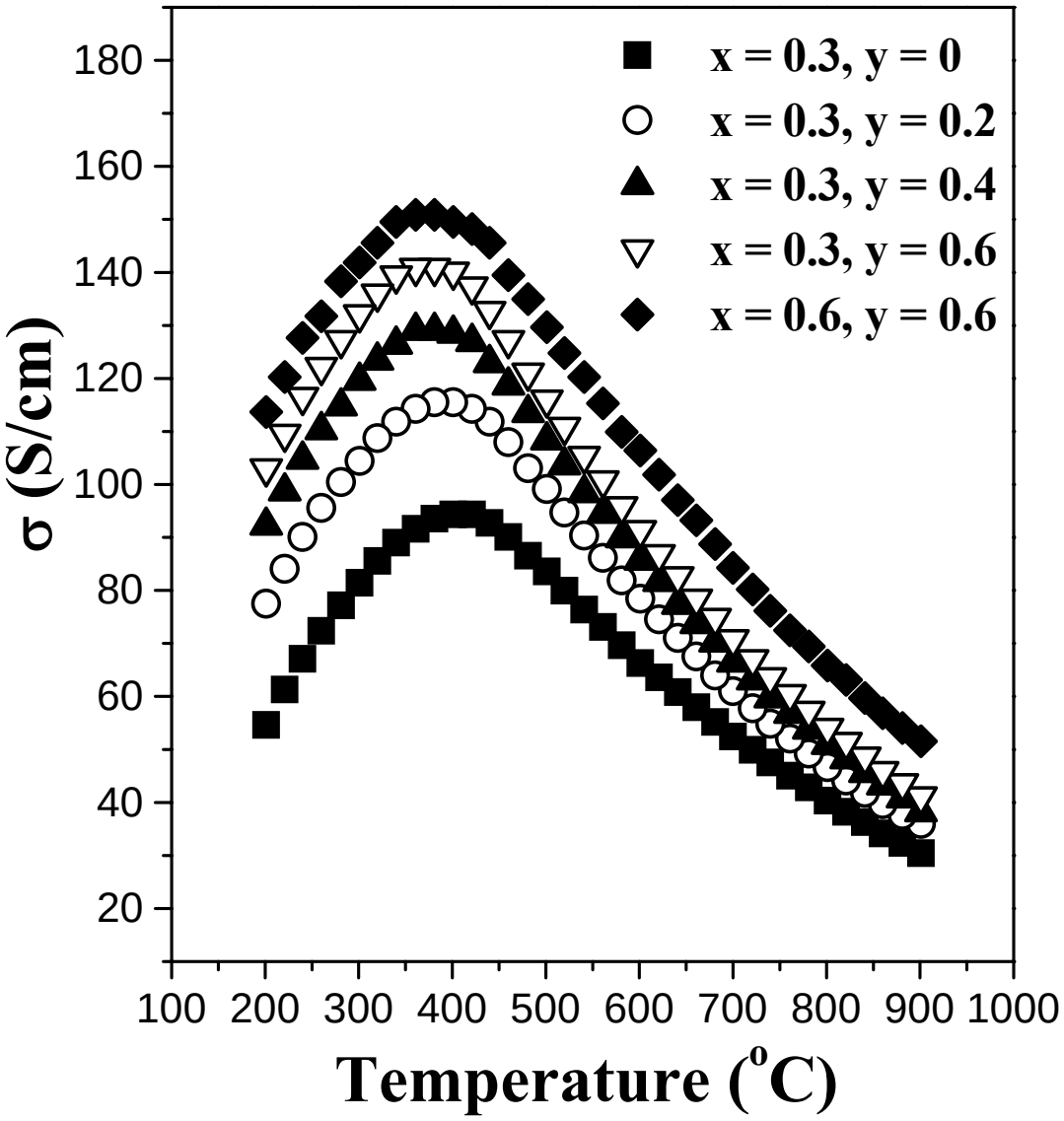

Figure 8.4 Variations of the electrical conductivity measured in air of $Sr_{3-x}La_xFe_{2-y}Co_yO_{7-\delta}$ with temperature.

On the other hand, the increase in conductivity with an increasing La content at a given Co content is due to a decrease in the concentration of oxide-ion vacancies and a consequent decrease in the perturbation of the O-(Fe,Co)-O extended interaction, resulting in an improvement in electron delocalization.[143]

The electrical conductivities of the $Sr_{3-x}La_xFe_{2-y}Co_yO_{7-\delta}$ system (30–150 S/cm) are significantly lower than that of the $La_{0.6}Sr_{0.4}CoO_{3-\delta}$ perovskite (~1200 S/cm).[109] The lower conductivity could be due to the discontinuity of the O-(Fe,Co)-O interaction along the *c* axis (two-dimensional) in the former compared to the three-dimensional interaction in the latter, and a consequent decrease in the bandwidth *W*. This explanation is supported by the fact that the $LaSr_3Fe_{3-y}Co_yO_{10-\delta}$ (n = 3) system, which has three SrO-(Fe,Co)O_2-SrO perovskite blocks along the *c* axis, exhibits slightly higher conductivity (~ 320 S/cm)[139] than the $Sr_{3-x}La_xFe_{2-y}Co_yO_{7-\delta}$ (n = 2) system that has only two SrO-(Fe,Co)O_2-SrO perovskite blocks along the *c* axis, as shown in Chapter 7.

8.3.4 Reactivity and Microstructure

Chemical reactivity tests carried out by firing the $Sr_{3-x}La_xFe_{2-y}Co_yO_{7-\delta}$ cathode powder with the LSGM electrolyte or the GDC interlayer powders followed by XRD analysis indicate that the $Sr_{3-x}La_xFe_{2-y}Co_yO_{7-\delta}$ cathode reacts with LSGM at 1000 ºC and GDC at 1100 ºC. The reactivity between LSGM and the $Sr_{3-x}La_xFe_{2-y}Co_yO_{7-\delta}$ system at temperatures below the preferred sintering temperature necessitates the use

of an interlayer. Figure 8.5 compares the XRD patterns recorded after heating the mixtures consisting of the $Sr_{3-x}La_xFe_{2-y}Co_yO_{7-\delta}$ cathode and GDC at 1000 ºC. The absence of any new reflections corresponding to reaction products suggest that GDC could be used effectively as an interlayer between the cathode and the LSGM electrolyte. While the inclusion of a GDC interlayer may complicate cell manufacturing, it may provide an advantage of acting as a buffer layer to thermal expansion mismatch as well as enhancing the electrochemical performance of the cell.[132,133]

SEM micrographs of the cross sections of the $Sr_{3-x}La_xFe_{2-y}Co_yO_{7-\delta}$ cathode, the GDC interlayer, and the LSGM electrolyte are displayed in Figure 8.6 for a few cathode compositions after testing the single cell at 800 ºC. The electrochemical performance of the cathode could be affected by the microstructure as well as the kinetics of oxygen exchange and diffusion. The micrographs show that good adhesion is maintained among the layers. Additionally, the similarity of the microstructures indicates that the variations of the electrochemical performances observed with different cathode compositions are not related to microstructural changes.

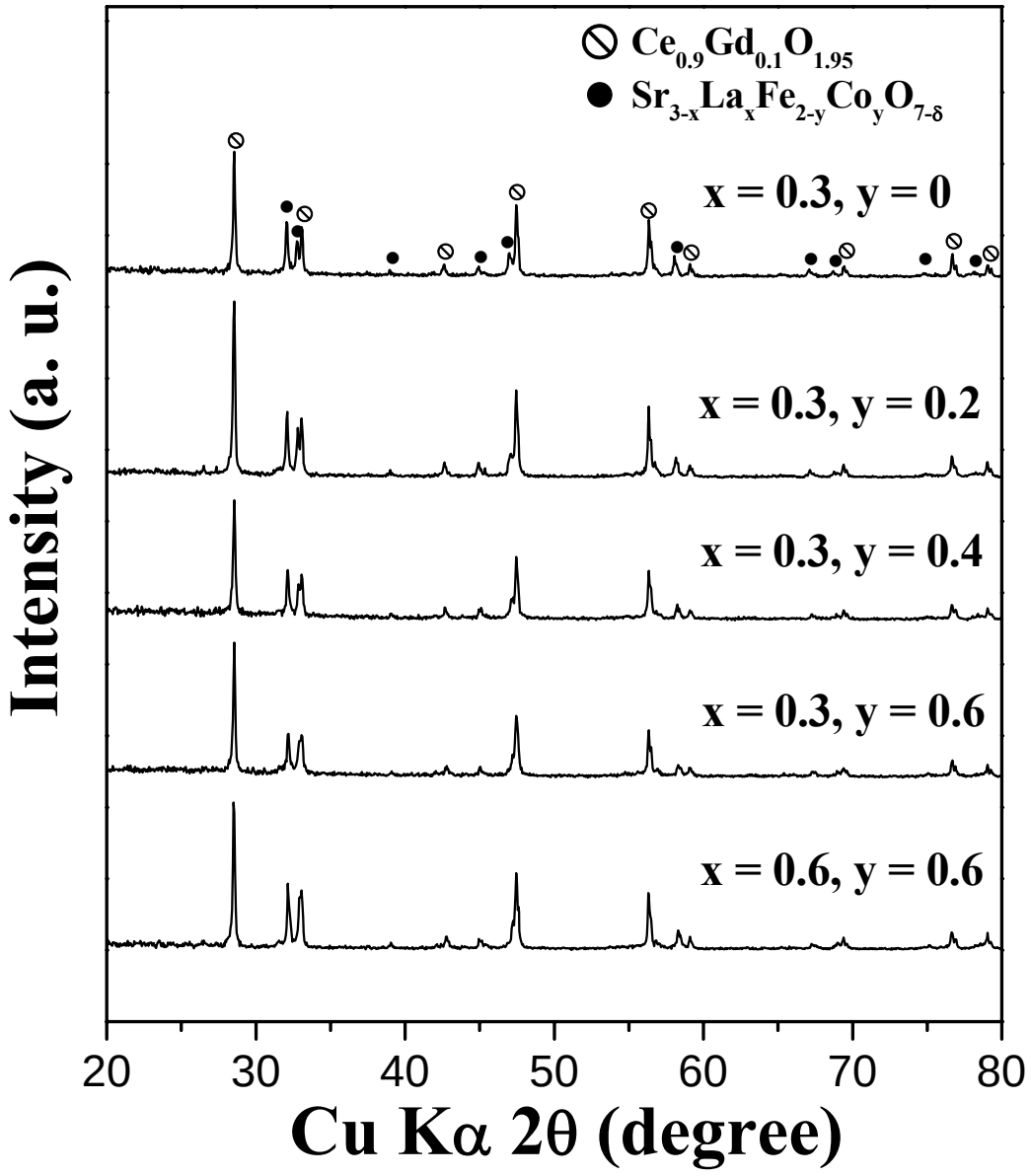

Figure 8.5 X-ray diffraction patterns recorded after heating the $Sr_{3-x}La_xFe_{2-y}Co_yO_{7-\delta}$ cathode and the GDC powders at 1000 ^oC for 3 h.

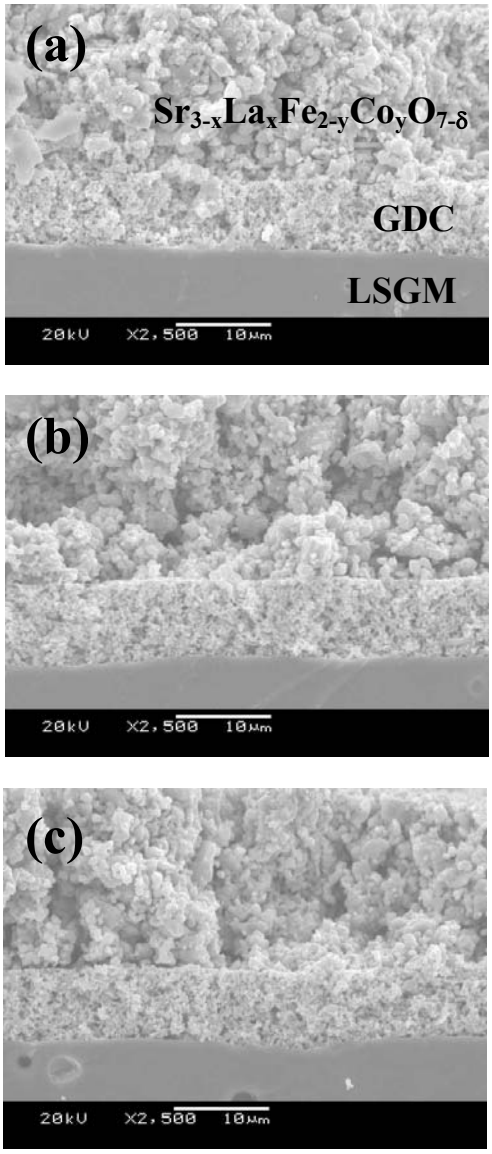

Figure 8.6 SEM micrographs of the $Sr_{3-x}La_xFe_{2-y}Co_yO_{7-\delta}$ cathode with GDC interlayer on the LSGM electrolyte after single cell test at 800 ^oC: (a) x = 0.3, y = 0, (b) x = 0.3, y = 0.6, and (c) x = 0.6, y = 0.6.

8.3.5 Electrochemical Performance

The electrochemical performance tests were carried out with $Sr_{3-x}La_xFe_{2-y}Co_yO_{7-\delta}$/GDC/LSGM/Ni-GDC single cells. The variations of cell voltage, power density, and cathode over-potential for the various $Sr_{3-x}La_xFe_{2-y}Co_yO_{7-\delta}$ cathode compositions are shown in Figure 8.7. The power density and cell voltage increase while the over-potential decreases with increasing Co and La contents. The variations could be understood by considering the following.

Oxygen reduction reaction in a porous cathode is similar to a multiphase catalysis reaction that includes a sequence of steps:[77] (i) diffusion of oxygen from the gas phase ($O_{2,pore}$) to the surface of the porous cathode, (ii) dissociation of adsorbed diatomic oxygen ($O_{2,ad}$) into atomic oxygen (O_{ad}) at the active sites, (iii) surface diffusion of oxygen atoms, (iv) charge transfer, (v) diffusion of oxide ions through the cathode across the cathode/interlayer, (vi) diffusion of oxide ions through the interface layer, and (vii) diffusion of oxide ions through the interlayer/electrolyte interface and into the electrolyte. Furthermore, steps (i)-(iv) can also occur in the porous GDC interlayer. The electrochemical performance of the cell, therefore, relies on oxygen adsorption, dissociation, and diffusion in and across both the cathode and interlayer, and oxide ion diffusion across the electrolyte and the interfaces between the layers. Also, the electrochemical performance relies on charge transfer and electronic conductivity in both the cathode and the interlayer.

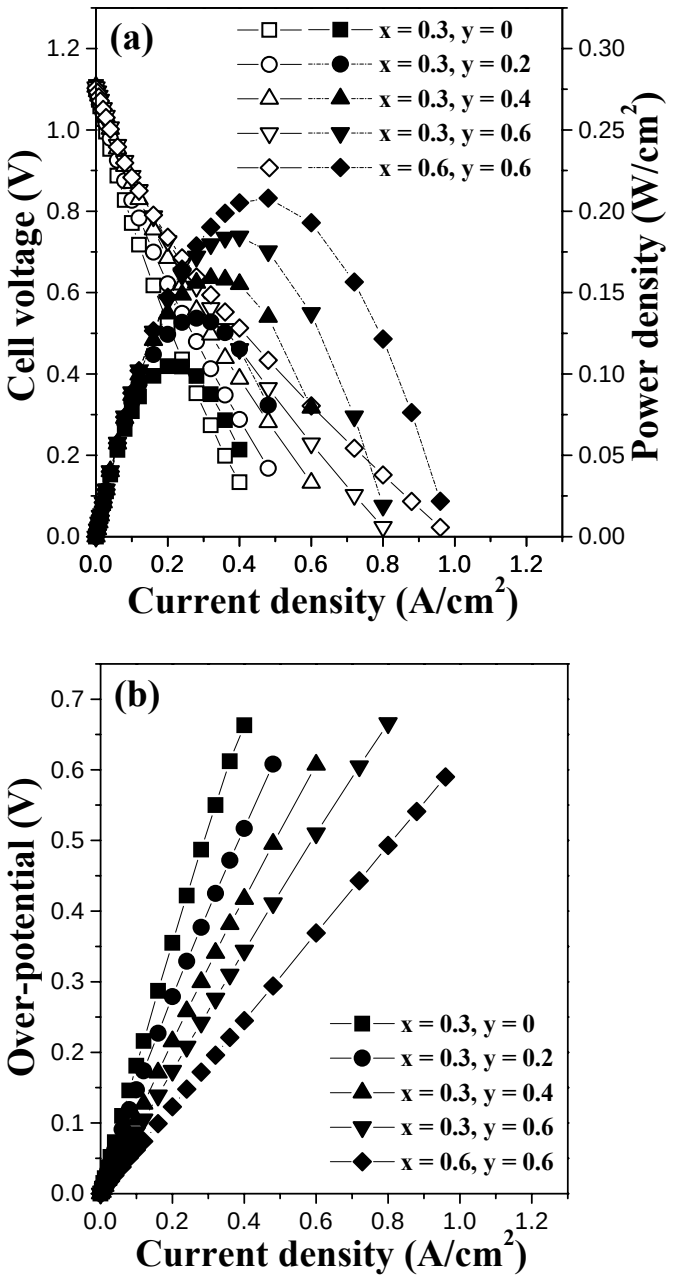

Figure 8.7 Comparison of the electrochemical performances of $Sr_{3-x}La_xFe_{2-y}Co_yO_{7-\delta}$/GDC/LSGM/Ni-GDC single cells at 800 ^oC: variations of (a) the I-V curve (open symbols) and power density (closed symbols) and (b) cathode over-potential.

It has been reported that the rate of oxygen reduction reaction including charge transfer is limited by the availability of free electrons.[144] Therefore, both oxide ion vacancy and electron concentration should be taken into account in understanding the electrochemical performance.

Both the oxide ion vacancy concentration and electrical conductivity increase with Co content as seen in Figures 8.2 and 8.4. Oxide ion vacancies on the surface can enhance oxygen adsorption and dissociation,[77] while the oxide ion vacancies distributed in the bulk of the material can enhance oxide ion diffusion through the cathode. It has been reported before that the oxygen permeation flux in $Sr_{3-x}La_xFe_{2-y}Co_yO_{7-\delta}$ increases with Co content,[122,125] which means an increase in the oxide ion mobility with Co doping. Consequently, the increase in oxygen adsorption, dissociation, and diffusion as well as the improved charge transfer kinetics with Co doping leads to an enhancement in the electrochemical performance.

The substitution of La^{3+} for Sr^{2+}, on the other hand, has a slightly different effect on the electrochemical performance. While conductivity increases with La content, oxide ion vacancy concentration decreases with La content. The decrease in oxide ion vacancy concentration suggests that the oxygen adsorption, dissociation, and diffusion could be debilitated. On the other hand, the increase in electronic conductivity with La content suggests that the charge transfer kinetics could be improved.[144] Considering these two opposing effects and the overall improvement in

the electrochemical performance with La doping, It may be concluded that the rate limiting step for the $Sr_{3-x}La_xFe_{2-y}Co_yO_{7-\delta}$ cathodes is likely the charge transfer step.

However, the overall electrochemical performance of the $Sr_{3-x}La_xFe_{2-y}Co_yO_{7-\delta}$ system is slightly inferior compared to those of the $LaSr_3Fe_{3-y}Co_yO_{10-\delta}$ (n = 3 member) system and the $La_{0.6}Sr_{0.4}CoO_{3-\delta}$ (n = ∞) perovskite system[139] as seen in Figure 8.8. It has been reported that the $Sr_{3-x}La_xFe_{2-y}Co_yO_{7-\delta}$ system exhibits lower oxygen permeation rate and higher activation energy than the $LaSr_3Fe_{3-y}Co_yO_{10-\delta}$ system or the perovskite systems such as $SrCo_{0.8}Fe_{0.2}O_{3-\delta}$.[122,124] This indicates that the oxide ion mobility in the $Sr_{3-x}La_xFe_{2-y}Co_yO_{7-\delta}$ system is slower than that in the $LaSr_3Fe_{3-y}Co_yO_{10-\delta}$ and $La_{0.6}Sr_{0.4}CoO_{3-\delta}$ systems. Thus, the lower electrochemical performance of the $Sr_{3-x}La_xFe_{2-y}Co_yO_{7-\delta}$ system could be due to both a lower electronic conductivity and slower oxide ion mobility. The lower electronic and oxide ion conductivities are in turn related to a lower dimensionality with two perovskite blocks along the *c* axis compared to three and ∞ number of perovskite blocks in the cases of, respectively, $LaSr_3Fe_{3-y}Co_yO_{10-\delta}$ and $La_{0.6}Sr_{0.4}CoO_{3-\delta}$. Nevertheless, the $Sr_{3-x}La_xFe_{2-y}Co_yO_{7-\delta}$ system offers better electrochemical performance at intermediate temperatures compared to the $La_{1-x}Sr_xMnO_{3-\delta}$ cathodes. It also provides an advantage of better structural stability without any phase transitions particularly at lower oxygen partial pressures[122,123,125] compared to the $La_{1-x}Sr_xCoO_{3-\delta}$ perovskite oxide systems.

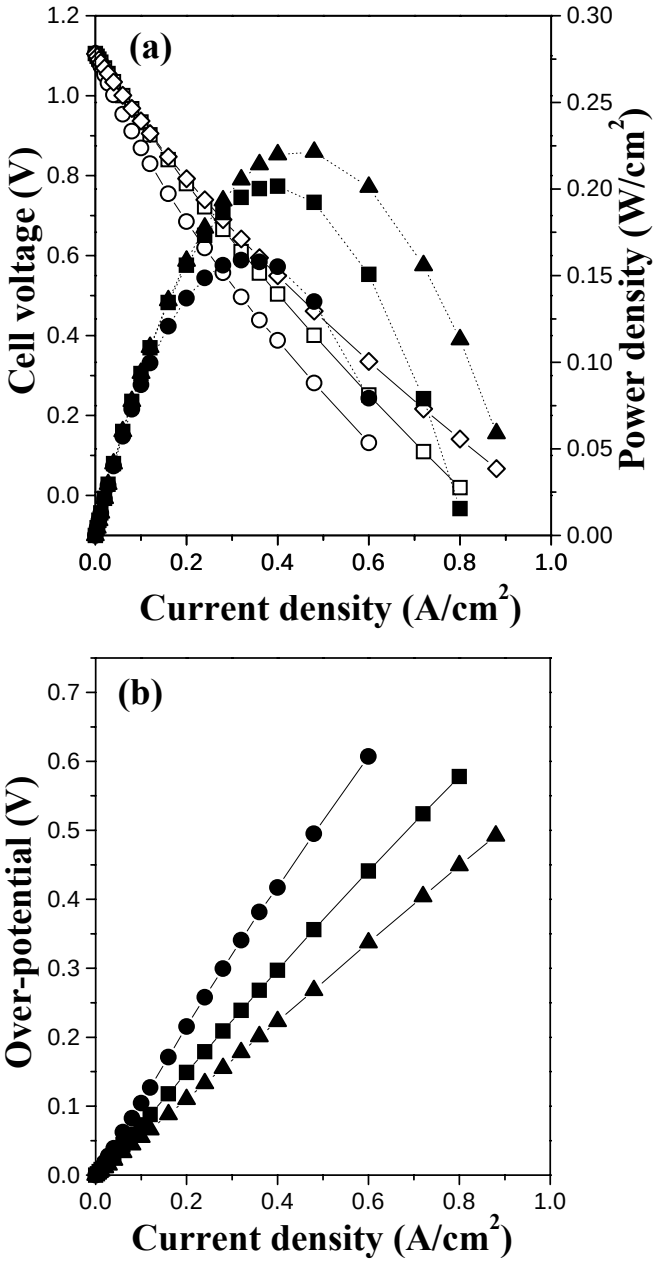

Figure 8.8 Comparison of the electrochemical performances at 800 ^{o}C of the single cells fabricated with the $Sr_{2.7}La_{0.3}Fe_{1.6}Co_{0.4}O_{7-\delta}$ (circles) $LaSr_3Fe_{2.5}Co_{0.5}O_{10-\delta}$ (squares), and $La_{0.6}Sr_{0.4}CoO_{3-\delta}$ (triangles) cathodes: variations of (a) the I-V curve (open symbols) and power density (closed symbols) and (b) cathode over-potential.

8.4 CONCLUSIONS

The perovskite-related $Sr_{3-x}La_xFe_{2-y}Co_yO_{7-\delta}$ ($0.3 \leq x \leq 0.6$ and $0 \leq y \leq 0.6$) intergrowth oxides have been characterized as cathode materials for intermediate temperature SOFC. While the oxygen content decreases with Co content for a given La content due to a lower stability of Co^{4+} compared to Fe^{4+}, it increases with La content for a given Co content due to a replacement of lower valent Sr^{2+} by a higher valent La^{3+}. The TEC increases with Co content for a given La content, but decreases with La content for a given Co content y = 0.6, which could be understood on the basis of oxide ion vacancy concentration, spin state transitions associated with Co^{3+}, and relative strengths of various bonds. With a La content of 0.3, the electrical conductivity increases with Co content due to an increase in the covalent character of the O-(Fe,Co)-O bonds. Single cell tests at 800 ºC indicate that the electrochemical performance increases with increasing Co and La contents, mostly due to an increase in electronic conductivity. However, the electrocatalytic activity of the $Sr_{3-x}La_xFe_{2-y}Co_yO_{7-\delta}$ cathodes is lower than those of the analogous $LaSr_3Fe_{3-y}Co_yO_{10-\delta}$ intergrowth and the $La_{0.6}Sr_{0.4}CoO_{3-\delta}$ perovskite cathodes[139] due to both a lower electronic conductivity and slower oxide ion mobility.

CHAPTER 9

SUMMARY

With an aim to design and develop efficient cathode materials for intermediate temperature SOFC, the $Ln_{1-x}Sr_xCoO_{3-\delta}$ (Ln = La, Pr, Nd, Sm, and Gd) and $Nd_{0.6}Sr_{0.4}Co_{1-y}M_yO_{3-\delta}$ (M = Fe and Mn) perovskite oxide cathodes, incorporation of metallic Ag into porous perovksite oxide cathodes, and new perovskite-related intergrowth oxide cathodes such as $LaSr_3Fe_{3-y}Co_yO_{10-\delta}$ and $Sr_{3-x}La_xFe_{2-y}Co_yO_{7-\delta}$ have been investigated.

A systematic investigation of a correlation of the electrochemical performance to the lanthanide host cations in $Ln_{0.6}Sr_{0.4}CoO_{3-\delta}$ (Ln = La, Pr, Nd, Sm, and Gd) perovskite oxides has been carried out. Both the electrical conductivity and the oxide ion vacancy concentration decrease from Ln = La to Gd, which leads to a decrease in the electrocatalytic activity for the oxygen reduction reaction in SOFC. However, the thermal expansion coefficient (TEC) decreases favorably from Ln = La to Gd due to a decreasing ionicity of the Ln-O bond and a suppression of the tendency to lose oxygen from the lattice with increasing temperature. Therefore, $Ln_{0.6}Sr_{0.4}CoO_{3-\delta}$ cathodes with an intermediate lanthanide ion such as Nd^{3+} offer a tradeoff between electrocatalytic activity and TEC.

With the $Nd_{1-x}Sr_xCoO_{3-\delta}$ system, the Sr content x also affects the crystal chemistry, thermal expansion behavior, electrical conductivity, chemical compatibility, and electrochemical performance. The lattice volume increases with increasing Sr content x. The thermal expansion coefficient decreases with x, reaches a minimum at x = 0.3, and then increases. The electrical conductivity increases with x, and the system exhibits a semiconductor to metal transition at around x = 0.3. The electrocatalytic activity and power density increase with increasing x, reaches a maximum around x = 0.4, and then decreases due to an interfacial reaction of the x = 0.5 sample with the electrolyte.

With an aim to decrease TEC further, the substitution of Fe or Mn for Co in $Nd_{0.6}Sr_{0.4}CoO_{3-\delta}$ has been pursued. The oxygen non-stoichiometry and electrical conductivity decrease with increasing Fe and Mn contents. Both the Fe- and Mn-doped systems exhibit a metal to semiconductor transition at $y \approx 0.2$, but the Mn-doped system exhibits higher activation energy than the Fe-doped system. The TEC decreases with increasing Fe and Mn contents due to a suppression of the low-spin to high-spin transition associated with the Co^{3+} ions and a stronger Fe-O or Mn-O bond compared to the Co-O bond. The electrocatalytic activity decreases with increasing Fe and Mn contents, but the decrease is rapid with the Mn-doped system due to a faster decrease in the oxide ion and electronic conductivities.

Although the $Nd_{0.6}Sr_{0.4}Co_{0.5}Fe_{0.5}O_{3-\delta}$ composition shows favorable TEC, its electrocatalytic activity is lower than that of $La_{0.6}Sr_{0.4}CoO_{3-\delta}$. The incorporation of

metallic Ag into porous $Nd_{0.6}Sr_{0.4}Co_{0.5}Fe_{0.5}O_{3-\delta}$ is found to improve the electrochemical performance. The $Nd_{0.6}Sr_{0.4}Co_{0.5}Fe_{0.5}O_{3-\delta}$-Ag cathodes prepared by ball milling show the maximum performance (power density: 0.15 W/cm^2 at 800 ^{o}C) at 3 wt. % Ag. On the other hand, the $Nd_{0.6}Sr_{0.4}Co_{0.5}Fe_{0.5}O_{3-\delta}$-Ag composite cathodes with 0.1 mg/cm^2 (~ 0.5 wt. %) Ag that were prepared by an impregnation method exhibit much better performance (power density: 0.27 W/cm^2 at 800 ^{o}C) than the composite cathodes prepared by ball milling, despite a much smaller amount of Ag due to a better dispersion and an enhanced adhesion. AC impedance analysis indicates that the Ag catalysts dispersed in the porous $Nd_{0.6}Sr_{0.4}Co_{0.5}Fe_{0.5}O_{3-\delta}$ cathode reduce the ohmic and the polarization resistances due to an increased electronic conductivity and enhanced electrocatalytic activity.

In an effort to develop new cathode materials for intermediate temperature SOFC, the $LaSr_3Fe_{3-y}Co_yO_{10-\delta}$ ($0 \leq y \leq 1.5$) oxides with a perovskite-related intergrowth structure have also been investigated. The electrical conductivity, oxygen vacancy concentration, and TEC increase with increasing Co content y. A porous GDC interlayer successfully prevents the unfavorable reaction between the cathode and electrolyte, and the cathode with GDC interlayer exhibits good electrocatalytic activity. The electrocatalytic activity and power density increase with increasing Co content due to an increase in the electronic and oxide ion conductivities of the cathode. In addition to significantly lower TEC, the $LaSr_3Fe_{3-y}Co_yO_{10-\delta}$ intergrowth

oxide cathodes offer electrochemical performances comparable to that of the well-known $La_{0.6}Sr_{0.4}CoO_{3-\delta}$ perovskite oxide cathode.

The $Sr_{3-x}La_xFe_{2-y}Co_yO_{7-\delta}$ ($0.3 \leq x \leq 0.6$ and $0 \leq y \leq 0.6$) cathodes also show properties similar to that of the $LaSr_3Fe_{3-y}Co_yO_{10-\delta}$ cathodes. With a given La content x, the electrical conductivity, oxide ion vacancy concentration, and TEC increase with increasing Co content y. With a given Co content, while the electrical conductivity increases, the TEC decreases with increasing La content. The electrocatalytic activity and power density increase with increasing Co and La contents due to an increase in electrical conductivity and oxide ion vacancy concentration. However, the $Sr_{3-x}La_xFe_{2-y}Co_yO_{7-\delta}$ cathodes show relatively lower catalytic activity compared to the analogous $LaSr_3Fe_{3-y}Co_yO_{10-\delta}$ and the $La_{0.6}Sr_{0.4}CoO_{3-\delta}$ cathodes due to both a lower electronic conductivity and slower oxide ion mobility.

Overall, this work has provided a better understanding of the structure-property-performance relationships of the cathode materials for intermediate temperature SOFC. The electrochemical performance is strongly related to electrical properties and defect structure, which could be tuned by controlling the chemical composition of the cathode materials. Although the Co containing perovskite oxides show high electronic and oxide ion conductivities leading to better catalytic activity, they exhibit large TEC due to the spin state transition associated with Co^{3+}. Thus, a decrease in the Co content or a suppression of the spin state transition without sacrificing the electrocatalytic activity may be a critical issue in identifying optimum

compositions of the Co containing perovskite cathodes. In this regard, the new class of $LaSr_3Fe_{3-y}Co_yO_{10-\delta}$ intergrowth oxides could be a promising cathode material for intermediate temperature SOFC, considering the good catalytic activity and significantly lower TEC compared to those of the Co containing perovskite oxides. Therefore, future work could focus on enhancing the electrochemical performance and decreasing the TEC of $LaSr_3Fe_{3-y}Co_yO_{10-\delta}$ through a further tuning of the chemical compositions by doping with Ni and Cu or replacing Sr with Ca. Additionally, since the electrochemical performance of the cathodes could be affected by the microstructure as well as the kinetics of oxygen exchange and diffusion, solution-based synthesis procedures such as coprecipitation or citrate-based synthesis could be pursued to optimize the microstructure and porosity.

LIST OF PUBLICATIONS RELATED TO THIS WORK

1. K. T. Lee and A. Manthiram, "Characterization of Sr-doped neodymium cobalt oxide cathode materials for intermediate temperature solid oxide fuel cells," *Ceramic Transactions: Development in Solid Oxide Fuel Cells and Lithium Ion Batteries*, A. Manthiram, P. N. Kumta, S. K. Sundaram, and S. Chan, Editors, Vol. 161, p. 3, American Ceramic Society, Westerville, OH (2004).

2. K. T. Lee and A. Manthiram, "Characterization of $Nd_{1-x}Sr_xCoO_{3-\delta}$ ($0 \le x \le 0.5$) cathode materials for intermediate temperature solid oxide fuel cells," *J. Electrochem.Soc.*, **152**, A197 (2005).

3. K. T. Lee and A. Manthiram, "Characterization of $Nd_{0.6}Sr_{0.4}Co_{1-y}Fe_yO_{3-\delta}$ ($0 \le y \le 0.5$) cathode materials for intermediate temperature solid oxide fuel cells," *Solid State Ionics*, **176**, 1521 (2005).

4. K. T. Lee and A. Manthiram, "Comparison of $Ln_{0.6}Sr_{0.4}CoO_{3-\delta}$ (Ln = La, Pr, Nd, Sm, and Gd) cathode materials for intermediate temperature solid oxide fuel cells," *J. Electrochem. Soc.*, **154**, A794 (2006).

5. K. T. Lee and A. Manthiram, "$LaSr_3Fe_{3-y}Co_yO_{10-\delta}$ ($0 \le y \le 1.5$) intergrowth oxide cathodes for intermediate temperature solid oxide fuel cells," *Chem. Mater.*, **18**, 1621 (2006).

6. K. T. Lee and A. Manthiram, "Investigation of $Nd_{0.6}Sr_{0.4}Co_{1-y}M_yO_{3-\delta}$ (M = Fe and Mn) as cathode materials for intermediate temperature solid oxide fuel cells," *Advances in Electronic and Electrochemical Ceramics* F. Dogan and P. N. Kumta, Editors, Vol. 179, American Ceramic Society, Westerville, OH, (in press).

7. K. T. Lee and A. Manthiram, "Synthesis and characterization of $Nd_{0.6}Sr_{0.4}Co_{1-y}Mn_yO_{3-\delta}$ ($0 \le y \le 1.0$) cathode materials for intermediate temperature solid oxide fuel cells," *J. Power Sources*, (in press).

8. K. T. Lee and A. Manthiram, "Electrochemical performance of $Nd_{0.6}Sr_{0.4}Co_{0.5}Fe_{0.5}O_{3-\delta}$-Ag composite cathodes for intermediate temperature solid oxide fuel cells," *J. Power Sources*, (in press).

9. K. T. Lee, D.M. Bierschenk, and A. Manthiram, "$Sr_{3-x}La_xFe_{2-y}Co_yO_{7-\delta}$ ($0.3 \le x \le 0.6$ and $0 \le y \le 0.6$) intergrowth oxide cathodes for intermediate temperature solid oxide fuel cells," *J. Electrochem. Soc.*, (in press).

REFERENCES

1. O. Yamamoto, *Electrochim. Acta*, **45**, 2423 (2000).
2. G. J. K. Acres, *J. Power Sources*, **100**, 60 (2001).
3. A. B. Stambouli and E. Traversa, *Renewable & Sustainable Energy Reviews*, **6**, 297 (2002).
4. F. Alcaide, P. -L. Cabot, and E. Brillas, *J. Power Sources*, **153**, 47 (2006).
5. K. Koon, *J. Power Sources*, **71**, 12 (1998).
6. S. C. Singhal, *Solid State Ionics*, **135**, 305 (2000).
7. M. Dokiya, *Solid State Ionics*, **152-153**, 386 (2002).
8. K. Kordesch and G. Simader, *Fuel Cells and Their Applications*, p. 25, VCH, New York, USA (1996).
9. C. M. A. Brett and A. M. O. Brett, *Electrochemistry, Principles, Methods, and Applications*, p. 14, Oxford University Press Inc., New York, USA (1993).
10. J. Larminie and A. Dicks, *Fuel Cell Systems Explained*, p. 37, John Wiley & Sons, New York, USA (2000).
11. K. B. Oldham and J. C. Myland, *Fundamentals of Electrochemical Science*, p. 187, Academic Press Inc., San Diego, USA (1994).
12. N. Q. Minh and T. Takahshi, *Science and Technology of Ceramic Fuel Cells*, p. 21, Elsevier Science B. V., Amsterdam, The Netherlands (1995).

13. M. C. Williams, *Fuel Cell Handbook,* 5th Edition, Report prepared by EG&G Services, Parsons, Inc. and Science Applications International Corporation under contract no. DE-AM26-99FT40575 for the U.S. Department of Energy, National Energy Technology Laboratory (2000).
14. N. Q. Minh, *J. Am. Ceram. Soc.*, **76**, 563 (1993).
15. G. Adachi, N. Imanaka, and S. Tamura, *Chem. Rev.*, **102**, 2405 (2002).
16. E. C. Subbarao and H. S. Maiti, *Solid State Ionics*, **11**, 317 (1984).
17. F. A. Kröger and H. J. Vink, *Solid State Phys.*, **3**, 307 (1956).
18. T. Takahashi, T. Esaka, and H. Iwahara, *J. Appl. Electrochem.*, **7**, 303 (1977).
19. H. L. Tuller and A. S. Nowick, *J. Electrochem. Soc.*, **122**, 255 (1975).
20. T. Kudo and Y. Obayashi, *J. Electrochem. Soc.*, **123**, 415 (1976).
21. H. Yahiro, Y. Baba, K. Eguchi, and H. Arai, *J. Electrochem. Soc.*, **135**, 2077 (1988).
22. D. L. Maricle, T. E. Swarr, and S. Karavolis, *Solid State Ionics*, **52**, 173 (1992).
23. K. Eguchi, T. Setoguchi, T. Inoue, and H. Arai, *Solid State Ionics*, **52**, 165 (1992).
24. A. V. Virkar, *J. Electrochem. Soc.*, **138**, 1481 (1991).
25. J. B. Goodenough, A. Manthiram, P. Paramthaman, and Y. S. Zhen, *Solid State Ionics*, **52**, 105 (1992).
26. M. Feng and J. B. Goodenough, *Eur. J. Solid State Inorg. Chem.*, **31**, 663 (1994).
27. T. Ishihara, H. Matsuda, and Y. Takita, *J. Am. Chem. Soc.*, **116**, 3801 (1994).
28. W. Z. Zhu and S. C. Deevi, *Mat. Sci. Eng.*, **A362**, 228 (2003).

29. M. Godickemeier, K. Sasaki, and L. J. Gauckler, in *Proceedings of the Fourth International Symposium on Solid Oxide Fuel Cells*, O. Yamamoto, H. Tagawa, and S. C. Singhal, Editors, The Electrochemical Society Proceedings Series, p. 1072, The Electrochemical Society Inc., Pennington, NJ, USA (1995).
30. R. M. Ormerod, *Stud. Surf. Sci. Catal.* **122**, 35 (1999).
31. M. Joerger and L. J. Gauckler, in *Proceedings of the Seventh International Symposium on Solid Oxide Fuel Cells*, K. Yokokawa and S. C. Singhal, Editors, The Electrochemical Society Proceedings Series, p. 662, The Electrochemical Society Inc., Pennington, NJ, USA (2001).
32. S. Park, H. Kim, S. Mcintosh, W. Worrell, R. J. Gorte, and J. M. Vohs, in *Proceedings of the Seventh International Symposium on Solid Oxide Fuel Cells*, K. Yokokawa and S. C. Singhal, Editors, The Electrochemical Society Proceedings Series, p. 712, The Electrochemical Society Inc., Pennington, NJ, USA (2001).
33. P. Vernoux, M. Guillodo, J. Fouletier, and A. Hammon, *Solid State Ionics*, **135**, 425 (2000).
34. S. P. Jiang, J. P. Zhang, Y. Ramprakash, D. Millosevic, and K. Wilshier, *J. Mater. Sci.*, **35**, 2735 (2000).
35. H. Yokokawa, N. Sakai, T. Kawada, and M. Dokiya, *J. Electrochem. Soc.*, **138**, 2719 (1991).
36. K. Wiik, C. R. Schmidt, S. Faaland, S. Shamsili, M. A. Einarsrud, and T. Grande, *J. Am. Chem. Soc.*, **82**, 721 (1999).

37. S. Srilomsak, D. P. Schilling, and H. U. Anderson, in *Proceedings of the First International Symposium on Solid Oxide Fuel Cells*, S. C. Singhal, Editor, The Electrochemical Society Proceedings Series, p. 129, The Electrochemical Society Inc., Pennington, NJ, USA (1989).
38. H. U. Anderson, *Solid State Ionics*, **52**, 33 (1992).
39. S. Carter, A. Selcuk, R. J. Chater, J. Kajda, J. A. Kilner, and B. C. H. Steele, *Solid State Ionics*, **53-56**, 597 (1992).
40. R. A. De Souza and J. A. Kilner, *Solid State Ionics*, **106**, 175 (1998).
41. J. Mizusaki, J. Tabuch, T. Matsuura, S. Yamauchi, and K. Fueki, *J. Electrochem. Soc.*, **136**, 2082 (1989).
42. A. Petric, P. Huang, and F. Tietz, *Solid State Ionics*, **135**, 719 (2000).
43. M. A. Señaris-Rodriguez and J. B. Goodenough, *J. Solid State Chem.*, **116**, 224 (1995).
44. Y. Ohno, S. Nagata, and H. Sato, *Solid State Ionics*, **9-10**, 1001 (1983).
45. T. Kawada, J. Suzuki, M. Sase, A. Kaimai, K. Yashiro, Y. Nigara, J. Mizusaki, K. Kawamura, and H. Yugami, *J. Electrochem. Soc.*, **149**, E252 (2002).
46. W. Zipprich, S. Waschilewski, F. Rocholl, and H. D. Wiemhofer, *Solid State Ionics*, **101-103**, 1015 (1997).
47. W. Zipprich and H. D. Wiemhofer, *Solid State Ionics*, **135**, 699 (2000).
48. O. Yamamoto, Y. Takeda, R. Kanno, and M. Noda, *Solid State Ionics*, **22**, 241 (1987).

49. J. W. Adams, H. H. Nakamura, R. P. Ingel, and R. W. Rice, *J. Am. Ceram. Soc.*, **68**, C-228 (1985).

50. L. A. Chick, L. R. Pederson, G. D. Maupin, J. L. Bates, L. E. Thomas, and G. J. Exarhos, *Mater. Lett.*, **10**, 6 (1990).

51. R. A. Young, A. Shakthivel, T. S. Moss, and C. O. P. Santos, *J. Appl. Crystallogr.*, **28**, 366 (1995).

52. L. V. Azaroff, *Elements of X-ray Crystallography*, p. 552, McGraw-Hill, New York, USA (1968).

53. A. Manthiram, J. S. Swinnea, Z. T. Sui, H. Steinfink, and J. B. Goodenough, *J. Am. Chem. Soc.*, **109**, 6667 (1987).

54. L. J. Van der Pauw, *Philips Research Reports*, **13**, 1 (1958).

55. I. Reiss, *J. Appl. Phy.*, **71**, 4079 (1992).

56. M. T. Colomer, B. C. H. Steele, and J. A. Kilner, *Solid State Ionics*, **147**, 41 (2002).

57. A. N. Petrov, O. F. Kononchuk, A. V. Andreev, V. A. Cherepanov, and P. Kofstad, *Solid State Ionics*, **80**, 189 (1995).

58. L. W. Tai, M. M. Nasrallah, H. U. Anderson, D. M. Sparlin, and S. R. Sehlin, *Solid State Ionics*, **76**, 259 (1995).

59. G. Ch. Kostogloudis, N. Vasilakos, and Ch. Ftikos, *Solid State Ionics*, **106**, 207 (1998).

60. K. T. Lee and A. Manthiram, *J. Electrochem. Soc.*, **152**, A197 (2005).

61. C. Xia, W. Rauch, F. Chen, and M. Liu, *Solid State Ionics*, **149**, 11 (2002).

62. Y. Takeda, H. Ueno, N. Imanishi, O. Yamamoto, N. Sammes, and M. B. Phillipps, *Solid State Ionics*, **86-88**, 1187 (1996).

63. H. Y. Tu, Y. Takeda, N. Imanishi, and O. Yamamoto, *Solid State Ionics*, **100**, 283 (1997).

64. H. Ohbayashi, T. Kudo, and T. Gejo, *Jpn. J. Appl. Phys.*, **13**, 1 (1974).

65. L. Brewer, in *Systematics and the Properties of the Lanthanides*, S. P. Sinha, Editor, p. 36, NATO ASI series, Series C, Mathematical and Physical Science, No. 109, D. Reidel Publishing Co., Dordrecht, Holland (1982).

66. H. Takahashi, F. Munakata, and M. Yamanaka, *Phys. Rev. B*, **57**, 15211 (1998).

67. Y. Sakaki, Y. Takeda, A. Kato, N. Imanish, O. Yamamoto, M. Hattori, M. Iio, and Y. Esaki, *Solid State Ionics*, **118**, 187 (1999).

68. F. Riza, Ch. Ftikos, F. Tietz, and W. Fischer, *J. Eur. Ceram. Soc.*, **21**, 1769 (2001).

69. M. Mori, Y. Hiei, N. M. Sammes, and G. A. Tompsett, *J. Electrochem. Soc.*, **147**, 1295 (2000).

70. W. D. Callister, Jr., *Materials Science and Engineering an Introduction*, 5th Edition, p. 23, John Wiley & Sons Inc., NY, USA (2000).

71. M. Barsoum, *Fundamentals of Ceramics*, p. 26, McGraw-Hill Companies Inc., NY, USA (1997).

72. M. Mori and N. M. Sammes, *Solid State Ionics*, **146**, 301 (2002).

73. A. R. Ruffa, *J. Mater. Sci.*, **15**, 2258 (1980).

74. H. Hayashi, M. Kanoh, C. J. Quan, H. Inaba, S. Wang, M. Dokiya, and H. Tagawa, *Solid State Ionics*, **132**, 227 (2000).

75. K. Huang, H. Y. Lee, and J. B. Goodenough, *J. Electrochem. Soc.*, **145**, 3220 (1998).

76. V. V. Kharton, E. N. Naumovich, A. A. Vecher, and A. V. Nikolaev, *J. Solid State Chem.*, **120**, 128 (1995).

77. J. Gao, X. Liu, D. Peng, and G. Meng, *Catal. Today*, **82**, 207 (2003).

78. L. Cong, T. He, Y. Ji, P. Guan, Y. Huang, and W. Su, *J. Alloys Comp.*, **348**, 225 (2003).

79. L. Qiu, T. Ichikawa, A. Hirano, N. Imanish, and Y. Takeda, *Solid State Ionics*, **158**, 55 (2003).

80. T. Wen, H. Tu, Z. Xu, and O. Yamamoto, *Solid State Ionics*, **121**, 25 (1999).

81. T. Horita, K. Yamaji, M. Ishikawa, N. Sakai, H. Yokokawa, T. Kawada, and T. Kato, *J. Electrochem. Soc.*, **145**, 3196 (1998).

82. F. Zheng and L. R. Pederson, *J. Electrochem. Soc.*, **146**, 2810 (1999).

83. S. B. Adler, *Solid State Ionics*, **111**, 125 (1998).

84. M. Koyama, C. Wen, T. Masuyama, J. Otomo, H. Fukunaga, K. Yamade, K. Eguchi, and H. Takahashi, *J. Electrochem. Soc.*, **148**, A795 (2001).

85. P. Shuk, V. Charton, and V. Samochval, *Materials Science Forum*, **76**, 161 (1991).

86. C. H. Yo, K. S. Roh, S. J. Lee, K. H. Kim, and E. J. Oh, *J. Korean Chem. Soc.*, **35**, 211 (1991).

87. J. P. Tang, R. I. Dass, and A. Manthiram, *Mater. Res. Bull.*, **35**, 411 (2000).

88. R. D. Shannon, *Acta Crystallogr.*, **A32**, 751 (1976).

89. S. V. Chavan, S. J. Patwe, and A. K. Tyagi, *J. Alloy. Compd.*, **360**, 189 (2003).

90. J. N. Eastabrook, *Philos. Mag.*, **2**, 1421 (1957).

91. P. M. Raccah and J. B. Goodenough, *Phys. Rev.*, **155**, 932 (1967).

92. D. S. Rajoria, V. G. Bhide, G. Rama Rao, and C. N. R. Rao, *J. Chem. Soc. Faraday II*, **70**, 512 (1974).

93. M. A. Señaris-Rodriguez and J. B. Goodenough, *J. Solid State Chem.*, **118**, 323 (1995).

94. H. Hayashi, M. Suzuki, and H. Inaba, *Solid State Ionics*, **128**, 131 (2000).

95. H. Ullmann, N. Trofimenko, F. Tietz, D. Stöver, and A. Ahmad-Khanlou, *Solid State Ionics*, **138**, 79 (2000).

96. I. G. Austin and N. F. Mott, *Adv. Phys.*, **18**, 41 (1969).

97. G. A. Sawatzky, W. Geertsma, and C. Haas, *J. Magn. Magn. Mater.,* **3**, 37 (1976).

98. J. K. Burdett, *Chemical Bonding in Solids*, p. 167, Oxford University Press, New York, USA (1995).

99. J. B. Torrance, P. Lacorre, A. I. Nazzal, E. J. Ansaldo, and Ch. Niedermayer, *Phys. Rev. B,* **45**, 8209 (1992).

100. K. Huang, M. Feng, and J. B. Goodenough, *J. Electrochem. Soc.*, **143**, 3630 (1996).

101. V. L. Kozhevnikov, I. A. Leonidov, E. B. Mitberg, M. V. Patrakeev, A. N. Petrov, and K. R. Poeppelmeier, *J. Solid State Chem.*, **172**, 296 (2003).

102. B. C. H. Steele, *Mater. Sci. Eng. B*, **13**, 79 (1992).

103. J. Mizusaki, Y. Mima, S. Yamauchi, K. Fueki, and H. Tagawa, *J. Solid State Chem.*, **80**, 102 (1989).

104. J. Mizusaki, H. Tagawa, K. Naraya, and T. Sasamoto, *Solid State Ionics*, **49**, 111 (1991).

105. M. H. R. Lankhorst and J. E. ten Elshof, *J. Solid State Chem.*, **130**, 302 (1997).

106. G. Ch. Kostogloudis, P. Fertis, and Ch. Ftikos, *Solid State Ionics*, **118**, 241 (1999)

107. J. W. Stevenson, T. R. Armstrong, R. D. Carneim, L. R. Pederson, and W. J. Weber, *J. Electrochem. Soc.*, **143**, 2722 (1996).

108. K. T. Lee and A. Manthiram, *Solid State Ionics*, **176**, 1521 (2005).

109. K. T. Lee and A. Manthiram, *J. Electrochem. Soc.*, **154**, A794 (2006).

110. H. Uchida, S. Arisaka, and M. Watanabe, *Solid State Ionics*, **135**, 347 (2000).

111. K. Sasaki, J. Tamura, and M. Dokiya, *Solid State Ionics*, **144**, 223 (2001).

112. K. Sasaki, J. Tamura, H. Hosada, T. N. Lan, K. Yasumoto, and M. Dokiya, *Solid State Ionics*, **148**, 551 (2002).

113. H. Uchida, S. Arisaka, and M. Watanabe, *J. Electrochem. Soc.*, **149**, A13 (2002).

114. R. Baker, J. Guindet, and M. Kleitz, *J. Electrochem. Soc.*, **144**, 2427 (1997).

115. J. Zhang, Y. Ji, H. Gao, T. He, and J. Liu, *J. Alloys Comp.*, **395**, 322 (2005).

116. C. Xia, Y. Zhang, and M. Liu, *Appl. Phy. Lett.*, **82**, 901 (2003).

117. S. Uhlenbruck, F. Tietz, V. Haanappel, D. Sebold, H. P. Buchkremer, and D. Stöver, *J. Solid State Electrochem.*, **8**, 923 (2004).

118. S. Wang, T. Kato, S. Nagata, T. Honda, T. Kaneko, N. Iwashita, and M. Dokiya, *Solid State Ionics*, **146**, 203 (2002).

119. R. Craciun, S. Park, R. J. Gorte, J. M. Vohs, C. Wang, and W. L. Worrell, *J. Electrochem. Soc.*, **146**, 4019 (1999).

120. S. J. Skinner and J. A. Kilner, *Solid State Ionics*, **135**, 709 (2000).

121. J. A. Kilner and C. K. M. Shaw, *Solid State Ionics*, **154**, 523 (2002).

122. F. Prado, T. Armstrong, A. Caneiro, and A. Manthiram, *J. Electrochem. Soc.*, **148**, J7 (2001).

123. F. Prado and A. Manthiram, *J. Solid State Chem.*, **158**, 307 (2001).

124. T. Armstrong, F. Prado, and A. Manthiram, *Solid State Ionics*, **140**, 89 (2001).

125. A. Manthiram, F. Prado, and T. Armstrong, *Solid State Ionics*, **152-153**, 647 (2002).

126. S. N. Ruddlesden and P. Popper, *Acta Crystallogr.*, **11**, 54 (1958).

127. Y. Matsumoto, S. Yamamoto, T. Nishida, and E. Sato, *J. Electrochem. Soc.*, **27**, 2360 (1980).

128. N. Dasgupta, R. Krishnamoorthy, and K. T. Jacob, *Mater. Sci. Eng.*, **B90**, 278 (2002).

129. V. G. Bhide, D. S. Rajoria, Y. S. Reddy, G. Rama Rao, G. V. Subba Rao, and C. N. R. Rao, *Phys. Rev. Letters*, **28**, 1133 (1972).

130. M. W. Chase, Jr., C. A. Davies, J. R. Downey, Jr., D. J. Frurip, R. A. McDonald, and A. N. Syverud, *J. Phys. Chem. Ref. Data*, **118**, Suppl. 1, 926 (1985).

131. H. Uchida, S. Arisaka, and M. Watanabe, *Electrochem. Solid-State Lett.*, **2**, 428 (1999).

132. S. P. Simner, J. F. Bonnett, N. L. Canfield, K. D. Meinhard, J. P. Shelton, V. L. Sprenkle, and J. W. Stevenson, *J. Power Sources*, **113**, 1 (2003).

133. T. L. Nguyen, K. Kobayashi, T. Honda, Y. Iimura, K. Kato, A. Neghisi, K. Nozaki, F. Tappero, K. Sasaki, H. Shirahama, K. Ota, M. Dokiya, and T. Kato, *Solid State Ionics*, **174**, 163 (2004).

134. A. Mai, V. A. C. Haanappel, S. Uhlenbruck, R. Tietz, and D. Stöver, *Solid State Ionics*, **176**, 1341 (2005).

135. M. Shiono, K. Kobayashi, T. L. Nguyen, K. Hosoda, T. Kato, K. Ota, and M. Dokiya, *Solid State Ionics*, **170**, 1 (2004).

136. H. J. M. Bouwmeester, M. W. Den Otter, and B. A. Boukamp, *J. Solid State Electrochem.*, **8**, 599 (2004).

137. J. A. Kerr, in *CRC Handbook of Chemistry and Physics*, 81st Edition, D. R. Lide, Editor, p. 9-54, CRC Press, Boca Raton, Florida, USA, (2000).

138. W. Kuncewicz-Kupczyk, D. Kobertz, M. Miller, L. Singheiser, and K. Hilpert, *J. Electrochem. Soc.*, **148**, E276 (2001).

139. K. T. Lee and A. Manthiram, *Chem. Mater.*, **18**, 1621 (2006).

140. F. Prado and A. Manthiram, in *Recent Research Developments in Materials Science and Engineering*, S. G. Pandalai, Editor, Vol. 1, Part I, p. 329, Transworld Research Network, Trivandrum, India, (2002).

141. J. B. Torrance, P. Lacorre, C. Asavaroengchai, and R. M. Metzger, *Physica C*, **182**, 351 (1991).

142. J. B. Torrance, P. Lacorre, C. Asavaroengchai, and R. M. Metzger, *J. Solid State Chem.*, **90**, 168 (1991).

143. N. F. Mott and E. A. Davis, *Electronic Processes in Noncrystalline Materials*, 2nd Edition, Oxford University Press, (1979).

144. Y. Ji, J. A. Kilner, and M. F. Carolan, *Solid State Ionics*, **176**, 937 (2005).

VITA

Ki-Tae Lee was born as the eldest son of Young-Seok Lee and Dong-Bun Kim, on November 16, 1971, in Seoul, Republic of Korea. He earned his B.S. and M.S. degrees in Ceramic Engineering from Yonsei University in Seoul, Republic of Korea in February, 1998 and February, 2000 respectively. He worked at the Korea Institute of Science and Technology as a research scientist from March, 2000 to September, 2001. He entered The University of Texas at Austin in August, 2002.

List of Publications:

1. S. M. Choi, K. T. Lee, S. Kim, M. C. Chun, and H. L. Lee, "Oxygen ion conductivity and cell performance of $La_{0.9}Ba_{0.1}Ga_{1-x}Mg_xO_{3-\delta}$ electrolyte," *Solid State Ionics*, **131**, 221 (2000).
2. J. D. Kim, G. D. Kim, J. W. Moon, H. W. Lee, K. T. Lee, and C. E. Kim, "The effect of percolation on electrochemical performance," *Solid State Ionics*, **133**, 67 (2000).
3. S. Kim, M. C. Chun, K. T. Lee, and H. L. Lee, "Oxygen-ion conductivity of BaO- and MgO-doped $LaGaO_3$ electrolytes," *J. Power Sources*, **93**, 279 (2001).
4. K. T. Lee, S. Kim, G. D. Kim, and H. L. Lee, "Electrical conduction behavior of Ba^{2+} and Mg^{2+} doped $LaGaO_3$ perovskite oxide," *J. Applied Electrochem.*, **31**, 1243 (2001).
5. S. Kim, K. T. Lee, and H. L. Lee, "Phase relationship of barium and magnesium doped $LaGaO_3$ oxides," *Materials Letters*, **52**, 342 (2002).
6. K. T. Lee and A. Manthiram, "Characterization of Sr-doped neodymium cobalt oxide cathode materials for intermediate temperature solid oxide fuel cells," *Ceramic Transactions: Development in Solid Oxide Fuel Cells and Lithium Ion Batteries*, A. Manthiram, P. N. Kumta, S. K. Sundaram, and S. Chan, Editors, Vol. 161, p. 3, American Ceramic Society, Westerville, OH (2004).

7. K. T. Lee and A. Manthiram, "Characterization of $Nd_{1-x}Sr_xCoO_{3-\delta}$ ($0 \le x \le 0.5$) cathode materials for intermediate temperature solid oxide fuel cells," *J. Electrochem.Soc.*, **152**, A197 (2005).
8. K. T. Lee and A. Manthiram, "Characterization of $Nd_{0.6}Sr_{0.4}Co_{1-y}Fe_yO_{3-\delta}$ ($0 \le y \le 0.5$) cathode materials for intermediate temperature solid oxide fuel cells," *Solid State Ionics*, **176**, 1521 (2005).
9. K. T. Lee and A. Manthiram, "Comparison of $Ln_{0.6}Sr_{0.4}CoO_{3-\delta}$ (Ln = La, Pr, Nd, Sm, and Gd) cathode materials for intermediate temperature solid oxide fuel cells," *J. Electrochem. Soc.*, **154**, A794 (2006).
10. K. T. Lee and A. Manthiram, "$LaSr_3Fe_{3-y}Co_yO_{10-\delta}$ ($0 \le y \le 1.5$) intergrowth oxide cathodes for intermediate temperature solid oxide fuel cells," *Chem. Mater.*, **18**, 1621 (2006).
11. K. T. Lee and A. Manthiram, "Investigation of $Nd_{0.6}Sr_{0.4}Co_{1-y}M_yO_{3-\delta}$ (M = Fe and Mn) as cathode materials for intermediate temperature solid oxide fuel cells," *Advances in Electronic and Electrochemical Ceramics* F. Dogan and P. N. Kumta, Editors, Vol. 179, American Ceramic Society, Westerville, OH, (in press).
12. K. T. Lee and A. Manthiram, "Synthesis and characterization of $Nd_{0.6}Sr_{0.4}Co_{1-y}Mn_yO_{3-\delta}$ ($0 \le y \le 1.0$) cathode materials for intermediate temperature solid oxide fuel cells," *J. Power Sources*, (in press).
13. K. T. Lee and A. Manthiram, "Electrochemical performance of $Nd_{0.6}Sr_{0.4}Co_{0.5}Fe_{0.5}O_{3-\delta}$-Ag composite cathodes for intermediate temperature solid oxide fuel cells," *J. Power Sources*, (in press).
14. K. T. Lee, D.M. Bierschenk, and A. Manthiram, "$Sr_{3-x}La_xFe_{2-y}Co_yO_{7-\delta}$ ($0.3 \le x \le 0.6$ and $0 \le y \le 0.6$) intergrowth oxide cathodes for intermediate temperature solid oxide fuel cells," *J. Electrochem. Soc.*, (in press).

Permanent address: 82-30 Seongnae 2 Dong, Gangdong-Gu,

Seoul, Republic of Korea 134-032

This dissertation was typed by the author.